University of New Mexico
UNM Digital Repository

Summer 7-15-2018

Dense-array teleseismic imaging of the southern Albuquerque basin

Tori S. Finlay
University of New Mexico

Follow this and additional works at: https://digitalrepository.unm.edu/eps_etds

 Part of the Geology Commons, and the Geophysics and Seismology Commons

Recommended Citation

Tori Finlay_____

Candidate

Earth and Planetary Sciences_____

Department

This thesis is approved, and it is acceptable in quality and form for publication:

Approved by the Thesis Committee:

   Dr. Lindsay Lowe Worthington, Chairperson_____

_____

   Dr. Brandon Schmandt_____

_____

   Dr. Mousumi Roy_____

_____

DENSE-ARRAY TELESEISMIC IMAGING OF THE SOUTHERN ALBUQUERQUE BASIN

by

TORI S. FINLAY

BS GEOLOGY, KUTZTOWN UNIVERSITY, 2016

THESIS

Submitted in Partial Fulfillment of the
Requirements for the Degree of

**Master of Science
Earth and Planetary Sciences**

The University of New Mexico
Albuquerque, New Mexico

July 2018

Dense-Array Teleseismic Imaging of the Southern Albuquerque Basin

by

Tori Finlay

BS Geology, Kutztown University, 2016

MS Earth and Planetary Sciences, University of New Mexico, 2018

Abstract

The southern Albuquerque basin is a complex area of high extension, multiple orogenies, and ongoing uplift from a midcrustal magma body in which geophysical coverage is sparse. In this thesis, I capitalize on recent innovations in dense-array processing techniques to create virtual source reflection profiles from five teleseismic events during the deployment of the Sevilleta array. The Sevilleta array consisted of ~800 vertical component nodes with ~300 m spacing deployed for 10 days in February of 2015. Virtual source reflection profiles are created by using the free surface of the earth as a virtual seismic source, yielding profiles that mimic active source seismic surveys. From the seventeen virtual source reflection profiles created, I am able to resolve mapped and buried geologic structures throughout much of the southern Albuquerque and northern Socorro basins. Furthermore, I present a unique case of teleseismic P-wave to Rayleigh wave conversion, which is a dominating feature along the western margin of the two basins. The dense instrument spacing makes it possible to detect these arrivals, which likely occur due to the strong impedance contrast between the rift basin sediments and bounding basement-cored fault blocks.

Table of Contents

1   Introduction

The Southern Albuquerque basin is a region in the central Rio Grande Rift (RGR) that is geologically complex and understood almost exclusively through surface observations. Two orogenies (the Ancestral Rocky Mountain and Laramide orogenies), active rifting, and active uplift from a midcrustal magma body create a unique area of geologic complexity with little geophysical coverage. New Mexico's largest metropolitan area resides in the northern portion of the Albuquerque basin, and as such, the north region of the basin has experienced much greater geophysical coverage than the southernmost portion (i.e. Connell and Grauch, 2013; Russell and Snelson, 1994, etc.).

Shallow seismic imaging of the southern Albuquerque basin was last conducted in the late 1970s (Brown et al., 1979; de Voogd et al., 1986), with deeper crustal studies conducted as recently as the mid-1990's to the early 2000's (Schlue et al., 1996; Gao et al., 2004; Wilson et al., 2005). Some recent studies have attempted to remedy the lack of basin imaging available (Folsom, 2017), or have fallen back on decades-old seismic data in combination with other geophysical methods (Connell and Grauch, 2013).

The goal of this work is to improve understanding of the crust and basin structure in the Southern Albuquerque basin using a dense, passive seismic array. The Sevilleta Array was deployed across the Sevilleta National Wildlife Refuge (SNWR) for two weeks in February of 2015. Approximately 800 vertical geophones captured local, regional, and teleseismic earthquakes during the deployment. In this thesis, I use teleseismic virtual reflection profiling (TVR), which capitalizes on recent innovations in dense-array processing methods to create virtual source reflection sections from records of

teleseismic events. The Sevilleta array imaged geologic structures best at depths that correspond to between ~1 and 5 s two-way travel time. The western half of the array is dominated by P-wave conversions to Rayleigh waves (P-to-Rg) from a north-south trending normal fault that delineates the western edge of the Albuquerque basin. Both exposed and buried structural complexities from local uplifts are resolved by TVR profiles. Features in this work agree well with previous geophysical studies and surface mapping. This work adds to the repository of geophysical studies in the area, expands knowledge of the Southern Albuquerque basin structures, and examines a unique case of body-to-surface wave conversions from teleseismic waves.

2   Geologic Overview

2.1   The Rio Grande Rift

The Rio Grande rift (RGR) is a Cenozoic continental rift that extends more than 1,000 km in length (Baldridge et al., 1984) and separates the Colorado Plateau to the west from the North American craton interior to the east (Hudson and Grauch, 2013) (Figure 1). The rift can be broken into three segments based on physiological features, as well as timing and structure: the south section (Chihuahua, Mexico to Socorro, NM) started rifting first at 32 Ma; the central section (Socorro, NM to Alamosa, CO) followed; and the north section (Alamosa, CO to Leadville, CO) started rifting at 27 Ma (Chapin, 1979). The RGR trends generally north-south, roughly following the structural grain of deformation from the Laramide (50 – 40 Ma) and Ancestral Rocky Mountain (approximately 300 Ma) orogenies, with slight direction changes by section (Chapin, 1979; Baldridge et al., 1995). Average extension in the RGR is modest, ~7 – 22% (Kelley and Chamberlin, 2012).

2.2   The Southern Albuquerque Basin

The Albuquerque basin is one of the largest basins in the RGR. The Albuquerque basin is flanked to the east by a series of three mountain ranges, from north to south: the Sandia Mountains, the Manzano Mountains, and the Los Piños Mountains. To the west, the Albuquerque basin is flanked by the Colorado Plateau and the Sierra Ladrones uplift. The SNWR, in which the Sevilleta array was deployed, sits between the Sierra Ladrones in the west and the Los Piños mountains in the east. The Albuquerque basin is constricted to the south by the Joyita Hills and Lemitar Mountains before opening into the Socorro basin. The Lemitar Mountains also separate the La Jencia basin to the east from the

Socorro basin. Extension is locally higher in this area than in the rest of the RGR, with totals as high as 170% in the area (Kelley and Chamberlin, 2012). The Rio Grande flows through the center of the basin in this area. From west to east, the major north-south normal faults with which the Sevilleta array interacts are the Silver Creek fault, the Loma Pelada fault, the Loma Blanca fault, the Cliff fault, the East Joyita fault, the Military Road fault, and the Los Piños fault. The Valle del Ojo de la Parida sits between Joyita Hills and the Los Piños mountains.

2.3 Western SNWR

The western half of the SNWR is structurally simpler than the eastern half: most of the structures in the area are normal faults associated with extension of the RGR. The only area of geologic complexity is the Cerritos de las Minas, which is a small eruptive center of late Oligocene or early Miocene andesite south of the Rio Salado (Machette, 1978). The dips of the normal faults in this half of the basin vary from low angle (~15°) to high angle (~80°), inciting an ongoing debate about the mechanism of fault rotation (Chamberlin, 1983; Ricketts et al., 2015). Both domino-style, in which fault and fault blocks simultaneously shallow, and rolling hinge, in which an outside fault shallows from isostatic rebound, have been attributed to the variety of fault dips in the region (Chamberlin, 1983; Ricketts et al., 2015).

All of the faults in the western half of the SNWR are Pleistocene, with the exception of the Silver Creek fault (SCf, Figure 1), which is late Miocene (Ricketts et al., 2015). The Loma Pelada fault (LPf, Figure 1), an east-dipping normal fault lies north of the Rio Salado in the SNWR and offsets Eocene, Oligocene, and Cretaceous volcanic and sedimentary rocks from Pleistocene, Pliocene, and Miocene sedimentary rocks and

4

alluvium in the basin (Connell and McCraw, 2007). South of the Rio Salado, offset across the Loma Pelada fault is less pronounced: Oligocene and Miocene rocks of the Cerritos de las Minas are separated from Pliocene and younger sands and sandstones (Machette, 1978). The Loma Blanca (LBf, Figure 1) and Cliff faults (Cf, Figure 1) exhibit minor offset of Pliocene and Miocene sedimentary rocks on both sides of the faults (Connell and McCraw, 2007; Machette, 1978). The Silver Creek fault offsets Oligocene rhyolite from Miocene sedimentary rocks (Cather and Read, 2003).

2.4   Eastern SNWR

The eastern half of the SNWR is more heavily faulted due to the Joyita Hills uplift, an area of heavy faulting and folding, with exhumed Precambrian gneiss at the center of an eroded anticline (de Moor et al., 2005)(Figure 1). The uplift records deformation from the Ancestral Rocky Mountain and Laramide orogenies, as well as normal faulting from Rio Grande rift extension (Beck and Chapin, 1994). A Laramide (Eocene) thrust-faulted anticline lies in the center, bounded by both west- and east-dipping normal faults (de Moor et al., 2005). The East Joyita fault is the major east-dipping detachment fault in the uplift, the splays of which offset Pennsylvanian through present day rocks and alluvium. Recent apatite fission track dating indicates that despite the extensive deformation, exhumation in the Joyita hills did not occur until the Miocene (Ricketts et al., 2015). The syncline from this uplift creates the Valle de la Joya (VJ, Figure 1), sometimes referred to as the La Joya basin, which sits directly east of the Joyita Hills uplift (Darton, 1921). A southward extension of the syncline, the Valle del Ojo de la Parida (VOP, Figure 1) separates the Joyita Hills to the west from the southern extent of the Los Piños Mountains to the east (Darton, 1921).

5

North of the Joyita Hills, the rest of the eastern SNWR is marked by a series of Pleistocene normal faults with one small eruptive center at the northernmost point (Machette et al., 2000). The Los Piños fault (LPf, Figure 1) acts as the main detachment fault for the Los Piños mountains, separating the alluvial fan from the 1.6 Ga Los Piños Granite and associated metamorphic rocks (Allen et al., 2014). The Military Road fault (MRf, Figure 1) is a north-south normal fault that cuts through the eastern side of Black Butte, an uplifted andesitic basalt just north of the SNWR (Rinehart et al., 2014). The Military Road fault is a recently discovered fault and may contain splays that are buried in the alluvium of the area (David Love and Richard Chamberlin, personal communication). Outside of offsetting basaltic andesite at both the surface and in the subsurface north of Black Butte (David Love and Richard Chamberlin, person communication), little is known about the Military Road fault.

2.5   Geophysical Studies and the Socorro Magma Body

At 19 km depth and 100 – 150 m thick, the Socorro magma body (SMB) is an active mid-crustal magma sill (Sanford et al., 1977; Rinehart et al., 1979; Ake and Sanford, 1988; Balch et al., 1997). Covering ~3400 km^2, the SMB is thought to be responsible for the high rates of seismicity and active uplift in the area overlying the magma body's known extent (Figure 1)(Sanford et al., 1977; Balch et al., 1997; Fialko and Simons, 2001). Assessment of local seismic anomalies characterized the parameters of the SMB from New Mexico Tech's permanent seismic network (Sanford et al., 1977; Rinehart et al., 1979; Ake and Sanford, 1988; Balch et al., 1997). Geodetic studies involving InSAR have found uplift rates of ~2 mm/year above the magma body, a rate

which is incompatible with inflation models for such a thin sill (Fialko and Simons, 2001; Finnegan and Pritchard, 2009; Pearse and Fialko, 2010).

Most geophysical studies completed in the Southern Albuquerque basin since 1965 have been executed in search of more information on the SMB. COCORP collected a ~155 km transect of 24-fold multi-channel seismic reflection data near the northeastern SNWR in 1975 and 1976 (Brown et al., 1979; Jurdy and Brocher, 1980; Brocher, 1981; de Voogd et al., 1986). Alongside a buried horst, a discontinuous, high-amplitude reflector provides evidence of the SMB at 19 km depth (Brown et al., 1979), indicating that the magma body consisted of multiple small layers that separate and recombine laterally (Brocher, 1981). Sheetz and Schlue (1992) used teleseismic receiver functions to investigate a possible magmatic source for the magma body, leading to the hypothesis of a series of feeder dikes. A localized anomaly in teleseismic P-wave arrivals led Schlue et al. (1996) to hypothesize a prismatic crustal root for the SMB. Folsom (2017) completed a magnetotelluric (MT) survey along the same road as the Sevilleta array Alamillo line, but was unable to find evidence of the SMB due to the magma body's low conductivity-thickness product and a "screening effect" from the overlying basins.

3 Data & Methods

3.1 The Sevilleta Array

The Sevilleta Array was a dense, passive seismic array deployed as a part of the Sevilleta Socorro Magma Body experiment in the SNWR in 2015. Deployment was a joint effort between the University of New Mexico, New Mexico Tech, Colorado State University, IRIS-PASSCAL, and NodalSeismic. The goals of the experiment were to study the Socorro magma body and the basin structures above the magma body. Seven broadband stations were also deployed during the experiment. The array was active from February 11th to February 25th and was composed of approximately 800 vertical component 10-Hz FairfieldNodal ZLand geophones. Station spacing was an average of 300 m on existing roads in the SNWR.

3.2 Teleseismic Virtual-Source Reflection Profiling

Teleseismic virtual-source reflection profiling (TVR) uses the reflection of the teleseismic P-wave off of the free surface of the Earth as a "virtual" seismic source. (Yu and Schuster, 2001) (Figure 2). Dense arrays recording PpPdp phases can be used to construct seismic profiles that imitate conventional seismic reflection profiles (Tseng and Chen, 2006; Yang et al., 2012). Sometimes known as vertical receiver functions (Schmandt and Clayton, 2013) or P-wave receiver functions (Tseng and Chen, 2006), the first successful use of TVR was imaging Moho arrivals in southern India's Archean crust with vertical component instruments (Tseng and Chen, 2006). Previous TVR studies targeting basin and shallow structure have been successful in the Bighorn and Powder River Basins in north-central Wyoming (Yang et al., 2012) and in the Three Gorges Region of China (Zou et al., 2014). Both studies used 4.5 Hz vertical component

geophones to resolve basin structure down to 10 km depth. This study is one of the first to use higher frequency (10 Hz) instruments for this method.

The TVR method can be broken down into four steps: event selection, trace alignment, source pulse deconvolution, and stacking (Figure 3). For event selection, the TVR method favors deep events (>~10 km) with a short and simple source pulse because shallow events (10 km or less) can have source-side scattering and pP and pS phases arriving with PpPdp phases (Zou et al., 2014; Yu et al., 2013). Teleseismic events (azimuthal distances of 30° – 80°) are used because those closer than 30° triplicate at upper mantle discontinuities (Zou et al., 2014; Stähler et al., 2012) and those greater than 80° may contain reflections off the core (PcP) that can cause interference (Tseng and Chen, 2006). Of the 34 teleseismic earthquakes that occurred during the deployment, the array picked up ten events. Three events matched the previous criteria with good signal-to-noise, and two events with fair signal-to-noise ratio (Table 1). Prior to alignment, I down-sampled each event from 250 to 20 samples per second. I filtered each event using a Tukey window with a 9% taper. All of the events except the M5.1 from Colombia were bandpass filtered from 0.2 – 3 Hz; the M5.1 from Colombia was bandpass filtered from 0.1 to 2 Hz.

For alignment of the P-arrival, I first applied a reduction velocity before determining a more precise alignment with multiple cross-correlations (Figure 3A). Plotting a reduced travel time of a headwave, such as the teleseismic P-wave in this study, is done by applying the following equation:

$$time_{reduced} = time - \frac{distance}{velocity_{reduction}}$$

I visually estimated the reduction velocity by sorting the traces of the array by distance

from the earthquake source and determining the time of the P-wave move out, then

applied the velocity to the above equation. This approximate alignment creates a smaller

signal window and makes the cross-correlation more efficient. Prior to cross-correlation,

I bandpass filtered a copy of each event from 0.2 to 1.2 Hz, except for the M5.4 from

Russia, which I filtered to 0.3 to 1.7 Hz. Filtering with a smaller bandpass made the

signal slightly clearer for better alignment, however, I applied the time shifts from cross-

correlation to both the lower frequency copy of the traces and a higher frequency (0.2 – 3

Hz) copy of the traces that is later used in deconvolution. During cross-correlation, every

trace is compared to every other trace to determine a median time and individual lag

times in order to closely align the direct P arrival. Cross correlation utilizes the integral

$$C(L) = \lim_{T \to \infty} \frac{1}{T} \int_{-\frac{T}{2}}^{\frac{T}{2}} x(t)f(t+L) \, dt$$

where *f (t)* is the peak of interest in the signal, *x(t)* is the rest of the signal, and *f (L)* is the

"lag time" to shift the signal (Stein and Wysession, 2003). After the initial cross-

correlation and subsequent alignment, I repeated the process two more times with a lag

time limitation of 10 samples and then 6 samples, tightening the P-wave alignment

(Figure 3B).

I estimated the source pulse by averaging all the traces for each event. This

process enhances the direct P-wave and reduces or removes scattered arrivals (Zou et al.,

2014). The source pulse length was determined by trial and error. Similar to previous

studies (Tseng and Chen, 2006; Yang et al., 2012; Zou et al., 2014), I tested various

source lengths and tapered source pulses as well as full trace deconvolutions (Figure 4).

For each of the events, I used tapered, simple sources that varied in length from 2 to 7 s

for the final deconvolution. The simplest wavelet is usually the most appropriate (Zou et

al., 2014) as reverberations appear if the wavelet is too long, and the receiver function is

too noisy if the wavelet is too short (Zou et al., 2014). Yang et al. (2012) removed the

basin traces to avoid basin reverberations interfering with the source pulse. We tested

both the full array and only non-basin traces and found little difference in the resulting

deconvolved TVR profiles.

In general, deconvolution separates two or more components of a signal from one

another (Stein and Wysession, 2003). Our observed signal can be expressed as $(t) = (t) *$

(t) where $d(t)$ is the observed signal, $g(t)$ is a known function of the signal, and $m(t)$ is the

unknown function. In this study, $m(t)$ is the geologic response and $g(t)$ is the source

wavelet. In order to find the geologic response, the source wavelet must be removed from

the observed signal, resulting in $(t)/(t) = m(t)$. To do this, I used a water-level spectral

deconvolution to create each event's TVR profile. Water-level spectral deconvolution

creates a resulting response that is proven to be both accurate and stable (Clayton and

Wiggins, 1976). The source pulse and traces were converted to the frequency domain

from the time domain using a fast Fourier transform (Stein and Wysession, 2003). The

water-level adjustment is performed on the spectral source signal; water-level here refers

to a chosen minimum absolute amplitude value below which lower values will be

adjusted to the chosen water-level (Clayton and Wiggins, 1976). Choosing a water-level

prevents very small values from being divided in the final spectral division, which would

create anomalously large numbers for the final profile. I chose a water-level that was

10% of the maximum of the source spectra. Once the lowest values have been adjusted, the overall trace can be divided by the source, and then converted back into the time domain. The spectral division can amplify noise, so performing a bandpass filter on the resulting deconvolution helps to stabilize the response (Clayton and Wiggins, 1976). I filtered the deconvolved traces from 0.25 to 1.5 Hz with a first-order zero-phase Butterworth filter. Once deconvolution is complete, the remaining traces are that event's TVR profile (Figure 3C).

In order to examine frequency sensitivity and azimuthal differences, I binned frequencies and separated my events into either the 'southeast' or 'northwest' category based on azimuthal angle from the array before stacking. I band-pass filtered each event into eight frequency bins: 0.1 – 0.5 Hz, 0.5 – 1.0 Hz, 1.0 – 1.5 Hz, 1.5 – 2.0 Hz, 2.0 – 2.5 Hz, 2.5 – 3.0 Hz, 3.0 – 3.5 Hz, and 3.5 – 4.0 Hz. The southeast events are the two Colombia and one Argentina earthquakes. The northwest events are the Russia and Japan earthquakes. I stacked each of the southeast events together and each of the northwest events together to create azimuthal stacks. I also created a full stack of all of the events in order to examine the overall TVR profile without azimuthal bias. Due to the degrading signal-to-noise ratios (Figure 5), only the following bins will be discussed in detail in the results: 0.1 to 0.5 Hz, 0.5 Hz to 1.0 Hz, and 1.0 to 1.5 Hz.

I calculated estimated depth profiles using several sources for velocity control. Shallow velocities are based off of wells presented in Brocher (1981). I used 2.5 km/s for a P-wave velocity for the Santa Fe group, which is the most pervasive surface formation. For deeper velocities, I used the S-wave velocity model determined by Ranasinghe et al.,

(accepted), which was based off of the Sevilleta array and converted to P-wave velocities using the empirical relationship of Brocher (2005).

3.3   Forward Modeling

To aid in the identification of phases in the TVR profiles, I utilized recent advancements in forward modeling. Synthetic seismograms were created based off of the 2-D finite difference elastic wave propagation algorithm developed by Duru et al. (2014) and implemented by Hansen and Schmandt (2017) in MATLAB. I created simple homogenous velocity layers, testing a variety of basin-bounding fault dips (Table 2, Figures 6A-D) and impedance contrasts between the basin and the crust (Figures 6E,F). Differences between the models are described in Table 2, with corresponding basin models in Figure 6. The boundary between the upper mantle layer and the crustal layer was always at ~31 km depth. Velocities and densities for the upper mantle and crust were based off of previously implemented models by Hansen and Schmandt (2017); upper mantle velocities were 7.8 km/s for Vp and 4.2 km/s for Vs, and crustal velocities were 6.3 km/s for Vp and 3.6 km/s for Vs. Upper mantle density was 3.3 g/cm^3 and crustal density was 2.75 g/cm^3. The corner frequency for all of the models except Basin 6 was 1 Hz, with an incoming incident plane wave slowness of 0.06 s/km. Basin 6 (Figure 6F) has a corner frequency of 1.2 Hz, to more accurately match the frequency of the observed Rayleigh phase.

4   Results

The Sevilleta array consisted of 17 lines, varying in length from under 4 km to more than 20 km. I have organized the results by geographical quadrant, as each quadrant has common geologic features. The Rio Grande River divides the array into west and east sections, and the Rio Salado River divides the western half of the array into north and south sections. Each line is named after the road on which the line was recorded. In each line's section, I detail observations from the full event stack observation, and follow with a summary of how the images change with different frequency bands. As outlined in the *Methods* section, the frequency analysis was performed using separate stacks from the northwest events (Russia, Japan) and the southeast events (Argentina, Colombia M5.5, Colombia M5.1) in order to investigate azimuthal effects in tandem with frequency effects.

4.1   Northwestern Quadrant

4.1.1   ATT Line

The ATT line runs west-to-east from the base of the Sierra Ladrones uplift into the Southern Albuquerque basin (Figure 7). The dominating feature of this line is a high amplitude, steeply east-dipping series of arrivals (Figure 8 – green). These arrivals are observed up to ~25 s deep before disappearing off the eastern edge of the profile. The other distinct feature in this line is a strong reflector at ~3 s starting at ~8 km along the profile (Figure 8 – red), which is paralleled above at ~2 s (Figure 8 – blue). This feature dips slightly eastward for the easternmost 2 km but is otherwise relatively flat. Very shallow arrivals (< 1 s) vary in depth along the profile both before and after the series of intense arrivals (Figure 8 – yellow).

14

4.1.1.1 Frequency analysis

For the events from the northwest, the shallow, east dipping reflector that dips from ~3 km along profile to the east end of the profile has slight variations in slope that change with frequency (Figure 9A-C). The shallowest slope at 0.1 to 0.5 Hz and 1.0 to 1.5 Hz is from 12 to 14 km along profile (at ~3 s)(Figure 9A,C). At 0.5 to 1.0 Hz, the shallowest slope is actually between 3 and 5 km along profile (at ~1 s), followed by 12 to 14 km (Figure 9B). From ~6.5 km to 14 km along profile, each frequency band bin has a different number of arrivals. At 0.1 to 0.5 Hz, there is one flat arrival at ~3 s (Figure 9A). At 0.5 to 1.0 Hz, there are three parallel arrivals at approximately 2, 3, and 4.2 s (Figure 9B). At 1.0 to 1.5 Hz, there is one low amplitude arrival at 1.5 s, followed by three subparallel, higher amplitude arrivals at 2.5, 3.3, and 4 s (Figure 9C). The high amplitude series of steeply east-dipping arrivals between 2 and 8 km along profile have similar slopes from 0.1 to 1.0 Hz. From 1.0 to 1.5 Hz, the arrivals are less continuous. Additionally there is high amplitude signal in the first 3 km of the profile that is not present in the lower frequency bins, which is discontinuous and arrives as late as 8 s.

For the events from the southeast, all three frequency bins have a reflector at ~3 s from 8 km along profile to the east end of the profile (Figure 9D-F). At 0.1 to 0.5 Hz, this reflector is accompanied by an earlier, subparallel, lower amplitude arrival at ~2 s (Figure 9D). At 0.5 to 1.0 Hz, the aforementioned earlier arrival is as high amplitude as the main reflector, with a third, lower amplitude arrival at ~4.2 s (Figure 9E). At 1.0 to 1.5 Hz, there are once again two arrivals – the main reflector at 3 s and a second, parallel arrival at 2 s (Figure 9F). A series of short (< 2 km horizontal distance) arrivals appear every second on the second on the west end of the line, down to 9 s. The steeply east-dipping

15

high amplitude arrivals seen in the northwest stacks are present in the southeast stacks, but are difficult to distinguish at 1.0 to 1.5 Hz.

For events from both azimuths, the prominent reflector from 8 km eastward arrives at 3 s on the stacks. From the northwest, there is a distinct 0 to 3 s east-dipping reflector that lines up with the aforementioned 3 s reflector. In both azimuths, parallel to sub-parallel arrivals accompany the 3 s reflector. The steeply east-dipping series of arrivals are present from both azimuths, but are more continuous from the northwest at 1.0 to 1.5 Hz (Figure 9C). At 1.0 to 1.5 Hz, both azimuths feature a block of high amplitude signal in the first 2 km of the profile.

4.1.2   *Popotosa Line*

The Popotosa Line approaches the eastern edge of the ATT line from the southwest, covering nearly the same area south of the previous line (Figure 7). The same features that can be observed in the previous line appear in the Popotosa line (Figure 10). The dominating east-dipping series of arrivals is still very evident, but more muted (Figure 10 – green). Because this high amplitude arrival starts further east than in the ATT line, some flat arrivals can be seen in the western ~2 km of the line, at 2 s (Figure 10 – pink), and at slightly more than 3 s (Figure 10 – red). Similarly, the flat reflector that comes in at the eastern edge of the profile at ~2-3 s also appears in this line but is flatter and possibly dipping slightly east (Figure 10 – red). Around 6 km across the profile, there is a shallow (< 2 s), east-dipping arrival that does not appear in the ATT line (Figure 10 – blue).

4.1.2.1 Frequency analysis

For the events from the northwest, the northeast-dipping reflectors that start at 5 km along profile and extend to the end of the profile have similar slopes from 5 to 10 km along profile and again from 10 km to the end of the profile from 0.1 to 1.0 Hz (Figure 11A, B). At 1.0 to 1.5 Hz, the slope of the reflector after 10 km is difficult to see (Figure 11C). Faint arrivals before and after the main reflector at 0.1 to 0.5 Hz become higher amplitude at 0.5 to 1.0 Hz (Figure 11A, B). At 1.0 to 1.5 Hz, the higher amplitude arrivals are only from ~6 km to 11 km along profile (Figure 11C). Steeply northeast-dipping arrivals starting at ~2 km along profile appear to be very similar at 0.1 to 1.0 Hz. At 1.0 Hz to 1.5 Hz, the arrivals resolve into a series of arrivals. Like the AT&T Line, another series of high amplitude arrivals appears in the first 2 km of the profile and continues from 0 to 6 s.

For events from the southeast, both the steeply northeast-dipping arrivals starting at 2 km along profile and the flat arrivals at 2 and 3 s increase in amplitude and decrease in noise from 0.1 to 0.5 Hz to 0.5 to 1.0 Hz (Figure 11D, E). At 1.0 to 1.5 Hz, both sets of arrivals become less continuous, and the steeper arrivals become difficult to distinguish from noise (Figure 11F). The first 3 km of the profile contain a high amplitude series of arrivals that go to the bottom of the profile.

The northeast-dipping reflector in the northwest stack that starts at 5 km along profile and goes as deep as 3 s in the northeast end of the profile appears solely as a completely flat reflector at 3 s in the southeast. The steeply northeast-dipping arrivals that start at 2 km along profile are less noisy from the northwest. Similarly, at 1.0 to 1.5 Hz,

the arrivals are far more continuous and high amplitude from the northwest than the southeast (Figure 11C, F).

4.1.3   Jack Well Line

The Jack Well line trends northeast-southwest before bending more directly north-south at around 3 km along the line (Figure 7). In the uppermost 2 s of this line, a consistent series of high frequency signal is apparent in the southern half (Figure 12 – yellow, red). In the northern half of the line, most of the signal is muted until ~3 s, where one of the strongest signals arrives, dipping gently to the north (Figure 12 – red). Below that, another signal dips more steeply to the north, going from 5 s at 0 km to just past 4 s at 4 km along the profile (Figure 12 – pink). The south region generally contains flat or very gently north-dipping arrivals. Below 10 s, a series of high amplitude arrivals again dominates the line (Figure 12 – green).

4.1.3.1   Frequency analysis

In the northwest events, an arrival at ~3 s from 4 km along profile to the end of the line at 0.1 to 0.5 Hz splits into two distinct arrivals at 0.5 to 1.0 Hz (Figure 13A, B). At 1.0 to 1.5 Hz, across the same horizontal distance, a high amplitude series arrives from 0 s down to 3 s (Figure 13C). A shallowly north-dipping arrival between 4 and 5 s from 0 to 5 km along profile gets increases in amplitudes as frequency bands increase (Figure 13A-C).

The aforementioned arrival in the northwest stack is also present in the southeast stack, with higher amplitudes at 0.5 to 1.0 Hz than 0.1 to 0.5 Hz (Figure 13D, E). Later arrivals (5+ s) that appear high amplitude at 0.1 to 0.5 Hz decrease amplitude with increasing frequency in the southeast events. The north-dipping reflector mentioned in

18

the northwest stack becomes discontinuous and lower amplitude at 1.0 to 1.5 Hz (Figure 13F).

At 0.1 to 0.5 Hz, the arrivals at 3 to 6 s are higher amplitude from the southeast than the northwest (Figure 13A, D). At 0.5 to 1.0 Hz, the northwest profiles are generally noisier than the southeast profiles (Figure 13B, E). However, at 1.0 to 1.5 Hz, the northwest has more continuous arrivals and better signal to noise than the southeast (Figure 13C, E).

4.2   Southwestern Quadrant

4.2.1   *West Mesa Line*

The West Mesa line runs from north to south in the La Jencia basin and is the westernmost line of the array (Figure 14). The first arrival comes in at ~1 s, blending into the direct P-wave arrival after about 2.5 km across the profile (Figure 15 – yellow). Arrivals at ~1.5 and ~2.5 s remain flat and seemingly uncomplicated throughout this line (Figure 15 – blue and red). An arrival coming in at ~3 s on the northern end discontinues after about 1.5 km along the profile (Figure 15 – pink). Similarly, another high amplitude arrival close to 5 s discontinues around 1.5 km (Figure 15 – purple).

4.2.1.1   *Frequency analysis*

In the records of events from the northwest, high amplitude arrivals across the profile between 0 and 2 s split at 0.1 to 0.5 Hz split into two arrivals at 0.5 and 1.6 s at 0.5 to 1.0 Hz (Figure 16A, B). At 1.0 to 1.5 Hz, the arrivals are difficult to see due to an overall increase in amplitude in the first 6 s across the whole profile (Figure 16C).

Like the northwest events, the southeast features a high amplitude arrival for the first 2 s across the whole profile at 0.1 to 0.5 Hz. This arrival splits into two arrivals (at 0.6 and 1.6 s) between 1.8 and 3.2 km along profile (Figure 16D). At 0.5 to 1.0 Hz, the arrival is fully separated into high amplitude arrivals at the same times as the aforementioned split section (Figure 16E). At 1.0 to 1.5 Hz, the line again becomes noisy for the first 6 s (Figure 16F). The northwest and southeast stacks are very similar, but the southeast stack has overall higher amplitude signal.

4.2.2   Alamillo Line

The Alamillo line runs west to east along the western margin of the Socorro basin, just north of the Lemitar Mountains (Figure 14). The most striking series of arrivals here is on the eastern edge of the line, after 11 km: the upper 5 s of arrivals appear to dip east (Figure 17 – green). West of that, there is a relatively uniform series of flat-lying arrivals at ~1.5 s (Figure 17 – blue) and again at ~3 s (Figure 17 – red). Shallow (< 1 s) arrivals in the first 6 km along the profile appear to shallow very gently moving east (Figure 17 – yellow).

4.2.2.1   Frequency analysis

For the northwest events, an arrival at 1.7 s from 5 to 11 km along profile is more consistent at 0.5 to 1.0 Hz than 0.1 to 0.5 Hz (Figure 18A, B). In the first 2 km of the profile, an arrival at 4.5 s is higher amplitude at 0.5 to 1.0 Hz than 0.1 to 0.5 Hz (Figure 18A, B). An arrival at ~3 s between 6 and 10 km along profile in lower frequency bins separates into two parallel arrivals at 2.5 s and 3.3 s at 1.0 to 1.5 Hz (Figure 18C). In 0.1 – 0.5 Hz and 0.5 – 1.0 Hz, arrivals on the east end of the profile begin to dip at ~10.5 km along profile, with dipping beginning after the initial P-arrival and continuing off the

20

profile range (Figure 18A, B). In the 1.0 – 1.5 Hz bin, dipping begins at 10 km along profile, with each arrival only continuing for ~1.8 km before terminating (Figure 18C).

For the southeast events, an arrival that frequently merges into a single peak across the entire profile from ~0.2 to 1.9 s at 0.1 – 0.5 Hz splits into two coherent arrivals at ~0.5 and 1.7 s respectively (Figure 18D). The latter arrival (1.7 s) has two points at which the arrival time is earlier – at ~2.1 km and ~7.8 km along profile. At 1.0 – 1.5 Hz, two separate arrivals at 0.2 s and 0.8 s merge into one high amplitude arrival at ~5 km along profile (Figure 18F). The arrival at 1.6 s is much flatter and consistent along profile. An arrival at 2.9 s across the entire profile increases amplitude at 0.5 – 1.0 Hz (Figure 18E). At the east end of the line, dipping arrivals begin from the initial P-arrival at ~11.5 km along profile at 0.1 – 0.5 Hz and ~10.5 km along profile at 0.5 – 1.0 Hz. However, in 1.0 – 1.5 Hz, dipping reflectors don't begin until below 2 s, ~10.2 km along profile.

The events from the southeast contain a series of flat arrivals that gets clearer with increased frequency (Figure 18D-F). From the northwest, arrivals appear to be gently dipping east and are overall noisier (Figure 18A-C). The dipping arrivals in the northwest events dip directly from the initial P-wave arrival whereas the southeast events have a 2 s delay at 1.0 to 1.5 Hz (Figure 18C, F).

4.2.3   Powerline Line

The Powerline Line runs north-south completely within the Albuquerque basin, east of the Loma Pelada fault (Figure 14). This line is visually dominated by a series of high amplitude arrivals, which appear to dip gently to the north (Figure 19 – green). These arrivals obscure most of the shallower arrivals, which appear as higher frequency

on the north end of the line, from 0 to ~1.5 km. The arrivals before 2 s appear to be

dipping very gently northward until coalescing with the direct P-wave arrival around 4

km along the profile (Figure 19 – yellow).

4.2.3.1   Frequency analysis

In records of the northwest events, a shallowly north-dipping arrival in the first

three seconds of the whole profile decreases amplitude from 0.1 to 0.5 Hz to 0.5 to 1.0

Hz (Figure 20A, B). The later arrivals appear unchanged between 0.1 and 1.0 Hz, and

become noisy at 1.0 to 1.5 Hz (Figure 20C).

In the southeast events, at 0.1 to 0.5 Hz, a flat arrival at 2 s which disappears after

1.5 km then increases in amplitude at 0.5 to 1.0 Hz, extending to 2.5 km along profile

(Figure 20D, E). One section from 2.5 to 4.5 km along profile of the shallowly north-

dipping arrivals from 3 to 4 s resolves from one arrival at 0.1 to 0.5 Hz to two arrivals at

0.5 to 1.0 Hz (Figure 20D, E). Again, this series of arrivals becomes noisy and indistinct

at 1.0 to 1.5 Hz (Figure 20F).

The northeast-dipping arrival at ~8 s is less continuous from the southeast than

the northwest. Both azimuths have degrading signal-to-noise ratios at frequencies above

1.0 Hz.

4.2.4   Esquival Line

The Esquival line is a relatively short (~4.5 km), northwest-southeast line that sits

fully inside the Socorro basin (Figure 14). Starting at 0.8 km along profile, there are flat-

lying arrivals around 2.3 s, but are delayed ~0.5 s between 2.7 km and 4.2 km (Figure 21

– red). A dipping set of arrivals appears on the southeast end of the line in the last km,

dipping northwest between 4 s and 5.5 s (Figure 21 – pink). Like previous lines, a series

of high amplitude arrivals crosses the line with varying apparent dips, but generally east-dipping at ~4 to 10 s (Figure 21 – green).

4.2.4.1 *Frequency analysis*

In the northwest events, both 0.1 to 0.5 Hz and 0.5 to 1.0 Hz have strong arrivals at ~3.8 s from 0 to 2 km along profile (Figure 22A, B). At 0.1 to 0.5 Hz, this signal continues to 4 km (Figure 22A). The profile is very noisy above 1.0 Hz, with the highest amplitudes occurring between 3 and 6 s (Figure 22C).

In the southeast events, the 0.5 to 1.0 Hz bin has so much noise that any signal seen in the 0.1 to 0.5 Hz bin is difficult to find in 0.5 to 1.0 Hz (Figure 22E). Additionally, 1.0 to 1.5 Hz is noisy, like in the northwest stack, but the highest amplitudes arrive early, between 0 and 3 s (Figure 22F).

A high-amplitude arrival at 3.8 s is less prominent from the southeast than the northwest. The southeastern profiles are overall noisier. At 1.0 to 1.5 Hz, the strongest signals arrive earlier from the southeast than the northwest (Figure 22C, F).

4.3   Eastern Half

4.3.1   *Firebreak Line*

The Firebreak line is a west-east line on the Joyita bench, just east of the Los Piños Mountains (Figure 23). The eastern edge of the line features a short series of west-dipping arrivals that abruptly stop around 7 km along the profile (Figure 24 – green). The middle of the line (2 – 7 km along profile) hosts a relatively flat arrival at 2.7 s (Figure 24 – red). The very easternmost shallow arrivals (~1.2 s) appear to be continuous from ~0-3 km along profile, after which they disappear (Figure 24 – yellow).

23

4.3.1.1 Frequency analysis

There are very minor differences between the frequency bins for events originating to the northwest. In 0.1 to 0.5 Hz, the east-dipping arrival at ~1.5 s from 5.5 to 7.5 km along profile is slightly steeper and higher amplitude than 0.5 to 1.0 Hz (Figure 25A, B). At the east end of the profile, from 9 km along profile to the end the arrival that goes down to ~6 s is more continuous at 1.0 to 1.5 Hz than the other frequency bins (Figure 25C).

The west-dipping arrival in the southeast events starting at 1 s on the eastern end of the profile down to ~5 s at 2.5 km along profile appears to be higher amplitude in 0.5 to 1.0 Hz than the other frequency bands (Figure 25E). At 1.0 to 1.5 Hz, the aforementioned arrival becomes a series of fairly continuous arrivals (Figure 25F). On the western half of the profile, this series of arrivals goes from 0 s down to 7 s. Unlike the northwest profiles, the southeast profiles have a strong west-dipping arrival that arrives as late as ~5 s at 2.5 km along profile.

4.3.2 McKensie North Line

The McKensie North Line trends northwest-southeast on the Joyita bench (Figure 23). A flat signal at ~2.7 s shows up fairly consistently between 1 km and 2.5 km along the profile (Figure 26 – red). Between 2.5 km and 5 km along the profile an arrival dips to the northwest, dipping from 2.6 s to 3.8 s over the 2.5 km (Figure 26 – orange). Past this, the signal continues to arrive flat at 2.7 s until 6 km along profile where there is smaller northwest-dipping arrival between 2.7 and 3 s. From 7 km to the southeast end of the profile, the signal resumes arriving at 2.6 s (Figure 26 – yellow).

4.3.2.1 Frequency analysis

In events from the northwest, a low amplitude signal dips west from 3 to ~6 s from 3 km along profile to the eastern edge of the profile at 0.1 to 1.0 Hz (Figure 27A, B). At 1.0 to 1.5 Hz, this arrival becomes higher amplitude and slightly less noisy (Figure 27C). At 0.5 to 1.0 Hz, there is a shallowly east-dipping arrival between 1 and 2 s from 3 km along profile to the east end of the profile (Figure 27B). This same arrival appears at 1.0 to 1.5 Hz, but is flat all the way across the profile at ~0.7 s with a second, east-dipping arrival beginning at 6 km along profile until the east end of the line (Figure 27C). The arrival does not appear at 0.1 to 0.5 Hz.

In the southeastern events, there is a west-dipping arrival with good signal-to-noise arriving between 2 and 6 s from 2 to 6 km along profile. At 0.1 to 1.0 Hz, there are two arrivals ~1.5 s apart (Figure 27D, E). At 0.5 to 1.0 Hz, the earlier arrival extends as far east as 7 km along profile (Figure 27E). From 1 to 2 km along profile, the aforementioned arrivals are flat with only the earlier (~4 s) arrival being high amplitude at 0.1 to 1.0 Hz. At 1.0 to 1.5 Hz, there is no clear west-dipping signal, but the arrivals between 1 and 2 km along profile have become a series of arrivals from 0 to 7 s that appear to shallow dip east (Figure 27F).

There is less signal across all frequencies from the northwest, whereas there is a fairly distinct west-dipping arrival from the southeast.

4.3.3   McKensie South Line

The McKensie South line trends northwest-southeast ~12 km south of the McKensie North line (Figure 23). Prominent features detected in both the northwest and southeast event TVR profiles are not as clear in the full event stacks for this line. As

25

such, the azimuth-based TVR profiles are presented separately alongside the full stack (Figure 28). On the northwest end of the line, shallow (~1 s) arrivals appear to dip southeast very gently from 1.5 km to 3 km (Figure 28 – pink). On the southeast end of the line, steep arrivals dip from 1.5 s to 4.2 s from 10 km to 7.5 km (Figure 28 – green). Between 2 and 6 km, there is a flat arrival at ~2.7 s (Figure 28 – red).

4.3.3.1   Frequency analysis

The east-dipping arrival in events originating to the northwest from ~2 km along profile eastward becomes less noisy at 0.5 to 1.0 Hz than 0.1 to 0.5 Hz (Figure 29A, B). At 1.0 to 1.5 Hz, the west-dipping arrival that starts at 1 km at previous frequencies starts 0.5 km along profile (Figure 29C). This arrival becomes a series of arrivals that last approximately 2 s.

The west-dipping arrival in the southeastern events from 2 s at 9 km along profile to 3 s at 4 km along profile is higher amplitude at 0.5 to 1.0 Hz than 0.1 to 0.5 Hz (Figure 29D, E). At 1.0 to 1.5 Hz, this arrival marks the bottom edge of a high-amplitude series of arrivals (Figure 29F). The profiles from the northwest appear to feature a series of east-dipping arrivals whereas the southeast profiles seem to mark a valley – both east- and west-dipping arrivals

4.3.4   Red Well Line

The Red Well line runs west-east for ~6 km (Figure 23). The most dominating feature here is an east-dipping arrival that starts near the P-arrival on the west end of the line and dips down to 3.2 s after 3.5 km (Figure 30 – pink). A flat-lying arrival at ~1.2 s is consistent across the rest of the line (Figure 30 – yellow).

4.3.4.1 Frequency analysis

In the northwestern events, an arrival appears to be flat from 0 to 1.5 km along

profile at 3 s, before dipping to the east from 1.5 km to 3 km along profile, down to 4 s at

0.1 to 0.5 Hz (Figure 31A). At 0.5 to 1.0 Hz, this arrival goes from 2 s at 0 km to 4 s at 3

km, dipping east during the entire 3 km (Figure 31B). At 1.0 to 1.5 Hz, this east-dipping

arrival is preceded in time by a series of high amplitude arrivals (Figure 31C).

In events originating to the southeast, an east-dipping arrival in the first 1.5 km of

the profile is high amplitude at 0.5 to 1.0 Hz than 0.1 to 0.5 Hz (Figure 31D, E). At 1.0 –

1.5 Hz, the profile is very noisy but the arrivals in the first 2 km still have an east-dipping

pattern (Figure 31F). The western half's east-dipping arrival extends further horizontally

and has higher amplitude from the northwest than the southeast.

4.3.5 Palo Duro Line

The Palo Duro line is the western north-south line in the eastern half and the

longest line in the array at ~25 km (Figure 23). The first km of the line has arrivals at ~1

and ~2 s dipping to the north (Figure 32 – blue). The ~1 s arrival dips south to 2 s from 1

km to 2.5 km along the profile before flattening out (Figure 32 – yellow). At 4 km along

the profile, another arrival dips again from the P-wave arrival to 1.5 s southward then

flattening out at 6.5 km (Figure 32 – pink). The flat section of that arrival increases in

amplitude at 7.5 km along the profile until 12 km. At 12 km, the arrival angles up to ~1.1

s and then drops back down to 1.5 s at 13.5 km. From 13.5 km to 16 km along the profile,

the arrival stays flat at 1.5 s, merges with the direct P-wave arrival at 16 km and gently

dips back down from 18 km to 22 km along the profile (Figure 32 – pink). Similar to

other lines in the eastern half of the array, much of the northern half of Palo Duro line has

a very consistent, flat arrival. At 11 km along the profile, the arrival dips down to ~3 s for

about a km and returns to 2.5 s for the rest of the line, although the arrival loses

amplitude from ~13-18 km along profile (Figure 32 – red).

4.3.5.1   Frequency analysis

An arrival in the first 1.5 s across the northwestern events profile resolves from

one large arrival with varying wavelengths from 0 to 20 km at 0.1 to 0.5 Hz (Figure 33A)

into 2 arrivals from 4 to 13 km at 0.5 to 1.0 Hz (Figure 33B). At 1.0 to 1.5 Hz, there are

two distinct arrivals across the entire profile within the first 1.5 s (Figure 33C). In the first

7 km of the profile, a series of short (~3 km horizontal) arrivals increases in amplitude

and decreases in noise as frequencies increase.

Like the northwestern profiles, an arrival within the first 1.5 s of the southeastern

events profile resolves into two arrivals from 0.1 to 0.5 Hz to 1.0 to 1.5 Hz (Figure 33D,

F). Arrivals at 2, 3, and 4 s in the first 5 km of the profile at 0.5 to 1.0 Hz splits into a

series of high amplitude arrivals that extends to 15 km along profile and down to 7 s

(Figure 33E).

The arrivals at 1.0 to 1.5 Hz on the north half of the profile are more continuous

and extend further horizontally from the southeast than the northwest (Figure 33C, F).

Both azimuths have an area of relative transparency between 2 and 4 s at 6 to 8 km along

profile at 0.1 to 1.0 Hz.

4.3.6   Gibbs Line

The Gibbs line runs southwest to northeast for 7 km before striking directly west

to east for the final ~3 km (Figure 23). On the south end of the line, an arrival is dipping

from ~1 s to 1.5 s, creating a north dip, from 0 to 1 km (Figure 34 – yellow). From 1 to 2

km, the arrival remains high amplitude and flat, but dips at 2.5 km down to 1.8 s and then back up to 1.5 s by 3.6 km along the profile. The arrival again stays flat and high amplitude until 6.5 km. The arrival drops from 1.5 to 4.5 s between 6.5 and 10 km (Figure 34 – yellow). Above this section of dip, shallow arrivals (< 1 s) follow the same trend, and dip from 0.8 s to 1.5 s, then return to coalesce with the P-wave by the east end of the profile (Figure 34 – pink). Like previous lines, there is a fairly consistent arrival at 2.7 s (Figure 34 – red). This lies flat from 0 to 8 km, at which point the arrival is cross cut by the previously mentioned dipping arrival.

4.3.6.1 Frequency analysis

From the northwest, an arrival at ~1.4 s from 0 to 7 km along profile is higher amplitude and more continuous at 0.5 to 1.0 Hz than 0.1 to 0.5 Hz (Figure 35B, A). At 1.0 to 1.5 Hz, there is a block of high amplitude arrivals down to 4 s that do not appear at lower frequencies (Figure 35C).

From the southeast, the north-dipping arrival becomes higher amplitude and less noisy as the frequency bands increase (Figure 35D-F). The north-dipping arrival arrives earlier from the northwest, but is less noisy from the southeast.

4.3.7 Tomasino Line

The Tomasino line runs west-east at the southernmost portion of the array (Figure 23). The upper 2 s of the line consist of multiple high-amplitude negative arrivals with little to no corresponding positive arrivals. Of this dense cluster of arrivals, there is a dipping arrival in the first 2 km that appears to dip east, going from 1 to ~1.5 s (Figure 36). At ~2 km, the same arrival dips steeply west, bringing the arrival back up towards the P-wave arrival.

4.3.7.1   Frequency analysis

Tomasino does not have any significant changes across the frequency bands,

outside of increased noise (Figure 37). There is a slight east-dipping arrival present from

the northwest (Figure 37A-C) that is not visible or discernable in the events from the

southeast (Figure 37D-F).

4.3.8   Sepultura Line

The Sepultura line runs north-south along the base of the Los Piños Mountains

(Figure 23). From 0 to 4 km along the profile, a series of high amplitude arrivals appears

from 0 to ~5 s (Figure 38 – green). From 4 to 9 km, the same series of high amplitude

arrivals intensifies, but only goes to ~3 s. At 12.5 km along the profile, a flat arrival

arrives at 1.5 s (Figure 38 – pink), continuing until 16 km where the arrival is disrupted

by a north-dipping arrival that goes from the P-wave arrival to 1.9 s between 17.5 km and

16 km along the profile (Figure 38 – yellow). From 17.5 km, another arrival dips up

(dipping to the north) from 2 to 1.2 s at 19 km (Figure 38 – blue); the arrival drops down

about 0.2 s to flatten out again at 1.5 s, continuing generally flat until the south end of the

profile. The 2.5/2.7 s arrival seen in most of the other lines of the array appears in the

Sepultura line again starting at 11 km (Figure 38 – red). The arrival goes through some

minor (+/- 0.3 s) variations in the same region of the previously mentioned dipping

arrivals, ~14 km to 20 km along the profile, before flattening out to the end of the south

end of the profile.

4.3.8.1   Frequency analysis

In the northwest events, there is a shallowly north-dipping arrival from 6 to ~16

km along profile at 2 to 2.5 s (Figure 39A-C). This arrival is higher amplitude at 0.5 to

1.0 Hz than 0.1 to 0.5 Hz (Figure 39B, A). At 1.0 to 1.5 Hz, the arrival becomes a series

of high-amplitude arrivals (Figure 39C).

In the southeast events, a relatively flat-lying arrival across the entire profile at

~2.8 s is again higher amplitude with less noise at 0.5 to 1.0 Hz than 0.1 to 0.5 Hz (Figure

39E, D). Similarly, the arrival becomes a series of high amplitude arrivals at 1.0 to 1.5 Hz

(Figure 39F). The north-dipping arrival visible from the northwest events is either not

present or lost in noise in the southeast events.

4.3.9   Cottonwood Line

The Cottonwood line runs east-west, splaying to the east from the Sepultura line

(Figure 23). The western edge of the line features a small dipping arrival between 1.1 and

1.7 s from 0 to 0.7 km along the profile (Figure 40 – pink). This arrival dips up to 1.2 s at

1.3 km, stays flat at 1.6 s from 1.3 to 4.2 km along the profile, and then dips back up to

~1 s at the east end of the profile (Figure 40 – yellow). The flat, 2.7 s arrival from

previous lines makes an appearance in this line, dipping from 2.1 s at 0.5 km down to a

low of 3 s at 3 km along the profile, and then rising back up to 2.1 s at 4 km (Figure 40 –

red).

4.3.9.1   Frequency analysis

In the northwestern events, the consistent, flat, high-amplitude signal that crosses

the entire profile at ~4 s has less noise on 0.5 – 1.0 Hz than the other frequency band bins

(Figure 41A-C). Additionally, there is high amplitude noise from 0 to 1 km along profile

that extends to ~3 s.

There is a consistent, flat, high amplitude arrival at 2 s across the whole

southeastern events profile, which gets increasingly lost in noise as frequency bins

increase (Figure 41D-F). From the northwest, there is a flat, high amplitude arrival across the profile at 4 s. From the southeast, this arrives at 2 s.

4.3.10 Montosa Line

The Montosa line runs north to south in the Los Piños Mountains (Figure 23). Starting at ~2.5 km along the profile, an arrival at ~1 s remains generally flat (+/- 0.1 s) across the entire profile except at ~7 km (Figure 42 – yellow). Here, a small south-dipping arrival dips into the ~1 s arrival. Two more arrivals at 1.8 s (Figure 42 – pink) and 2.7 s (Figure 42 – red) continue flat and undisturbed across the entirety of the Montosa line. Below 2.7 s, arrivals are low amplitude and uniform.

4.3.10.1 Frequency analysis

Shallow arrivals across the whole northwestern event profile become high amplitude and more continuous with increasing frequencies (Figure 43A-C). At lower frequencies, the north and south ends of the profile appear to host north- and south-dipping arrivals respectively, but only at 1.0 to 1.5 Hz do the dipping arrivals become distinct and continuous (Figure 43C).

Arrivals in the southeastern events that appear noisy at lower frequencies become less noisy and higher amplitude with increasing frequency bands (Figure 43 D-F). The north and south ends of the northwest profiles feature outward-dipping (north- and south-dipping respectively), whereas the southeast is completely flat across all frequencies.

5 Discussion

5.1 Geologic interpretation

5.1.1 *Northwestern Quadrant*

The most striking feature in the ATT and Popotosa lines is the steeply east-dipping series of high amplitude arrivals. Synthetic tests indicate that this phase is a Rayleigh wave converted from the teleseismic P (P-to-Rg) at the Loma Pelada fault. This P-to-Rg phase is most commonly observed near abrupt, sharp changes in local topography (i.e. Bannister et al. 1990), but the topography nearest the apparent surface conversion features no such changes in topography, as can be seen in the topography plotted on top of figures 8 and 10. Additionally, the Rayleigh wave physically begins on both the ATT and the Popotosa lines at the P-wave arrival, coincident with the Loma Pelada fault, which could have a strong velocity contrast at shallow depths (Figure 8, 10 – green).

Synthetic seismogram modeling displays a large, high amplitude, dipping arrival (Figure 6), as does a broadband station on the Popotosa line (Figure 1, 10). In both cases, I plotted the vertical component traces against the radial component traces in the area of the initial P-wave arrival and in the area of the large dipping arrival (Figures 44, 45). Both show elliptical particle motion in the area of the arrival vs a solely vertical particle motion around the direct P-wave arrival. The P-to-Rg shows up again after 10 seconds in the Jack Well line, appearing to "dip" north (Figure 12 – green). This arrival pattern arises from the acquisition geometry that places the southern portion of the line closest to the Loma Pelada fault, while the line and fault move away from one another going northward, creating a longer path for the Rayleigh wave to travel in the north.

All three lines in the northwestern quadrant contain a strong reflector at ~2 to 3 s. This reflector likely marks the bottom of the basin, possibly a down-dropped graben (Figure 8, 10, 12 – red). A series of domino-style grabens are thought to dominate the basin bottom as extension has opened the rift (Love and Chamberlin, 2016). In the Jack Well Line, which runs north-south, the basin bottom appears to shallow southwards (Figure 12 – red). This observation is consistent with recent gravity work that shows the Albuquerque basin shallowing southward as the basin constricts into the Socorro basin (Grauch and Connell, 2013). An east-dipping reflector is visible only in the events arriving from the northwest in both the Popotosa and ATT lines (Figure 9, 11 A-C). This reflector is likely the Loma Pelada fault, which has enough offset to create the modern edge of the Albuquerque basin in this area (Love and Chamberlin, 2016; Ricketts et al., 2015).

The Jack Well line is the only line in this quadrant entirely within the Albuquerque basin. The northern half of the line lies on top of alluvium and the southern half of the line winds into Upper Santa Fe Group, which is slightly older and more consolidated than the alluvium (Machette, 1978; Connell and McCraw, 2007). The change in the shallow reflection character could be attributed to this transition in surface geology, which likely extends to shallow depths.

5.1.2   *Southwestern Quadrant*

The southwest quadrant covers the margins of two basins: the La Jencia basin to the west and the Socorro basin to the east. One of the major phases in this quadrant is once again the P-to-Rg conversion across the eastern-most lines. In the Alamillo line, the Rayleigh waves are just being converted at the Loma Pelada fault, so only the

easternmost portion of the line captures the moveout (Figure 17 – green). Both the Powerline and Esquival lines are physically within the basin, and the surface waves are captured as they move eastward (Figure 19, 21 – green). The Powerline line is closer to the Loma Pelada fault in the south and these arrivals appear earlier in the southern part of the line. The Esquival line trends northwest-southeast oblique to the fault. At one section, around ~1 km, the line runs perpendicular to the corresponding lateral strike of the fault creating a steeper apparent dip for the surface wave arrivals. Then, between 1.5 and 2 km, the line runs sub-parallel to the lateral strike and the surface wave arrival is flat, before continuing obliquely to the southeast.

The Alamillo line is unique to this study in that there are two very recent studies that were done on the same road on which the line was deployed. Chamberlin and Love (2016) published a cross section and a series of block diagrams displaying the depositional history of this section of the SNWR. Even more recently, Folsom (2017) performed a magnetotelluric study and was able to compare his results to Chamberlin and Love's cross section. Both studies show the edge of the Socorro basin beginning at the Loma Pelada fault, which agrees well with our study; P-to-Rg conversions at the Loma Pelada fault could be attributed to a basin-edge high impedance contrast. Folsom's (2017) model shows higher resistivity in the Cerritos de las Minas and lower resistivity in the La Jencia and Socorro basins. Again, this observation agrees well with the TVR profile: a change in the character of the shallowest arrivals (< 1 s) can be seen moving from west to east with a dip up and down that line up well with the Cerritos de las Minas (Figure 17).

The West Mesa Line is relatively uniform across the transect (Figure 15). The northern few kilometers of the array sit over upper Pleistocene to Holocene alluvial

deposits, before moving into the Upper Santa Fe group basin deposits (Cather and Read, 2003). The small, shallow arrivals that change character after 2.5 km along the profile could be attributed to this minor change in shallow geology (Figure 15 – yellow). There is no significant reflector indicative of a basement sediment contact, most likely due to a smoother density contrast between basin fill and basement rocks.

The Powerline line runs through the Socorro basin, with a northern terminus at the Rio Salado. Moving southward, the line sits atop active and stabilized Holocene eolian deposits (sand), then Pliocene stream deposits and Pliocene piedmont deposits of decreasing thickness. Miocene Popotosa formation dips northward beneath these deposits (Machette, 1978). The shallow, gently dipping reflectors in this line (Figure 19 – yellow) could be attributed to this erosion of the Popotosa formation, or possibly an underlying andesite, which is exhumed on the other side of the Loma Pelada fault in the Cerritos de las Minas. The depth to basement in this area is unknown, but is estimated to be ~3 – 4 kilometers (Chamberlin and Love, 2016), so some of the flatter reflectors at ~2 s could be basement rock.

The Esquival line sits almost exclusively in or on the margins of the Rio Salado. Because of this geometry, much of the surface and likely much of the shallow subsurface is dominated by stream deposits. On the southeastern edge of the line, two reflectors appear to be dipping west (Figure 21 – red, pink). These arrivals may be related to the Joyita hills uplift approximately 2 km to the east of the southeastern end of the Esquival line. A range of formations from Precambrian to Neogene are exhumed in the Joyita hills, with beds tilting towards the Esquival line, covered by alluvium (de Moor et al. 2005).

5.1.3   Eastern Half

        The eastern half of the Sevilleta Array in general is structurally complex and the

Firebreak line is no exception. However, little of that complexity is captured in this

profile. The Firebreak line draws fairly close to Black Butte, a surface exposure of

Oligocene basaltic andesite and rhyolitic tuffs surrounded on all sides by very young (<

1 Ma) alluvium (Rinehart et al., 2014). Black Butte sits near the break in the line at ~1

km along the profile. Here, shallow arrivals at 1.2 s dip to the east (Figure 24 – yellow).

These reflectors could be the contact between the Quaternary alluvium around Black

Butte and the basaltic andesite, which is known to continue as a layer in this region

(Richard Chamberlin, personal communication). The highest amplitude arrivals are seen

at 2.7 s in the middle of the profile and could delineate the basement contact at ~3.3 km

deep (Figure 24 – red). The west dipping arrivals on the eastern end of the profile likely

mark the Los Piños fault, which separates the Albuquerque basin alluvium from

Proterozoic igneous and metamorphic rocks in the Los Piños Mountains (Luther et al.,

2005). Comparing azimuthal differences, this arrival is only seen from the southeast

direction, which supports this fault being somewhat steep. Faults on the edge of the basin

are not mapped due to coverage by alluvium, but a significant fault could be truncating

the arrivals. The arrivals themselves look similar to the P-to-Rg arrivals observed in the

western half of the array but have slightly smaller amplitudes (Figure 24 – green).

Alternatively, these deeper, west-dipping arrivals could be a deeper zone of deformation

suggested when the same reflectors were seen in the COCORP profile (Brown et al.,

1979).

The McKensie North line lies almost exclusively on the Los Piños' alluvial fan. Like the Firebreak line, the McKensie North line strays fairly close to Black Butte, but noise in the northwestern portion of the line makes observations difficult. Like the Firebreak line, a flat arrival at ~2.7 s is nearly consistent across the line. However, around 3 km, the arrival appears to 'break' and dip northwest (Figure 26 – red, orange). An unnamed fault is mapped with an approximate location at the surface here, so the dipping arrivals could be offset from this fault (Rinehart et al., 2014). The Albuquerque basin is known to have some buried Laramide structures (Kelley, 1977; Brown et al., 1979), which may also be a reasonable explanation here.

The McKensie South line skirts around the edge of the Joyita Hills uplift before running towards the Los Piños Mountains. Unlike the two northern west-east lines, the McKensie South line does not run completely up to the base of the mountains. The northwest-dipping arrivals on the southeast end of the line could be remnant surface waves from the edge of the Los Piños fault. Like most of the other lines in the eastern half, the McKensie South line contains flat-lying arrivals at ~2.7 s (Figure 28 – red). These arrivals are relatively low amplitude compared to other lines. Due to uplift from the Joyita hills, the shallower arrivals at 1.5 s (~1.8 km)(Figure 28 – pink) might be a more realistic representation of basement contact in this area.

The Red Well line runs straight through the eastern portion of the Joyita Hills uplift, an area of uplifted Permian rocks. West of the Red Well line is the East Joyita Fault, which exhumes Precambrian basement rock, and juxtaposes this basement against folded and faulted overlying Pennsylvanian through Quaternary rocks (de Moor et al., 2005). Considering the east-dipping arrivals (Figure 30 – pink) are sharp, higher

frequency, and not ringing, they could be reflecting off of the East Joyita fault. For the shallow, flat lying arrivals (Figure 30 – yellow), most of the surface rocks here are not alluvium but actually Permian limestone and sandstones with a higher elevation basement (de Moor et al., 2005), so the basement contact may be arriving significantly earlier (1.2 s [1.5 km] instead of 2.7 s [3.3 km]) than on the other profiles.

The Palo Duro line goes through several different areas covered by other lines in this array. The Palo Duro line travels just east of Black Butte and runs nearly parallel to the Military Road fault, which is thought to possibly have buried splays in the area (David Love, personal communication). The north-dipping and south-dipping arrivals from the first 2 km could be associated with Black Butte, as the butte is surrounded by Quaternary alluvium (Figure 32 – blue, yellow). The dipping arrival at ~4 km along profile (Figure 32 – pink) could be either an unmapped fault, or a splay of the Military Road fault, as the Military Road fault turns towards the line at this point before running more parallel again. Moving down the line, the small uptick in arrivals around 12 km (Figure 32 – pink) coincides with the eastern edge of the Joyita Hills uplift, an area of uplifted Pennsylvanian rocks. The shallow arrivals in the southernmost section of the Palo Duro line are very similar to COCORP line 2A (Brown et al., 1979). The line enters the Valle del Ojo de la Parida, which is a valley formed by a syncline between the Joyita Hills uplift and the adjacent uplift.

The Gibbs line skirts the western edge of the Valle del Ojo de la Parida and the Valle de La Joya, putting the north-south portion of the line against the La Joya Uplift. From there, the line moves directly east, crossing the Valle de la Joya before meeting the Palo Duro line. The south-north portion of the line is relatively uniform outside of the

first km, where the southern tip of the line approaches an uplifted region of Eocene and Upper Cretaceous rocks at the southwestern edge of the Valle del Ojo de la Parida (Cather et al., 2004). When the line strikes east-west, the arrival at 1.5 s dips to the east, likely equivalent to the arrival on the McKensie South and the Red Well lines (Figure 34 – pink). This arrival appears to be the East Joyita fault from the Joyita Hills uplift beneath the valley's alluvium. The shallow dip and rise between 7 and 10 km along the profile that follows the trend of the previous arrival (Figure 34 – yellow) could be the large syncline thought to rest under the Valle de la Joya and Valle del Ojo de la Parida (Darton, 1921).

The Tomasino line goes through southern extent of the Valle del Ojo de la Parida before moving east into the base of the southern extent of the Los Piños uplift. The western part of the line crosses a thin layer of Quaternary alluvium over uplifted Permian rocks, then traverses heavily folded and faulted Permian rocks (Cather et al., 2004; Cather and Colpitts, 2012). The series of dipping arrivals seen in the first 2 km of the line could be a reflection of the southern tip of the valley (Figure 36 – pink). The noisy remainder of the section is likely evidence of how chaotic sequences are in the subsurface. Also, the basement depth could be as shallow as 600 m in parts of the Tomasino line (Cather et al., 2004).

The Sepultura line runs east of the nearly parallel Palo Duro line. The proximity of the Los Piños fault most likely gives rise to what looks like more P-to-Rg surface waves in the northern half of the line (Figure 38 – green). The fact that the Rg waves appear later shows the proximity of the line to the Los Piños fault; the line is further from the fault in the northernmost portion of the line. These high amplitude arrivals appear in

40

increasingly long series in the frequency bins, and are present across all frequencies, Rg waves in other lines (Figure 39). Moving south, the surface waves disappear, likely from the lack of basin fill moving into the southern extent of the Los Piños Mountains which creates a smaller impedance contrast. The north dipping arrivals at 16 and 17 km coincide with the line crossing into the region of uplifted Pennsylvanian and Permian rocks between the Los Piños and Joyita Hills uplifts (Cather and Colpitts, 2012)(Figure 38 – yellow, blue). The uplifted regions are heavily faulted and folded, so the dipping arrivals could be an expression of either.

The Cottonwood line enters the base of the Los Piños uplift, approaching but not crossing the Los Piños fault. Everything in the upper 4 seconds seems to be dipping into the center of the line, which is where the line crosses a very small tract of alluvium (Figure 40). Considering the rest of the line crosses exposed Pennsylvanian rocks (Allen et al., 2013), the alluvium could be slowing the velocities down enough to create the gentle dip. There is also an exposed fault surface, but the fault is thought to be dipping west (Allen et al., 2013). For the eastern edge of the line, the Los Piños fault is nearby (~2.5 km southeast) and approaching at an oblique angle which could be partially affecting the arrivals.

The Montosa line is the only line that is exclusively outside of the basin. The line runs on top of and parallel to the strike of both the Manzano/Los Piños synclinorium, composed of metamorphic rocks, and two fault systems: the Montosa fault and the Paloma fault (Luther et al., 2005; Allen et al., 2014). The two lower arrivals at 1.8 and 2.7 s are likely different contacts between the folded rocks in the synclinorium (Figure 42 – pink, red). The arrivals at ~1 s begin at the point at which the line enters the partially

eroded limestone that caps the synclinorium (Allen et al., 2014)(Figure 42 – yellow). The line crosses the Montosa fault several times (from 0 to 1 km and at 6.7 km), so the slight dip at ~7 km along the profile could be some offset Pennsylvanian limestone across the fault.

5.2 P-to-Rg in the Sevilleta Array

The high-amplitude dipping arrivals seen on the ATT and Popotosa lines (Figures 8 and 10) are surface waves formed by P-wave to Rg-wave conversion at the western edge of the Albuquerque and Socorro basins. I verified that these arrivals are Rayleigh waves in two ways: I extracted three-component data from concurrent broadband stations (Figure 45) and I compared the Sevilleta array data to forward models of a simple basin in similar media (Figure 6). In both cases, I plotted particle motion of the vertical component against the radial component during both the initial P-wave arrival and times when the high-amplitude arrivals occurred (Figures 44, 45). Linear particle motion is exhibited by the P-wave arrival but the high-amplitude arrivals exhibited elliptical particle motion.

P-to-Rg conversions can occur when there is rough topography, shallow velocity heterogeneity, or a shallow low velocity zone (Revenaugh and Mendoza, 1996). Rough topography is thought to be one of the most controlling factors in P-to-Rg conversions, and modeling of P-to-Rg from topography has been well documented (e.g. Ruud et al., 1993; Hestholm et al., 1994; Clouser and Langston, 1995; Monteiller et al., 2013). In this context, rough topography consists of elevation changes of more than half the Rayleigh wavelength, which, in previous studies, could be up to 300 km away from the actual array (Bannister et al., 1990). However, several lines in the Sevilleta array that display the

initial Rg-conversion do not exhibit dramatic elevation changes. The largest change is ~150 m over 6 km in the ATT line. The synthetic seismograms feature very prominent Rg phases but with a flat free-surface topography, as well. I conclude that, in the Sevilleta array, topography is not a likely cause of the P-to-Rg conversion.

The apparent P-to-Rg conversion observed in the western half of the array correlates with the surface expression of the Loma Pelada fault, suggesting that the conversion is caused by high impedance contrast across the fault. Sedimentary basins have been shown to have enough impedance contrast at basin edges to induce P-to-Rg conversions (Levander and Hill, 1985; Vidale and Hemberger, 1988; Revenaugh and Mendoza, 1996). To confirm that the Loma Pelada fault is the source, I calculated the correlation between the time of the P-to-Rg arrival against the distance of the receiver from the Loma Pelada fault, which yielded a positive linear correlation with an R^2 of 0.987. Though the authors do not explicitly discuss P-to-Rg conversion, a similar arrival can be seen in a previous TVR study across the Bighorn basin in northern Wyoming (Figure 46) (Yang et al., 2012). However, not every basin appears to give such a strong arrival: visual inspection of the TVR study in the Three Gorges in China (Zou et al., 2014) does not appear to contain any P-to-Rg phases.

5.3   Comparison with COCORP

Creating TVR profiles is advantageous because the results should be comparable with active source methods but without the logistical and financial costs typically associated with active source experiments. The COCORP survey extended to 35 km

depth, and successfully imaged the SMB, but found little evidence of the reflection Moho in the region (Brown et al., 1979). COCORP line 2A was taken on the same road as the Palo Duro line and COCORP line 1A was taken on US-60, which runs sub-parallel to the Firebreak line, between 1.3 and 2.3 km north (Figure 47, 48). My comparisons between the two surveys are based solely on the published works on the Rio Grande rift COCORP survey. Due to lack of high quality reflection images, I rely more heavily on what is written and the annotated survey profiles than the actual seismic profiles provided in the papers.

Similarities between the two surveys are most prominent between 1 and 5 s. However, both studies were unable to detect a definitive Moho reflection. Across much of the Sevilleta array, I note a relatively flat-lying arrival at 2.5 – 2.7 s. Across the western lines of COCORP survey, Brown et al. (1979) also noted an inconsistent 2.7 s reflector, interpreting the reflector as a Cenozoic volcanic unit or a Paleozoic sedimentary reflection.

COCORP line 1 and the Sevilleta array Firebreak line share west-dipping arrivals on the east end of the line (Figure 48). Brown et al. (1979) noted some of the reflectors and hypothesized that the reflectors are buried metamorphic terrain. However, de Voogd et al. (1986), after a more extensive re-evaluation of the line, considered the reflectors to be the southeastern Albuquerque basin master fault. I find that the analysis by de Voogd et al. (1986) is more consistent with the Sevilleta array, as the geometry of the reflectors assessed by these workers better matched those interpreted by me. Brown et al. (1979) recognized less reflectors than de Voogd et al. (1986) and gave less of an explanation,

making comparisons on this line between COCORP and the Sevilleta array more difficult.

The Sevilleta array Palo Duro line shares some reflectors with COCORP line 2A (Figure 47). Jurdy and Brocher (1980) evaluated shallow velocities along line 2A, finding higher shallow velocities in the middle of the line. This was disputed by Brocher (1981), who found that velocities in the middle of the line were not as high as suggested by Jurdy and Brocher (1980). This area correlates with the Joyita Hills uplift, which includes exhumed, relatively high velocity Permian sandstones and limestones (Brocher, 1981; Allen et al., 2013). Both lines feature a distinct valley-like dip and rise in shallow reflectors at the south end of the line (Figure 47). Interpretation of this feature is left unaddressed by Brown et al. (1979), with Brocher (1981) stating that there is either a very thin or no Paleozoic layer in this area. I believe this area corresponds well with the Valle de la Joya and the Valle del Ojo de la Parida, which are the northern and southern section, respectively, of the valley between the Joyita Hills and Los Piños uplifts. A major difference between interpretations of COCORP line 2A and my interpretation of the Palo Duro line is the central region of the line between 1 and 4 s. Brown et al. (1979) reported that the area was transparent, alleging that area could be hosting an unmapped pluton, not dissimilar to the Los Piños pluton. The Sevilleta Array has reflections in the region mentioned and might represent a more elevated basement depth than an intruded pluton.

Due to the frequency content of teleseismic events, I am unable to resolve some of the features interpreted by Brown et al. (1979), de Voogd et al. (1986), and Brocher (1981). The COCORP study used a Vibroseis vibrator and the Sevilleta array utilized

teleseismic earthquakes. These different methods lead to very different frequency contents: this study's frequency range is 0.2 to 1.5 Hz, whereas COCORP's was 10 to 32 Hz (de Voogd et al., 1986). If I make the modest assumption of a mid-crustal P-wave velocity of 6000 m/s, and a maximum frequency of 1.5 Hz, I am left with a wavelength of 1500 m resulting in a minimum vertical resolution of 375 m. The COCORP study found high amplitude reflectors at ~6 s that Brown et al. (1979) interpreted as an inconsistent magma body, agreeing well with previous workers' interpretation of the SMB. At 150 m of partial melt, the magma body is unable to be resolved by this study.

6 Conclusion

Teleseismic earthquakes recorded by the Sevilleta array have successfully been used to passively image subsurface geologic structures both mapped and unmapped in the southern Albuquerque and northern Socorro basins. I created TVR profiles using five teleseismic earthquakes between M5.1 and M6.7 from South America, Japan, and Kamchatka. Observations of the lines in the array correlate well with known geologic structures in the study area. P-to-Rg converted phases dominate much of the western half of the array due to the basin-bounding Loma Pelada normal fault, which creates a large impedance contrast as the fault offsets Quaternary alluvium deposits on the east from Tertiary rocks on the west. Faults in the eastern half of the array form a complex uplift zone, the Joyita Hills uplift, seen across multiple lines. Mapped geology along the eastern margin of the southern Albuquerque basin agrees well with the profiles in this study. Some structures apparent from my profiles are not mapped and are most likely buried by recent syn-rift fill. However, the interpreted buried structures are consistent with known regional extensional and deformational trends. The TVR profiles were compared to a

published active source survey, the COCORP Rio Grande Rift experiment, which shares some lines with the Sevilleta array. Differences between the two surveys were primarily due to differences in frequency content, but major structures were consistent across the profiles. Overall, while I was unable to resolve the shallowest (< 0.7 s) and deepest (> 5 s) known structures in the region, I was able to use the TVR method to illuminate major basin structures in a complex area.

7   References

Ake, J.P., and Sanford, A.R., 1988, New evidence for the existence and internal structure of a thin layer of magma at mid-crustal depths near Socorro, New Mexico: Bulletin of the Seismological Society of America, v. 78, p. 1335–1359.

Allen, B.D., Love, D.W., McCraw, D.J., and Rinehart, A.J., 2013, Geologic map of the Becker SW quadrangle, Socorro County, New Mexico: New Mexico Bureau of Geology and Mineral Resources, scale 1:24000.

Allen, B.D., Timmons, M., Luther, A.L., Miller, P.L., and Love, D.W., 2014, Geologic Map of the Cerro Montoso 7.5-Minute Quadrangle, Socorro County, New Mexico: New Mexico Bureau of Geology and Mineral Resources, scale 1:24000.

Balch, R.S., Hartse, H.E., Sanford, A.R., and Lin, K., 1997, A New Map of the Geographic Extent of the Socorro Mid-Crustal Magma Body: Bulletin of the Seismological Society of America, v. 87, p. 174–182.

Baldridge, W.S., Keller, G.R., Haak, V., Wendlandt, E., Jiracek, G.R., and Olsen, K.H., 1995, The Rio Grande Rift, in Olsen, K.H. ed., Continental Rifts: Evolution, Structure, Tectonics, Amsterdam, Elsevier Science B.V., Developments in Geotectonics 25, p. 233–275.

Baldridge, W.S., Olsen, K.H., and Callender, J.F., 1984, Rio Grande rift: Problems and Perspectives: New Mexico Geological Society Guidebook, v. 35, p. 14.

Bannister, S.C., Husebye, E.S., and Ruud, B.O., 1990, Teleseismic P Coda Analyzed by Three-Component and Array Techqniques: Deterministic Location of Topograhic P-to-Rg Scattering near the NORESS array: Bulletin of the Seismological Society of America, v. 80, p. 1969–1986.

Beck, W.C., and Chapin, C.E., 1994, Structural and tectonic evolution of the Joyita Hills, central New Mexico: Implications of basement control on Rio Grande rift, in Keller, G.R., and Cather, S.M., eds., Basins of the Rio Grande Rift: Structure, Stratigraphy, and Tectonic Setting: Geological Society of America Special Paper 291, p. 187–205.

Brocher, T.M., 1981, Shallow velocity structure of the Rio Grande Rift north of Socorro, New Mexico: A reinterpretation: Journal of Geophysical Research: Solid Earth, v. 86, p. 4960–4970, doi: 10.1029/JB086iB06p04960.

Brocher, T.M., 2005, Empirical Relations between Elastic Wavespeeds and Density in the Earth's Crust: Bulletin of the Seismological Society of America, v. 96, n. 6, p. 2081-2092.

Brown, L.D., Krumhansl, P.A., Chapin, C.E., Sanford, A.R., Cook, F.A., Kaufman, S., Oliver, J.E., and Schilt, F.S., 1979, Cocorp Seismic Reflection Studies of the Rio Grande Rift, in Riecker, R.E. ed., Special Publications, Washington, D. C., American Geophysical Union, p. 169–184, doi: 10.1029/SP014p0169.

Cather, S.J., and Colpitts, Jr., R.M., 2012, Geologic map of the Sierra de la Cruz quadrangle, Socorro County, New Mexico.: New Mexico Bureau of Geology and Mineral Resources, scale 1:24000.

Cather, S.J., Colpitts, Jr., R.M., and Hook, S.C., 2004, Geologic map of the Mesa del Yeso quadrangle, Socorro County, New Mexico.: New Mexico Bureau of Geology and Mineral Resources, scale 1:24000.

Cather, S.J., and Jr, R.C., 2012, Geologic map of the Sierra De La Cruz quadrangle, Socorro County, New Mexico: New Mexico Bureau of Geology and Mineral Resources, scale 1:24000.

Cather, S.J., and Read, A., 2003, Geologic map of the Silver Creek 7.5-minute Quadrangle: New Mexico Bureau of Geology and Mineral Resources, scale 1:24000.

Chamberlin, R.M., 1983, Cenozoic domino-style crustal extension in the Lemitar Mountains, New Mexico: a summary: New Mexico Geological Society Guidebook, v. 34, p. 9.

Chamberlin, R.M., and Love, D.W., 2016, Block diagrams and cross sections illustrating geologic and tectonic evolution of the Sevilleta National Wildlife Refuge, Rio Grande Rift, Central New Mexico: New Mexico Bureau of Geology and Mineral Resources Open-file 579, 17 p.

Chapin, C.E., 1979, Evolution of the Rio Grande rift - a summary, in Rio Grande Rift: Tectonics and Magmatism, Washington, D.C., American Geophysical Union, p. 1–5.

Clayton, R.W., and Wiggins, R.A., 1976, Source shape estimation and deconvolution of teleseismic bodywaves: Geophysical Journal International, v. 47, p. 151–177, doi: 10.1111/j.1365-246X.1976.tb01267.x.

Clouser, R.H., and Langston, C.A., 1995, Effect of sinusoidal interfaces on teleseismic P-wave receiver functions: Geophysical Journal International, v. 123, p. 541–558, doi: 10.1111/j.1365-246X.1995.tb06870.x.

Connell, S.D., and McCraw, D.J., 2007, Preliminary geologic map of the La Joya NW quadrangle, Socorro County, New Mexico.: New Mexico Bureau of Geology and Mineral Resources, scale 1:24000.

Darton, N.H., 1921, Contributions to Economic Geology, Part II, in Geologic Structure of Parts of New Mexico, p. 173–276.

Duru, K., Kreiss, G., and Mattsson, K., 2014, Stable and High-Order Accurate Boundary Treatments for the Elastic Wave Equation on Second-Order Form: SIAM Journal on Scientific Computing, v. 36, p. A2787–A2818, doi: 10.1137/130947210.

Fialko, Y., and Simons, M., 2001, Evidence for on-going inflation of the Socorro Magma Body, New Mexico, from interferometric synthetic aperture radar imaging: Geophysical Research Letters, v. 28, p. 3549–3552, doi: 10.1029/2001GL013318.

Finnegan, N.J., and Pritchard, M.E., 2009, Magnitude and duration of surface uplift above the Socorro magma body: Geology, v. 37, p. 231–234, doi: 10.1130/G25132A.1.

Gao, W., Grand, S.P., Baldridge, W.S., Wilson, D., West, M., Ni, J.F., and Aster, R.C., 2004, Upper mantle convection beneath the central Rio Grande rift imaged by P and S wave tomography: Journal of Geophysical Research, v. 109, doi: 10.1029/2003JB002743.

Grauch, V.J.S., and Connell, S.D., 2013, New perspectives on the geometry of the Albuquerque Basin, Rio Grande rift, New Mexico: Insights from geophysical models of rift-fill thickness, in Geological Society of America Special Papers, Geological Society of America, v. 494, p. 427–462, doi: 10.1130/2013.2494(16).

Hansen, S.M., and Schmandt, B., 2017, P and S Wave Receiver Function Imaging of Subduction With Scattering Kernels: Geochemistry, Geophysics, Geosystems, v. 18, p. 4487–4502, doi: 10.1002/2017GC007120.

Hestholm, S.O., Husebye, E.S., and Ruud, B.O., 1994, Seismic wave propagation in complex crust-upper mantle media using 2-D finite-difference synthetics: Geophysical Journal International, v. 118, p. 643–670, doi: 10.1111/j.1365-246X.1994.tb03991.x.

Hudson, M.R., and Grauch, V.J.S., 2013, Introduction, in Geological Society of America Special Papers, Geological Society of America, v. 494, p. v–xii, doi: 10.1130/2013.2494(00).

Jurdy, D.M., and Brocher, T.M., 1980, Shallow velocity model of the Rio Grande rift near Socorro, New Mexico: Geology, v. 8, p. 185, doi: 10.1130/0091-7613(1980)8<185:SVMOTR>2.0.CO;2.

Kelley, V.C., 1977, Geology of Albuquerque Basin, New Mexico: New Mexico Bureau of Geology and Mineral Resources, Memoir 33.

Kelley, S., and CHAMBERLIN, R.M., 2012, Our growing understanding of the Rio Grande Rift: New Mexico Earth Matters, v. 12, p. 6.

Levander, A.R., and Hill, N.R., 1985, P-SV Resonances in Irregular Low-Velocity Surface Layers: Bulletin of the Seismological Society of America, v. 75, p. 847–864.

Luther, A.L., Karlstrom, K.E., Scott, L.A., Elrick, M., and Connell, S.D., 2005, Geologic map of the Becker 7.5 - minute quadrangle, Valencia and Socorro Counties, New Mexico.: New Mexico Bureau of Geology and Mineral Resources, scale 1:24000.

Machette, M., 1978, Geologic Map of the San Acacia Quadrangle, Socorro County, New Mexico: USGS.

Matthew, F., 2017, Deep resistivity imaging of the Central Rio Grande Rift using 3-D inverse models of magnetotelluric data, with implications for hydrologic and geothermal processes [Master of Science]: New Mexico Institute of Mining and Technology, 75 p.

Monteiller, V., Chevrot, S., Komatitsch, D., and Fuji, N., 2013, A hybrid method to compute short-period synthetic seismograms of teleseismic body waves in a 3-D regional model: Geophysical Journal International, v. 192, p. 230–247, doi: 10.1093/gji/ggs006.

de Moor, M., Zinsser, A., Karlstrom, K.E., CHAMBERLIN, R.M., Connell, S.D., and Read, A., 2005, Geologic Map of the La Joya 7.5 - minute Quadrangle: New Mexico Bureau of Geology and Mineral Resources, scale 1:24000.

Pearse, J., and Fialko, Y., 2010, Mechanics of active magmatic intraplating in the Rio Grande Rift near Socorro, New Mexico: Journal of Geophysical Research, v. 115, doi: 10.1029/2009JB006592.

Ranasinghe, N.R., Worthington, L.L., Schmandt, B., Jiang, C.X., Finlay, T.S., Bilek, S.L., Aster, R.C., Submitted, Upper crustal shear wave velocity structure of the South-central Rio Grande Rift from large-N Sevilleta seismic array: Submitted to Seismological Research Letters.

Revenaugh, J., and Mendoza, H., 1996, Mapping Shallow Heterogeneity with Teleseismic P to Rg Scattered Waves: Bulletin of the Seismological Society of America, v. 86, p. 1194–1199.

Ricketts, J.W., Karlstrom, K.E., and Kelley, S.A., 2015, Embryonic core complexes in narrow continental rifts: The importance of low-angle normal faults in the Rio Grande rift of central New Mexico: Geosphere, v. 11, p. 425–444, doi: 10.1130/GES01109.1.

Rinehart, A.J., Love, D.W., and Miller, P.L., 2014, Geologic Map of the Black Butte 7.5-Minute quadrangle, Socorro and Valencia Counties, New Mexico.: New Mexico Bureau of Geology and Mineral Resources, scale 1:24000.

Rinehart, E.J., Sanford, A.R., and Ward, R.M., 1979, Geographic extent and shape of an extensive magma body at mid-crustal depths in the Rio Grande Rift near Socorro, New Mexico, in Rieker, R.E. ed., Rio Grande Rift: Tectonics and Magmatism, Washington, D.C., American Geophysical Union, p. 237–251

Russell, L.R., and Snelson, S., 1994a, Structure and tectonics of the Albuquerque Basin segment of the Rio Grande rift: Insights from reflection seismic data, in Keller, G.R., and Cather, S.M., eds., Basins of the Rio Grande Rift: Structure, Stratigraphy, and Tectonic Setting: Geological Society of America Special Paper 291, p. 83–112.

Ruud, B.O., Husebye, E.S., and Hestholm, S.O., 1993, Rg observations from four continents: inverse- and forward-modelling experiments: Geophysical Journal International, v. 114, p. 465–472, doi: 10.1111/j.1365-246X.1993.tb06980.x.

Sanford, A.R., Mott, Jr., R.P., Shuleski, P.J., Rinehart, E.J., Caravella, F.J., Ward, R.M., and Wallace, T.C., 1977, Geophysical evidence for a magma body in the crust in the vicinity of Socorro, New Mexico, in Heacock, J.G. ed., The Earth's Crust: Its Nature and Physical Properties, Washington, D.C., American Geophysical Union, Geophysical Monograph 20, p. 385–404.

Schlue, J.W., Aster, R.C., and Meyer, R.P., 1996, A lower crustal extension to a midcrustal magma body in the Rio Grande Rift, New Mexico: Journal of Geophysical Research: Solid Earth, v. 101, p. 25283–25291, doi: 10.1029/96JB02464.

Schmandt, B., and Clayton, R.W., 2013, Analysis of teleseismic P waves with a 5200-station array in Long Beach, California: Evidence for an abrupt boundary to Inner Borderland rifting: Journal of Geophysical Research: Solid Earth, v. 118, p. 5320–5338, doi: 10.1002/jgrb.50370.

Sheetz, K.E., and Schlue, J.W., 1992, Inferences for the Socorro magma body from teleseismic receiver functions: Geophysical Research Letters, v. 19, p. 1867–1870, doi: 10.1029/92GL02137.

Stähler, S.C., Sigloch, K., and Nissen-Meyer, T., 2012, Triplicated P-wave measurements for waveform tomography of the mantle transition zone: Solid Earth, v. 3, p. 339–354, doi: 10.5194/se-3-339-2012.

Stein, S., and Wysession, M., 2003, An introduction to seismology, earthquakes, and earth structure: Malden, Massachusetts, Wiley-Blackwell, 498 p.

Tseng, T.-L., 2006, Probing the Southern Indian Shield with P-Wave Receiver-Function Profiles: Bulletin of the Seismological Society of America, v. 96, p. 328–333, doi: 10.1785/0120050074.

Tseng, T.-L., Chen, W.-P., and Nowack, R.L., 2009, Northward thinning of Tibetan crust revealed by virtual seismic profiles: Geophysical Research Letters, v. 36, doi: 10.1029/2009GL040457.

Vidale, J.E., and Helmberger, D.V., 1988, Elastic finite-difference modeling of the 1971 San Fernando, California Earthquake: Bulletin of the Seismological Society of America, v. 78, p. 122–141.

de Voogd, B., Brown, L.D., and Merey, C., 1986, Nature of the eastern boundary of the Rio Grande rift from COCORP surveys in the Albuquerque basin, New Mexico: Journal of Geophysical Research, v. 91, p. 6305, doi: 10.1029/JB091iB06p06305.

Wilson, D., 2005, Imaging the seismic structure of the crust and upper mantle beneath the Great Plains, Rio Grande Rift, and Colorado Plateau using receiver functions: Journal of Geophysical Research, v. 110, doi: 10.1029/2004JB003492.

Yang, Z., Sheehan, A.F., Yeck, W.L., Miller, K.C., Erslev, E.A., Worthington, L.L., and Harder, S.H., 2012, Imaging basin structure with teleseismic virtual source reflection profiles: Geophysical Research Letters, v. 39, p. 6, doi: 10.1029/2011GL050035.

Yu, C.-Q., Chen, W.-P., and van der Hilst, R.D., 2013, Removing source-side scattering for virtual deep seismic sounding (VDSS): Geophysical Journal International, v. 195, p. 1932–1941, doi: 10.1093/gji/ggt359.

Zou, Z., Zhou, H. -w., and Gurrola, H., 2014, Teleseismic Virtual-Source Imaging of the Basin Structures in the Three Gorges Region, China: Bulletin of the

Seismological Society of America, v. 104, p. 2142–2147, doi: 10.1785/0120130110.

8 Tables

Table 1. Teleseismic earthquakes used in this work.

Date	Time (UTC)	Region	Lat (°N)	Long (°E)	Magnitude	Depth (km)	Distance (deg)	Distance (km)	BAZ (deg)
22-Feb-15	12:56:24	Colombia	2.73	-76.50	5.5	149	42.32	4697.2	131.6
19-Feb-15	16:32:47	Russia	52.81	159.01	5.4	82	65.65	7287.6	318.6
11-Feb-15	18:57:22	Argentina	-23.11	-66.69	6.7	223	68.90	7647.7	140.6
21-Feb-15	22:26:46	Colombia	4.67	-76.18	5.1	95	41.01	4552.3	129.4
17-Feb-15	4:46:39	Japan	40.11	141.89	5.5	47	82.34	9140.0	314.0

Table 2. Synthetic seismogram layer parameters. Each model used a different basin, as numbered.

	Upper Mantle	Crust	Basin 1	Basin 2	Basin 3	Basin 4	Basin 5	Basin 6*
Vp (km/s)	7.8	6.3	4	4	4	4	3	2.5
Vs (km/s)	4.2	3.6	2.1	2.1	2.1	2.1	1.6	1.3
Rho (g/cm³)	3.3	2.75	2.3	2.3	2.3	2.3	1.3	1.08
Width (km)	300	300	27.4 - 39.4	30.1 - 39.5	34.2 - 39.8	39.1 - 39.8	34.2 - 39.8	34.2 - 39.8
Depth (km)	~69	~31	4	5	5	5	5	5
Dip of Basin Edges (deg)			30°	45°	60°	80°	60°	60°

9   Figures
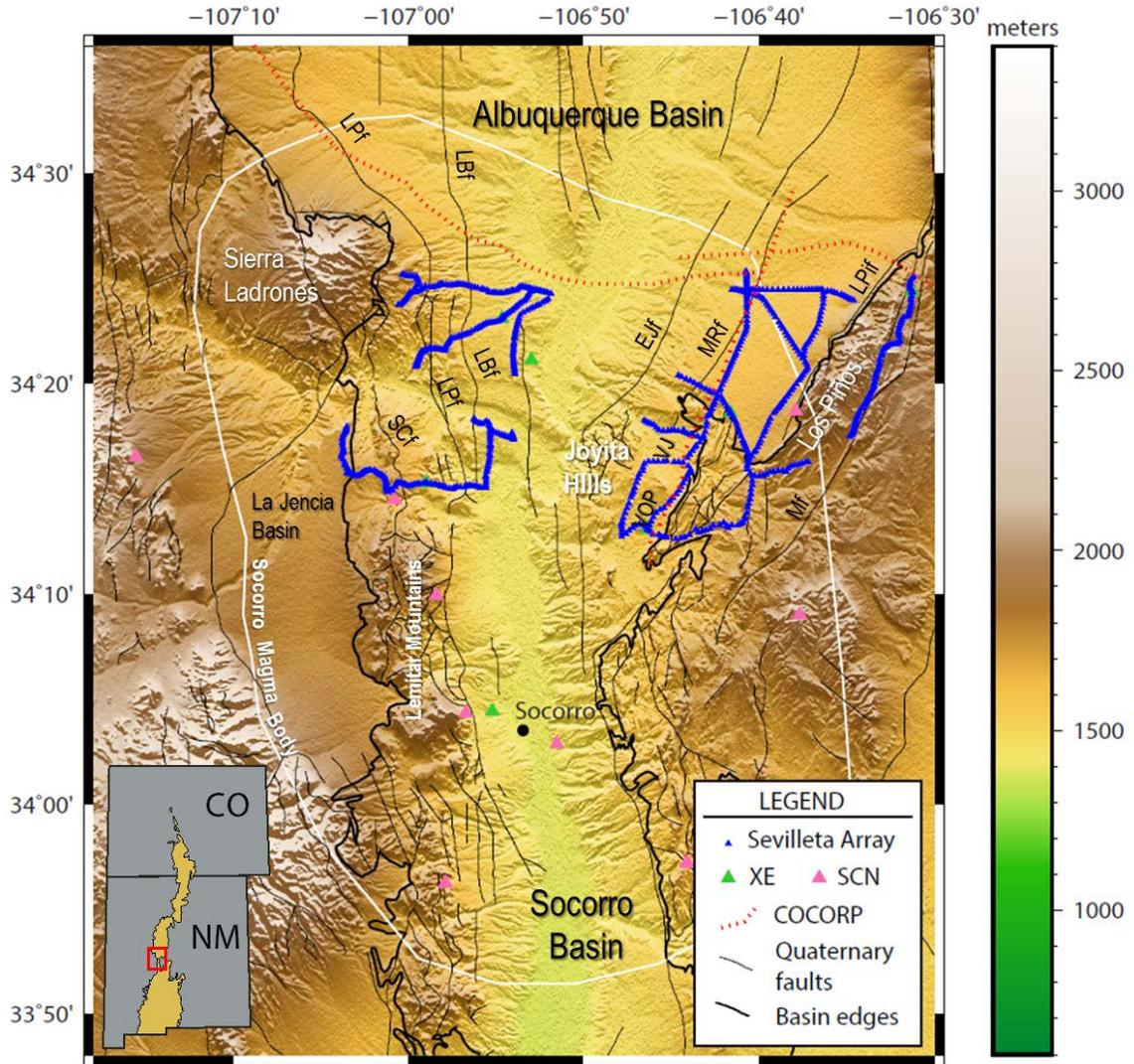
Figure 1: Map of the study area. Faults are abbreviated as follows: LPf – Loma Pelada fault, LBf – Loma Blanca fault, SCf – Silver Creek fault, EJf – East Joyita fault, MRf – Military Road fault, LPif – Los Piños fault, Mf – Montosa fault. The white outline is the estimated lateral extent of the Socorro magma body (Balch et al., 1997). Golden basins in the inset map are the basins of the Rio Grande Rift (modified from Grauch and Connell, 2013).
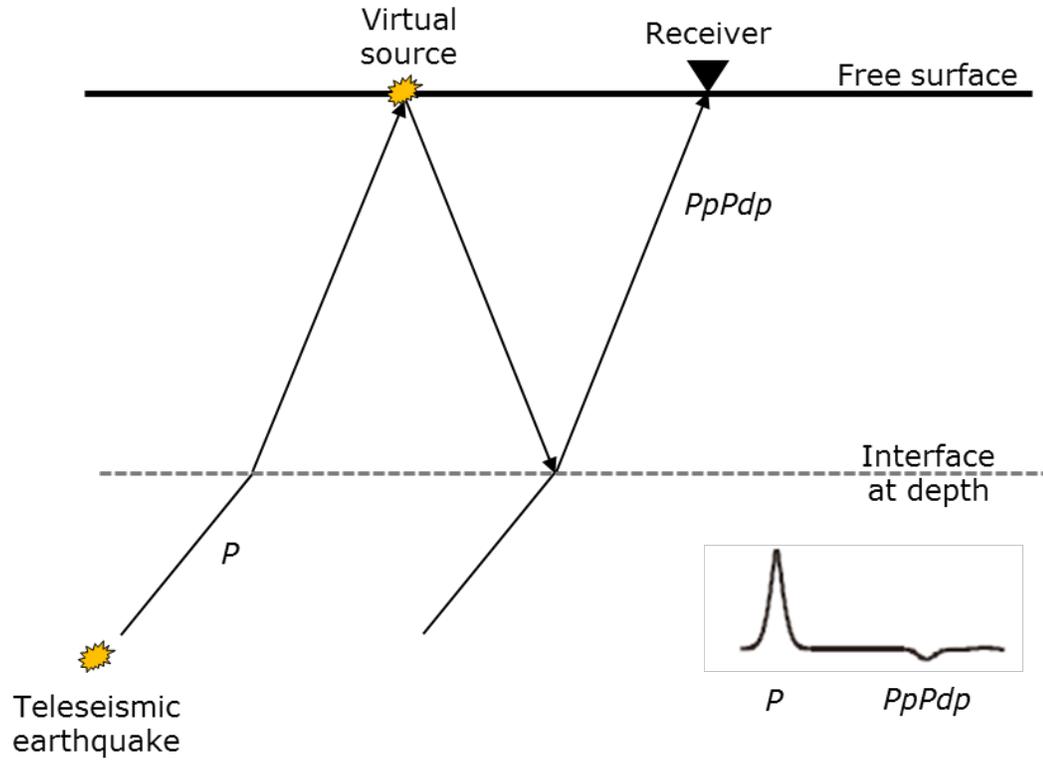
Figure 2: A diagram displaying the ray paths of the PpPdp (the d refers to an interface at depth) and P phases. The phases reflect off of free surface of the earth to act as virtual sources for the TVR method.

A. **Colombia M5.5, Popotosa line waveforms**
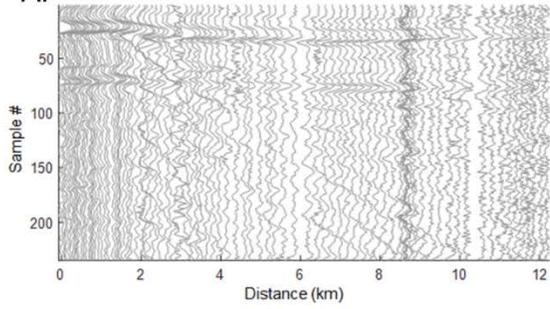
Russia M5.4, Popotosa line waveforms
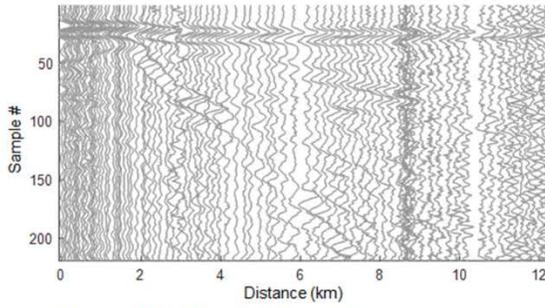
Argentina M6.7, Popotosa line waveforms
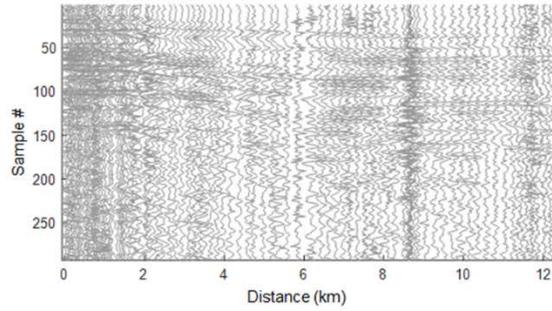
Colombia M5.1, Popotosa line waveforms
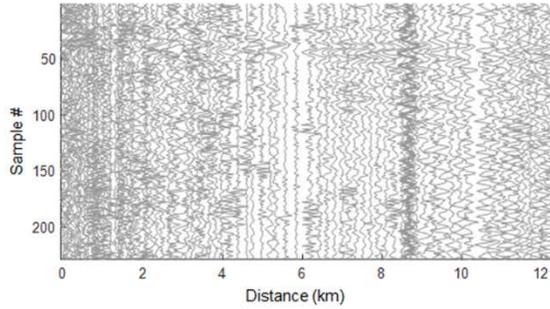
Japan M5.5, Popotosa line waveforms

57
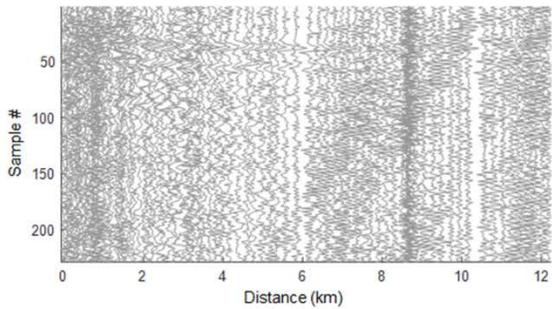
B. **Colombia 5.5 waveforms aligned by cross-correlation**
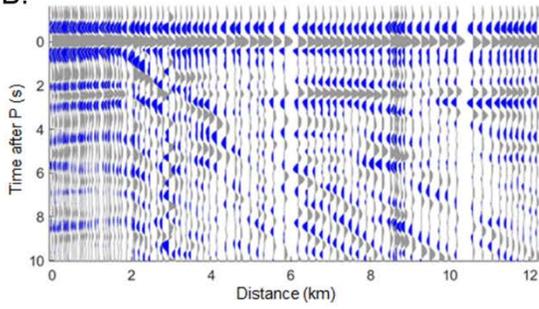
Russia M5.4 waveforms aligned by cross-correlation
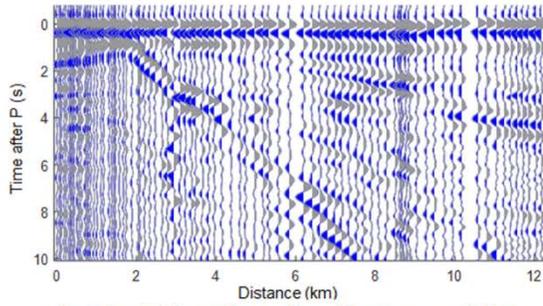
Argentina M6.7 waveforms aligned by cross-correlation
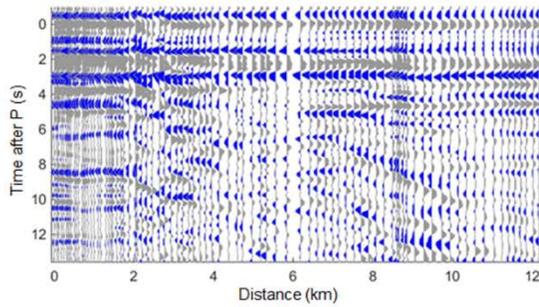
Colombia 5.1 waveforms aligned by cross-correlation
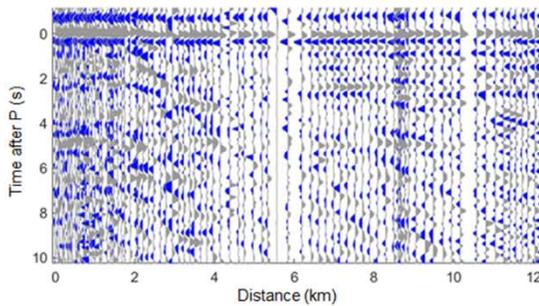
Japan M5.5 Waveforms aligned by cross-correlation

58

C. **Colombia M5.5, TVR Profile**

Russia M5.4, TVR Profile

Argentina M6.7, TVR Profile

Colombia M5.1, TVR Profile

Japan M5.5, TVR Profile
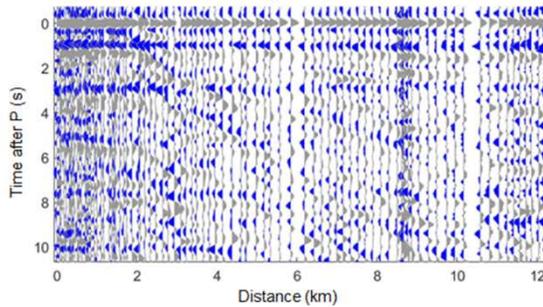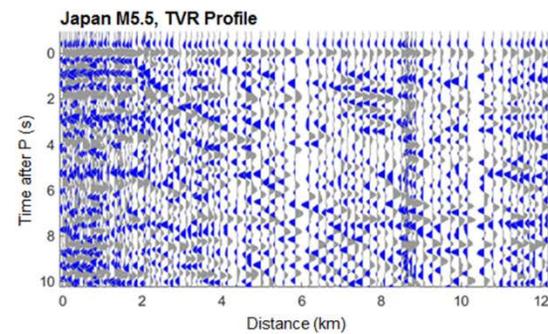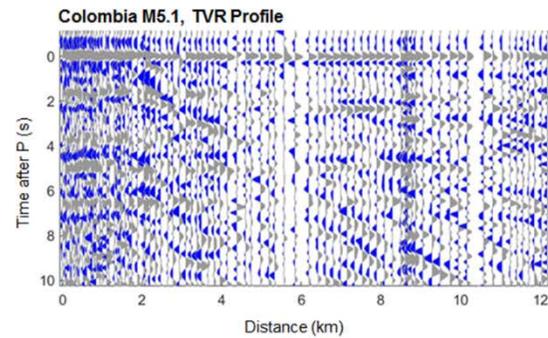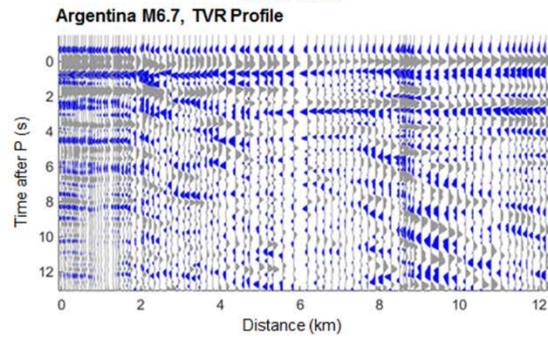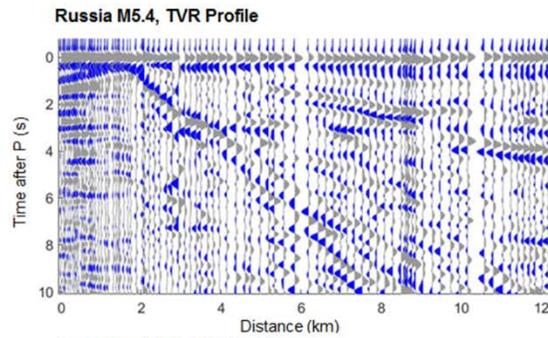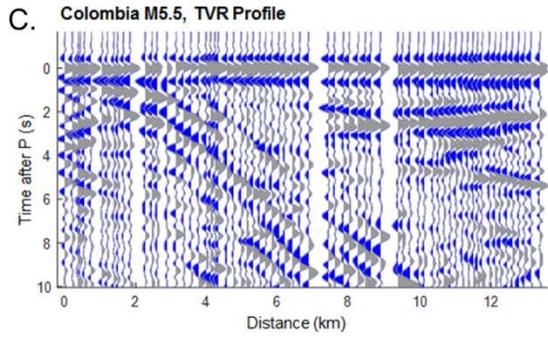
Figure 3: The TVR method broken down by step, and applied to each event used in this work on the Popotosa line. Events were ordered by best signal-to-noise. A. The first step approximately aligns the P-wave with a reduction velocity. The events presented were filtered from 0.2 to 3 Hz, except the Colombia M5.1, which was filtered from 0.1 to 2 Hz. B. The P-wave arrival is aligned by cross correlation to create a strict alignment. The waveforms here have been filtered between 0.2 and 1.5 Hz, except the Russia event which was filtered from 0.3 to 1.7 Hz. C. The final TVR profile is produced after deconvolution. All events presented were filtered from 0.25 to 1.5 Hz.

A. Colombia M5.5 Source Pulse

B. Russia M5.4 Source Pulse

C. Argentina M6.7 Source Pulse

D. Colombia M5.1 Source Pulse

E. Japan M5.5 Source Pulse
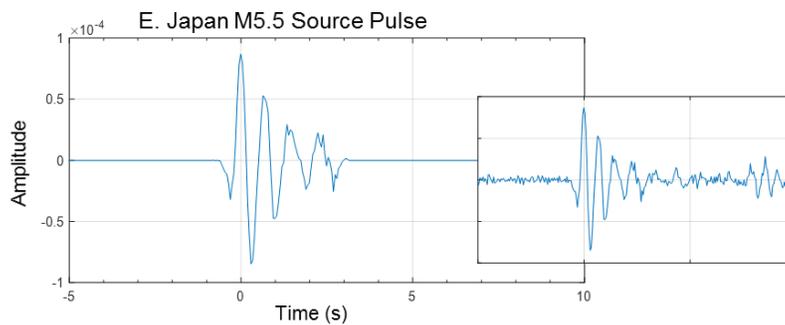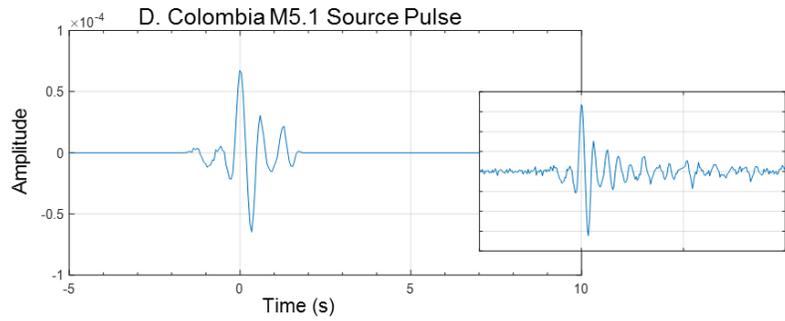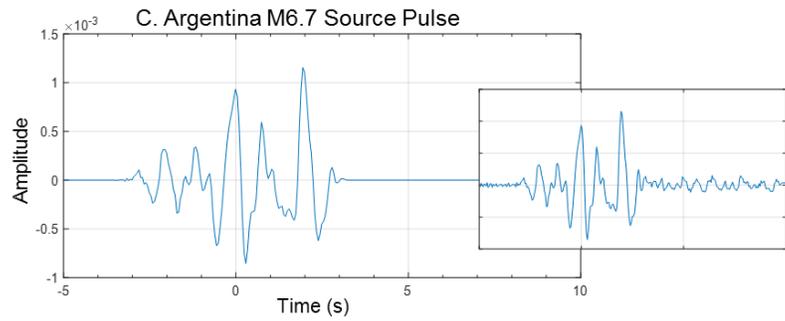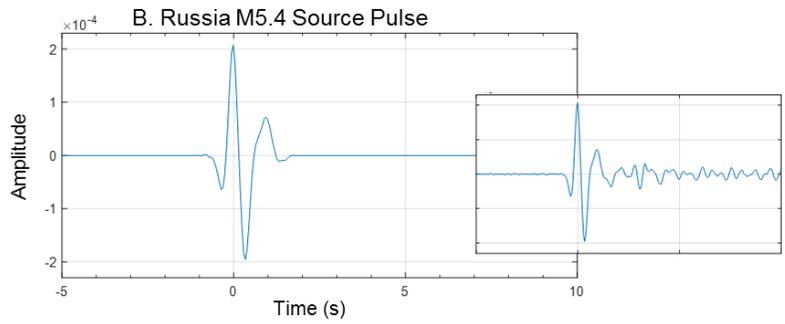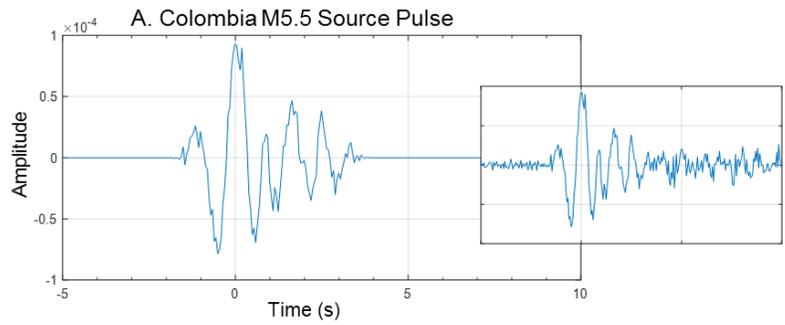
Figure 4: The estimated source pulse used in deconvolution for each event (left), as compared to the average pulse (right, small).

A. Colombia M5.5 Signal vs. Noise
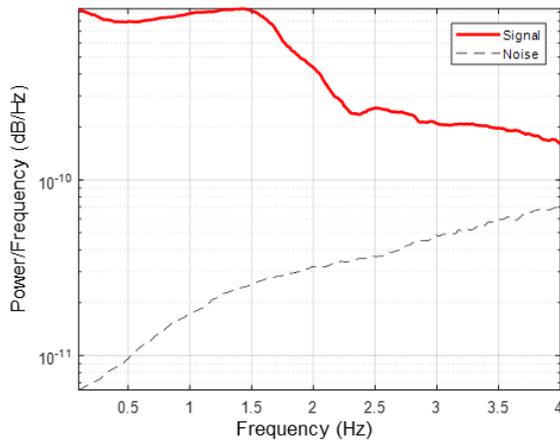
B. Russia Signal vs. Noise
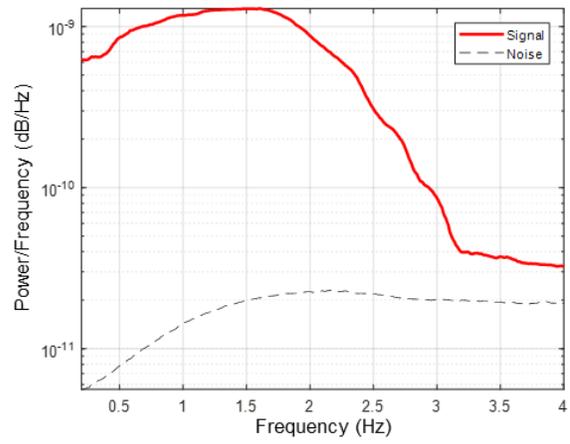
C. Argentina Signal vs. Noise
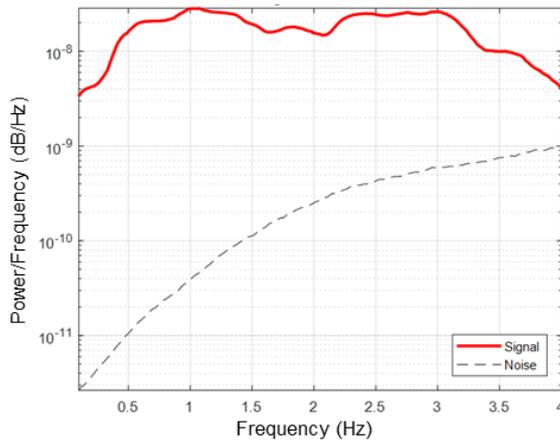
D. Colombia M5.1 Signal vs. Noise
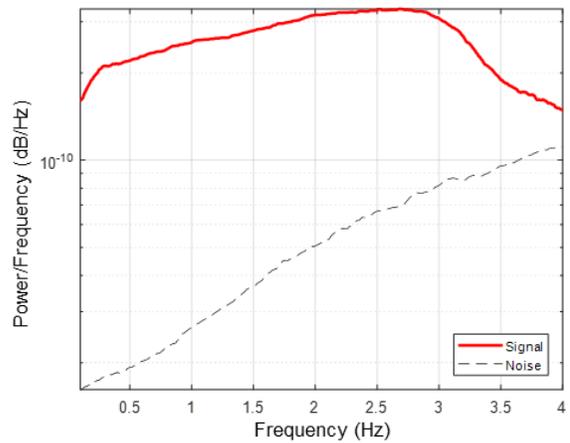
E. Japan Signal vs. Noise
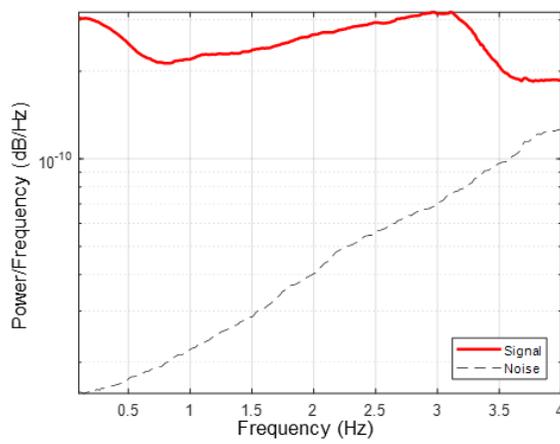
Figure 5: Signal to noise ratio plots of each of the teleseismic events used in this study.
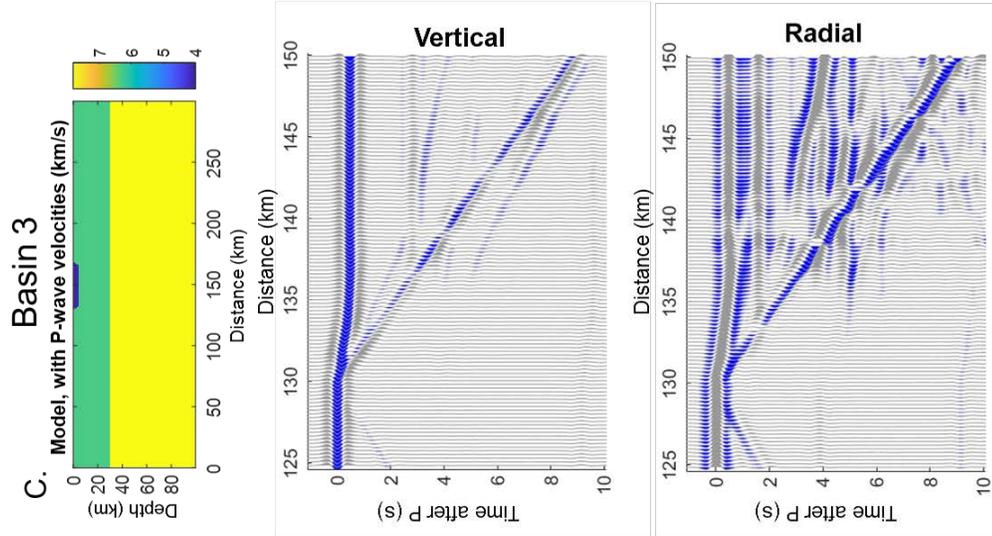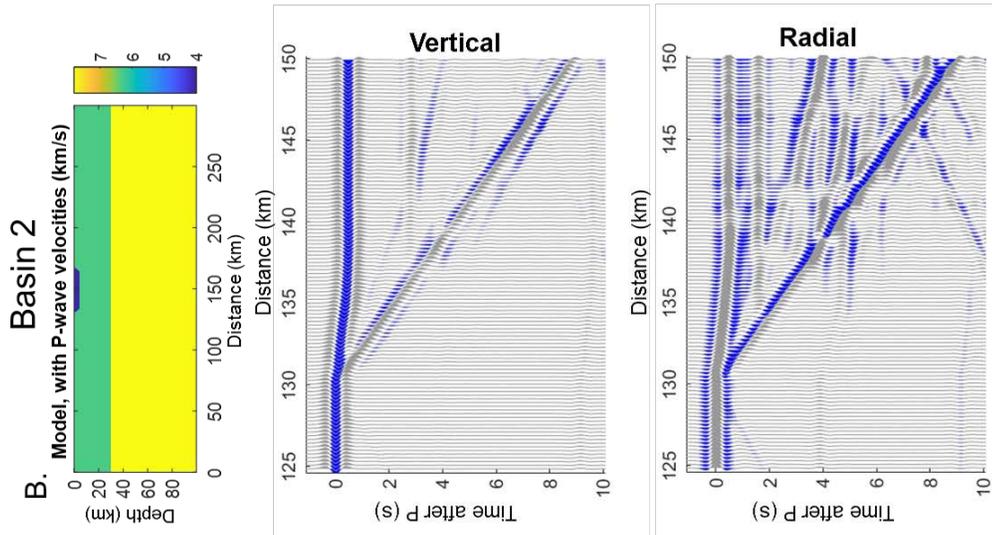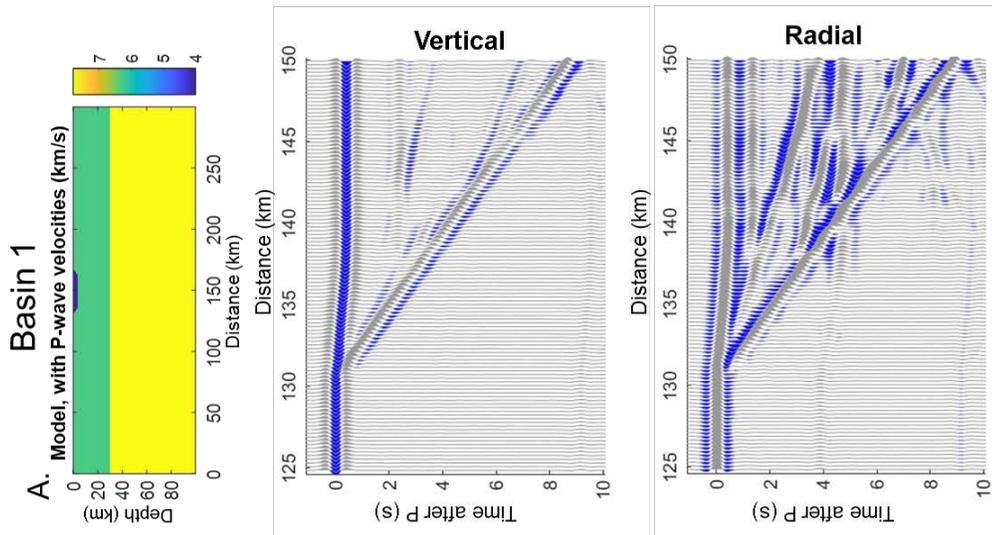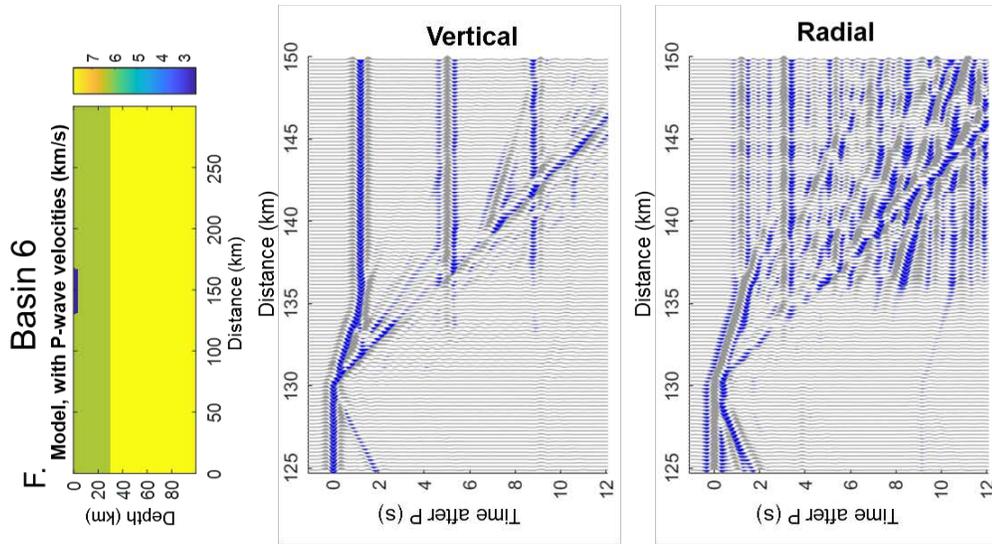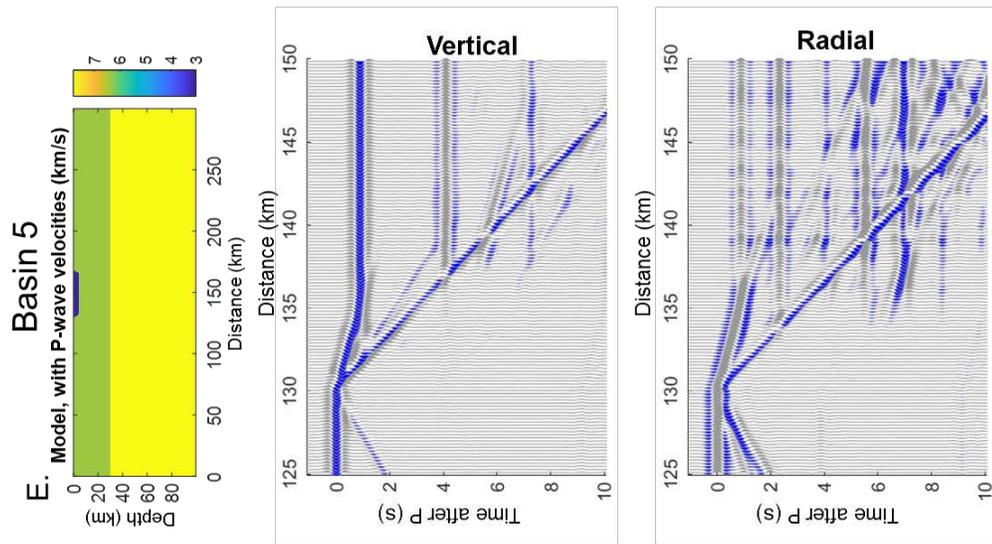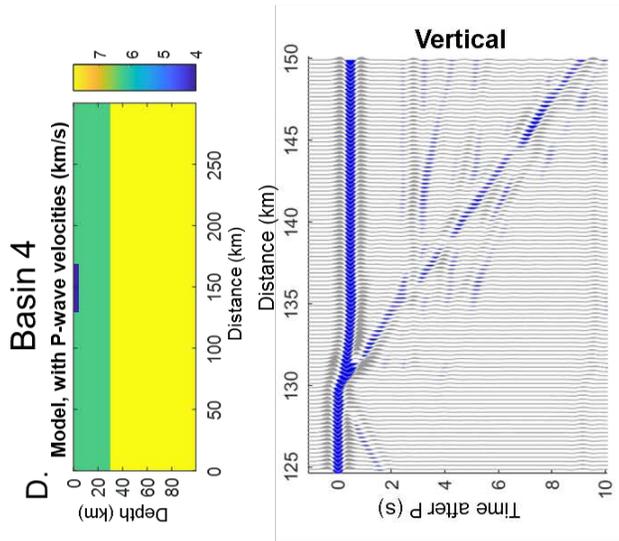
Figure 6: The models used to create synthetic seismograms (top), and the resulting vertical and radial components (middle and bottom respectively). A. The shallowest-dipping basin, with 30º basin edge dip (Basin 1 in Table 2). B. A basin bounded by 45º dip edge (Basin 2 in Table 2). C. A basin bounded by 60º dip edge (Basin 3 in Table 2). D. The steepest-dipping basin, with 80º basin edge dip (Basin 4 in Table 2). E. A basin bounded by 60º dip edge, like basin 3 but with a basin material velocity of 3 km/s (Basin 5 in Table 2). F. A basin bounded by 60º dip edge, like basins 3 and 5, but with a basin material velocity of 2.5 km/s (Basin 6 in Table 2).
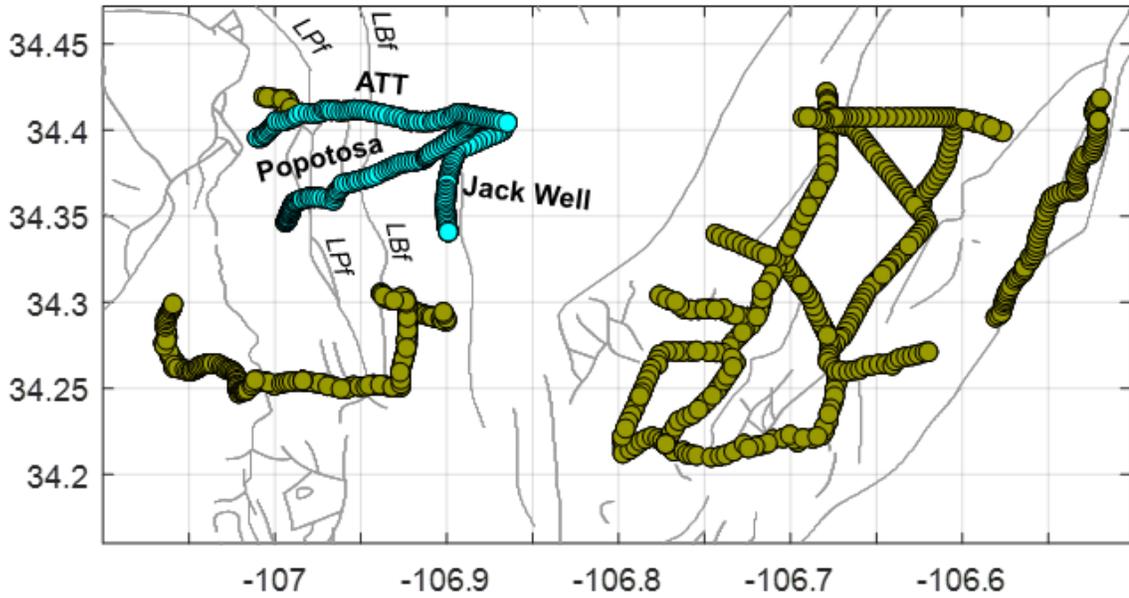
Figure 7: Map of the northwest quadrant of the Sevilleta Array with profile lines highlighted in cyan and labelled. The relevant faults are labelled as follows: LPf – Loma Pelada fault and LBf – Loma Blanca fault.
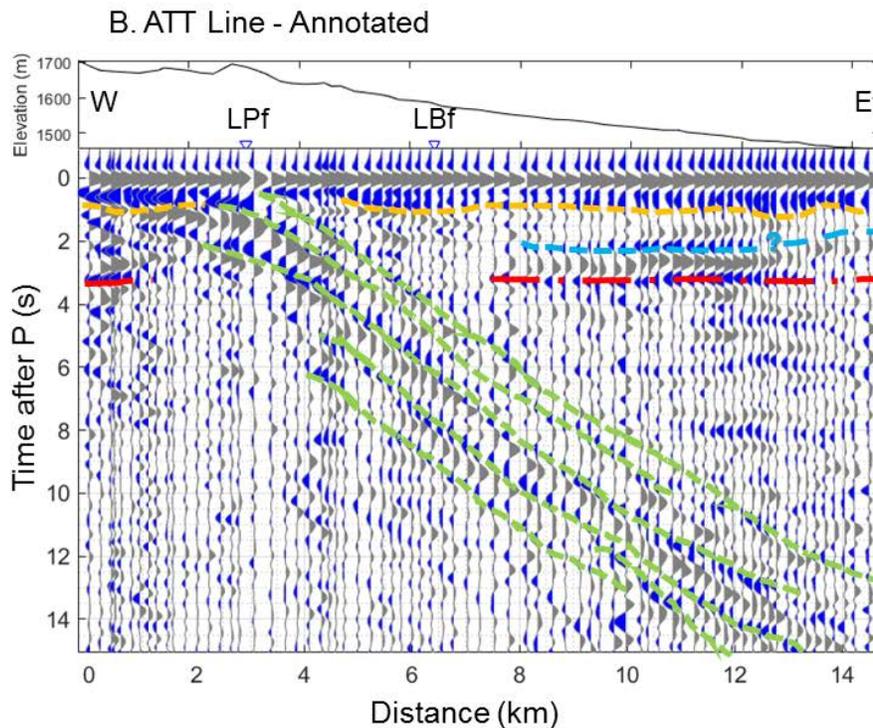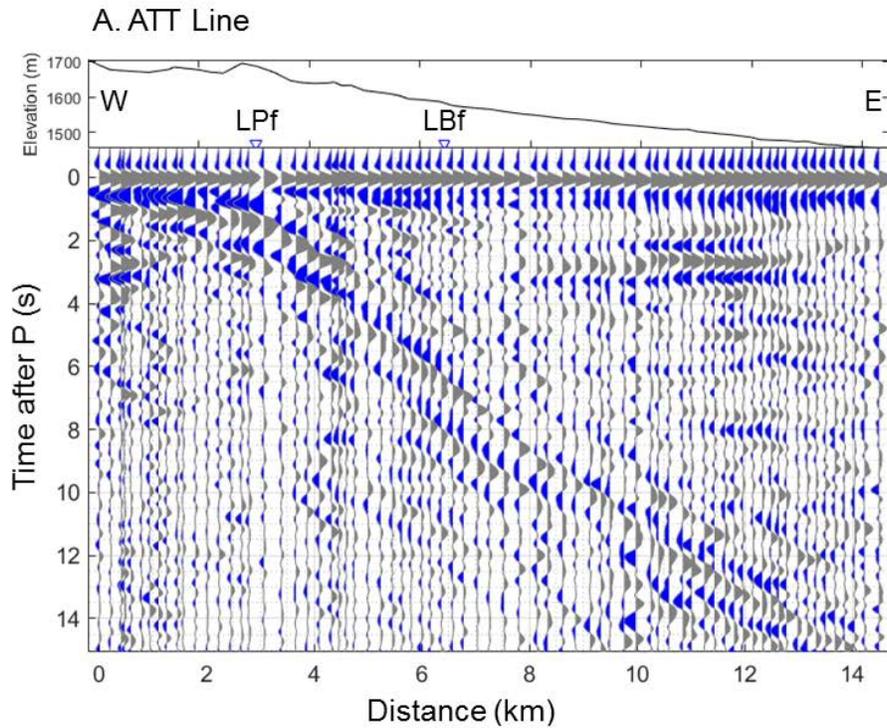
Figure 8: A. The ATT line TVR profile overlain by corresponding topography. Time is shown to 15 seconds depth (~45 kilometers) to show extent of dipping reflectors. Distance is from the westernmost trace. Faults are labelled as follows: LPf – Loma Pelada fault and LBf – Loma Blanca fault. B. The same as A, but with annotated features discussed in text.

ATT Line – Northwest frequency bins
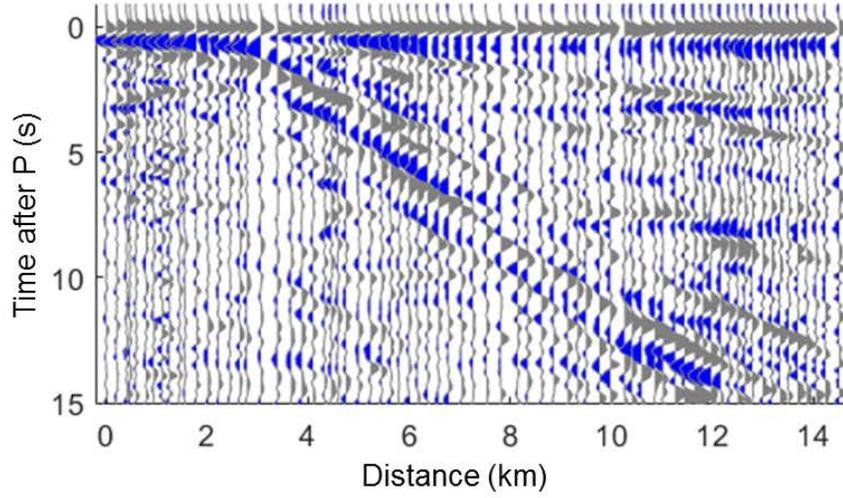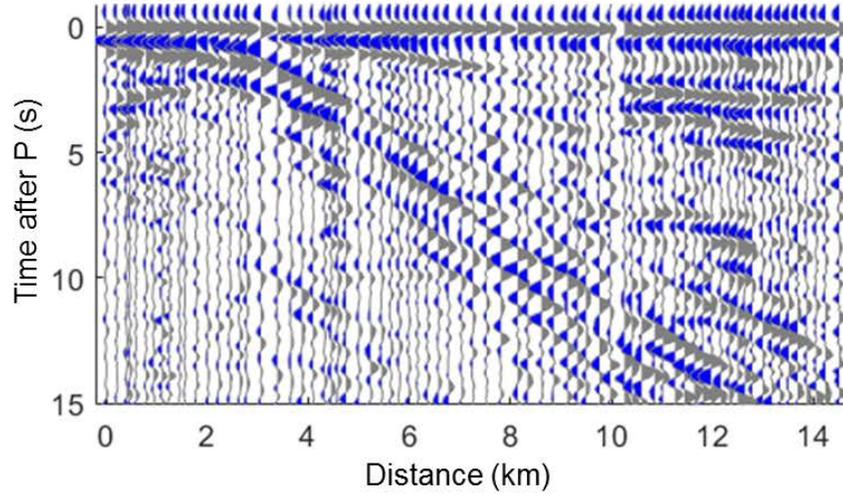
A. 0.1 – 0.5 Hz
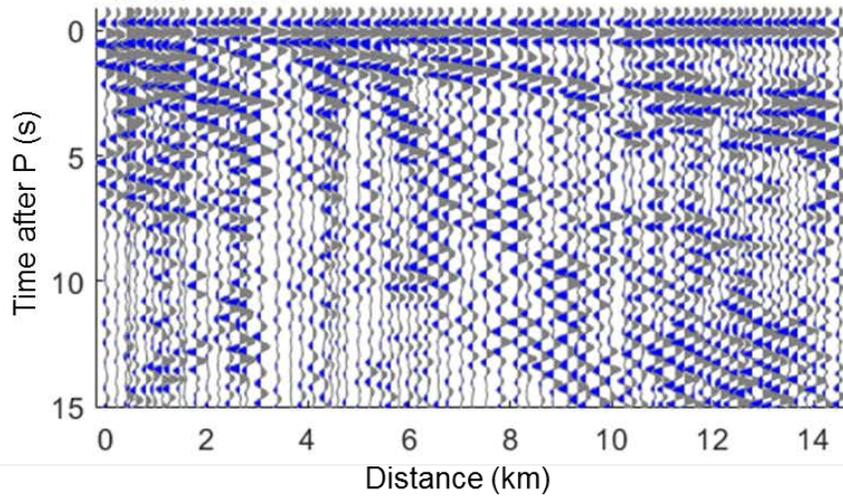
B. 0.5 – 1.0 Hz

C. 1.0 – 1.5 Hz

ATT Line – Southeast frequency bins

D. 0.1 – 0.5 Hz
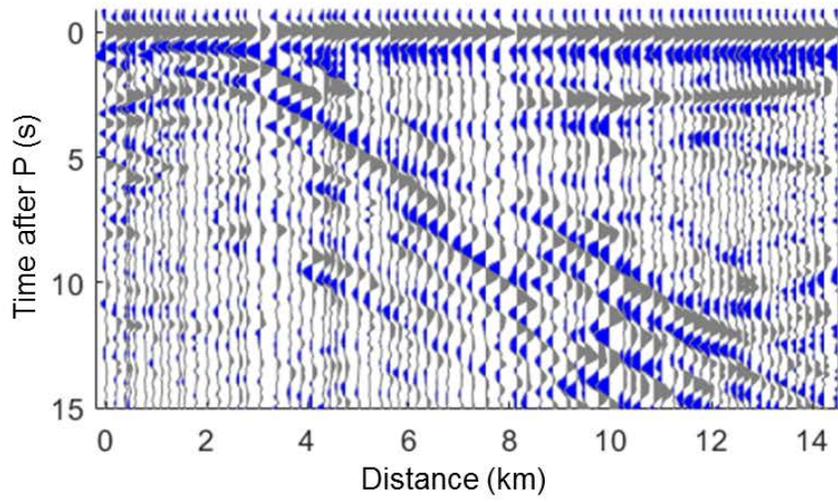
E. 0.5 – 1.0 Hz
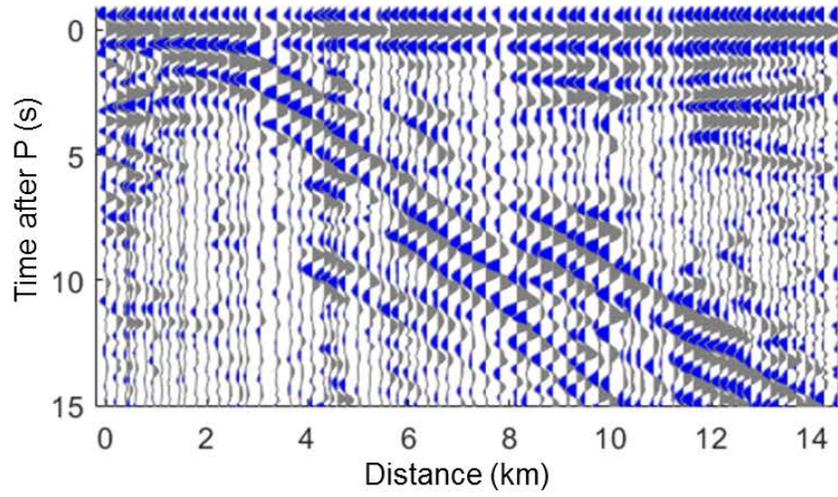
F. 1.0 – 1.5 Hz
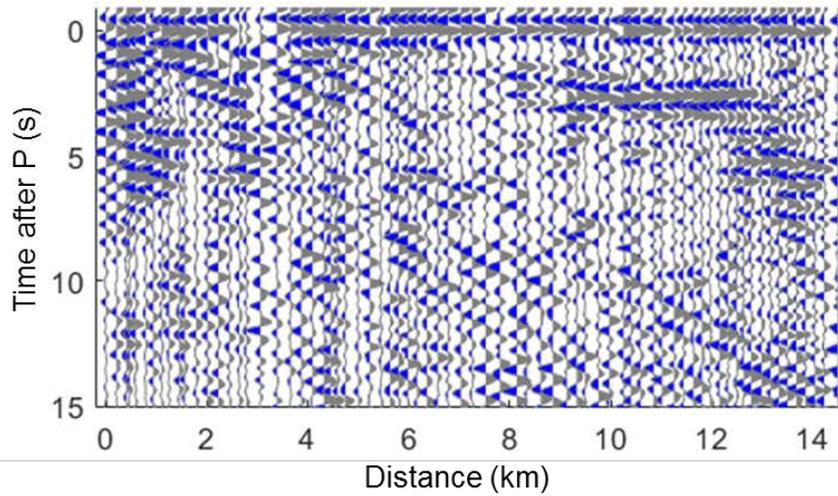
Figure 9: ATT TVR profile separated by azimuth and by frequency bin. Northwest events (A,B,C) are Russia and Japan. Southwest events (D,E,F) are both Colombia earthquakes and Argentina. Frequency bins only extend to 1.5 Hz due to signal-to-noise degradation at higher frequencies.
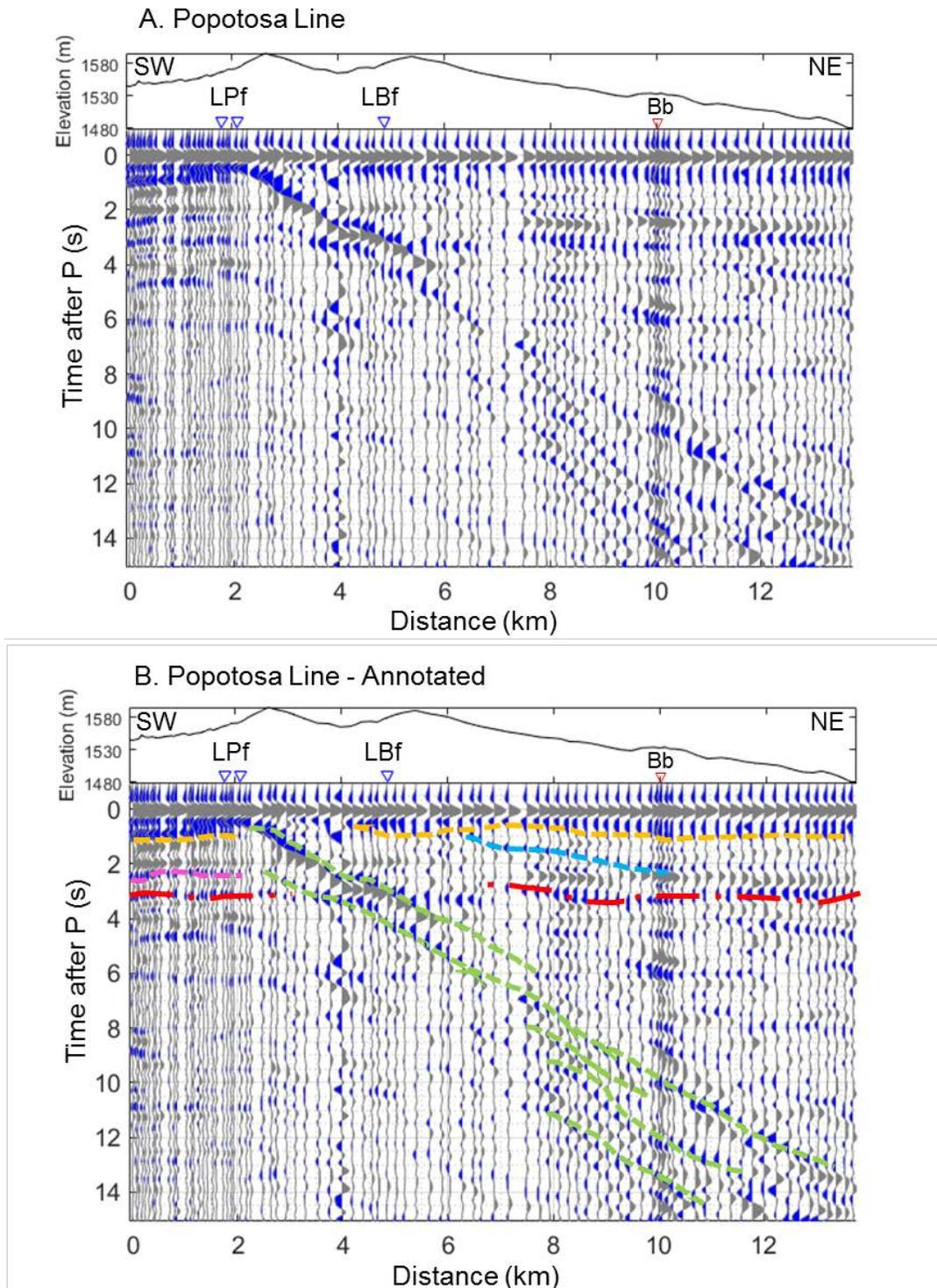
Figure 10: A. The Popotosa line TVR profile overlain by corresponding topography. Time is shown to 15 seconds depth (~45 kilometers) to show extent of dipping reflectors. Distance is from the southwesternmost trace. Bb is the location of the broadband station on the line. Faults are labelled as follows: LPf – Loma Pelada fault and LBf – Loma Blanca fault. B. The same as A, but with annotated features discussed in text.

Popotosa Line – Northwest frequency bins
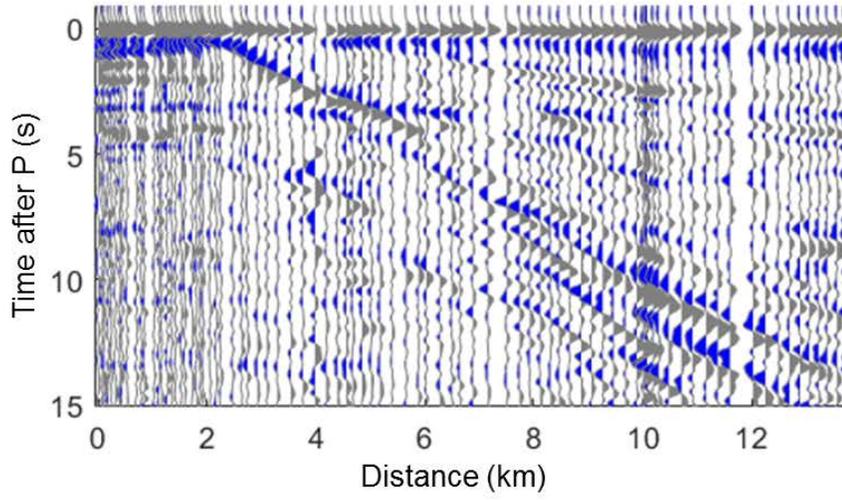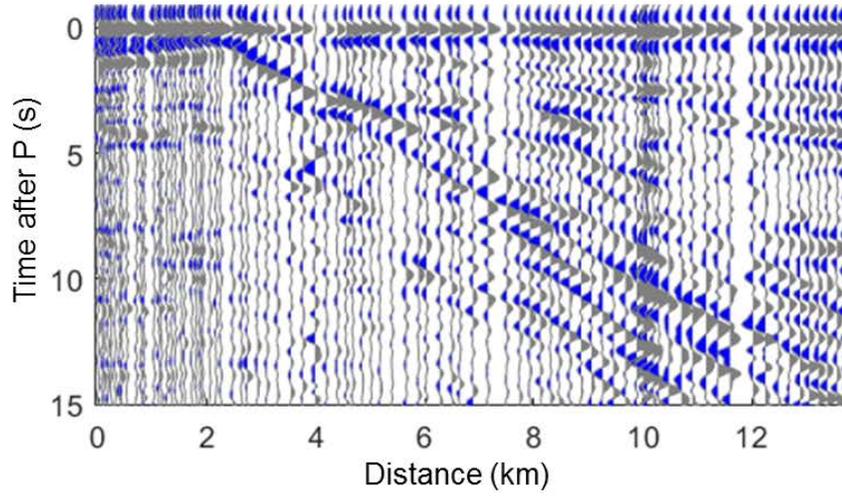
A. 0.1 – 0.5 Hz
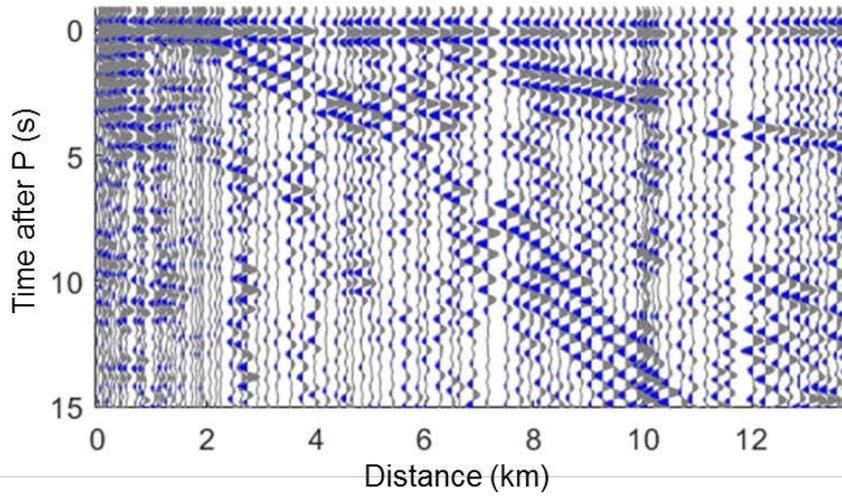
B. 0.5 – 1.0 Hz

C. 1.0 – 1.5 Hz

Popotosa Line – Southeast frequency bins

D. 0.1 – 0.5 Hz
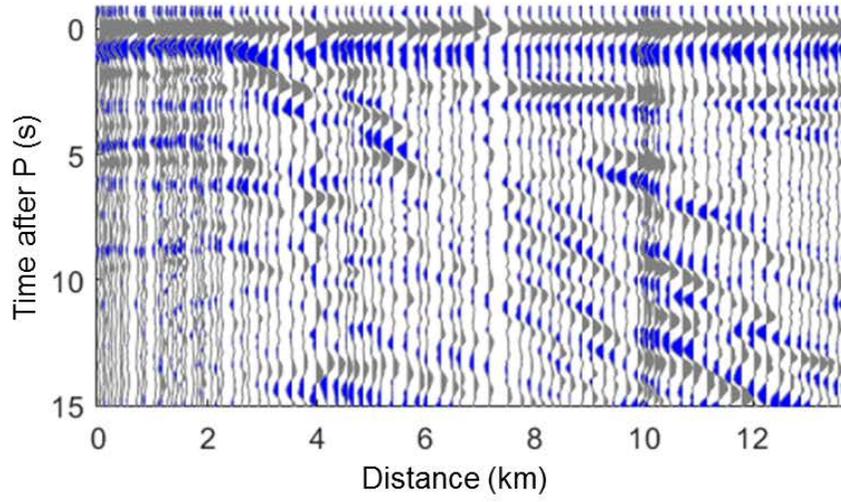
E. 0.5 – 1.0 Hz
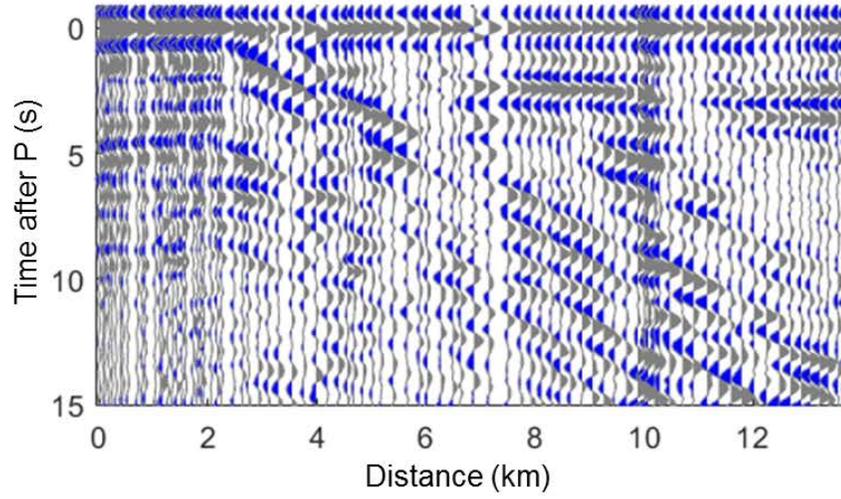
F. 1.0 – 1.5 Hz
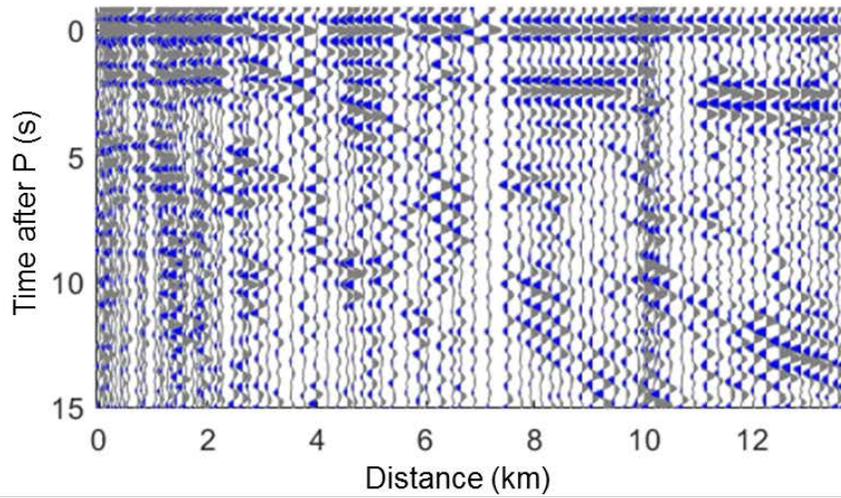
Figure 11: Popotosa TVR profile separated by azimuth and by frequency bin. Northwest events (A,B,C) are Russia and Japan. Southwest events (D,E,F) are both Colombia earthquakes and Argentina. Frequency bins only extend to 1.5 Hz due to signal-to-noise degradation at higher frequencies.

A. Jack Well Line

B. Jack Well Line - Annotated
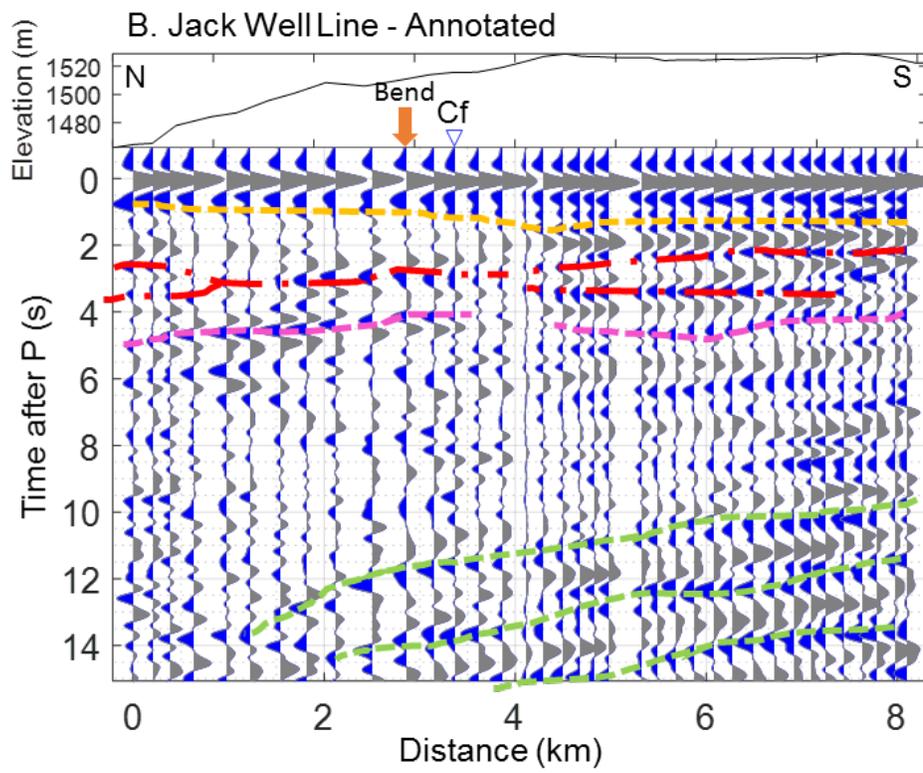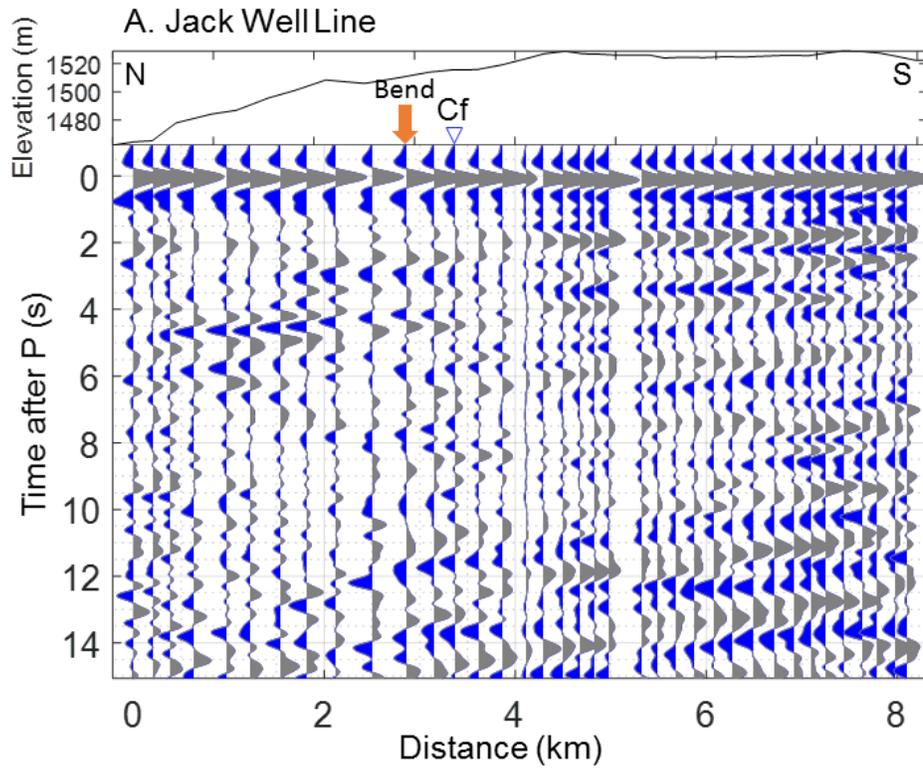
Figure 12: A. The Jack Well line TVR profile overlain by corresponding topography. Time is shown to 15 seconds depth (~45 kilometers) to show arrival of intense reflectors. Distance is from the northernmost trace. Slight bend to the northeast in the line is labeled by the orange arrow. The fault labeled Cf is the Cliff fault. B. The same as A, but with annotated features discussed in text.

Jack Well Line – Northwest frequency bins
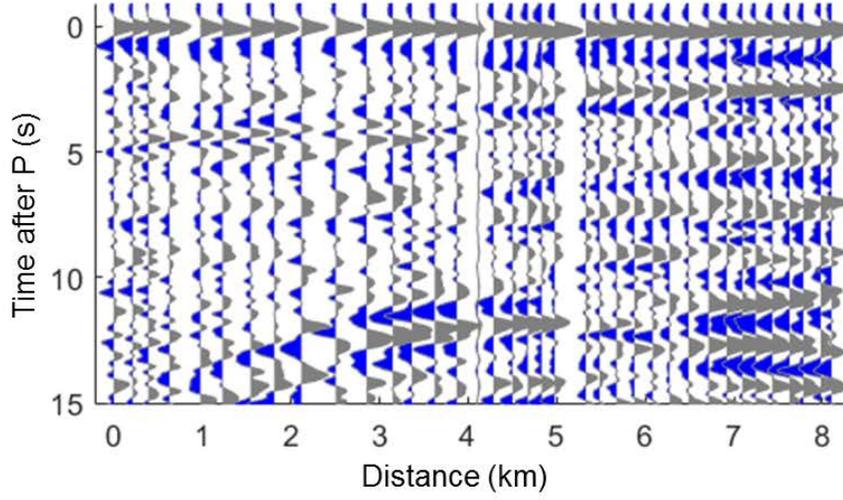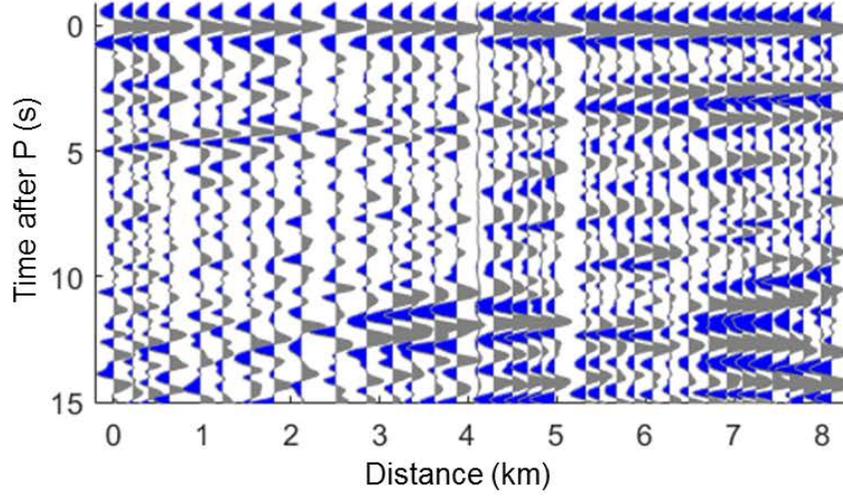
A. 0.1 – 0.5 Hz
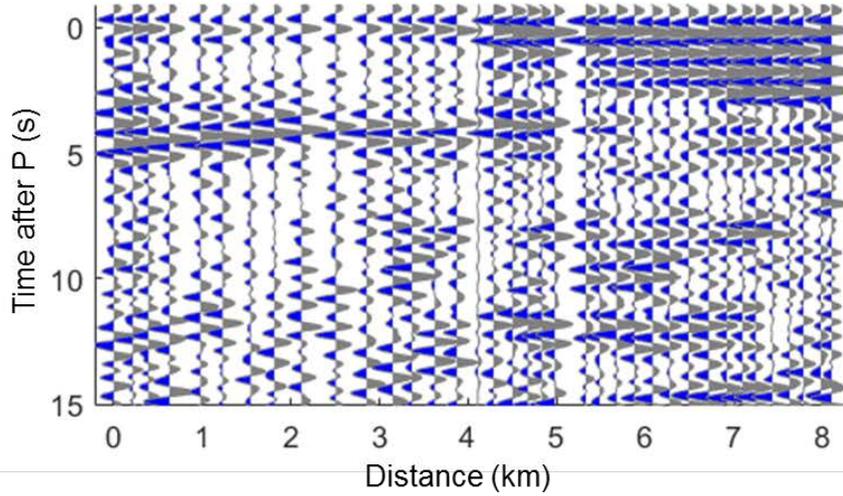
B. 0.5 – 1.0 Hz

C. 1.0 – 1.5 Hz

Jack Well Line – Southeast frequency bins

D. 0.1 – 0.5 Hz
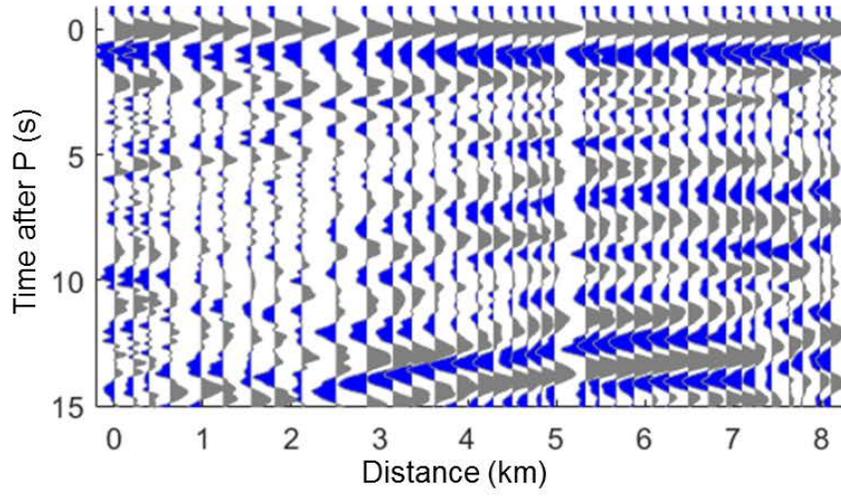
E. 0.5 – 1.0 Hz
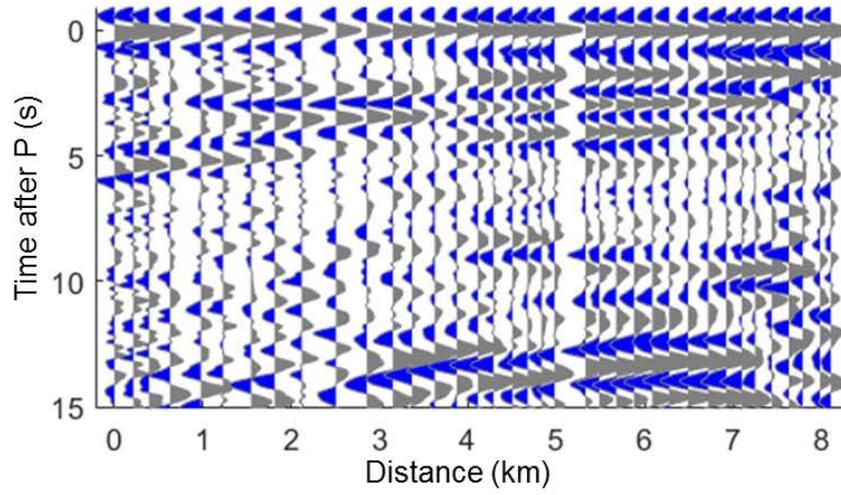
F. 1.0 – 1.5 Hz
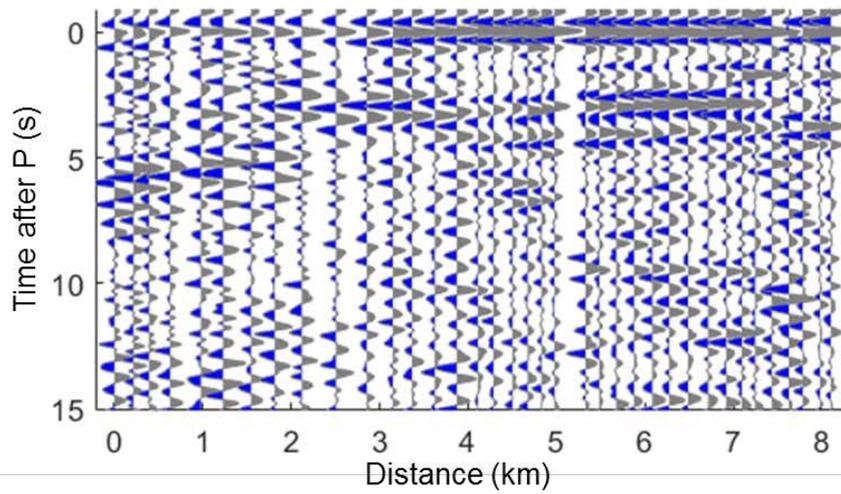
Figure 13: Jack Well TVR profile separated by azimuth and by frequency bin. Northwest events (A,B,C) are Russia and Japan. Southwest events (D,E,F) are both Colombia earthquakes and Argentina. Frequency bins only extend to 1.5 Hz due to signal-to-noise degradation at higher frequencies.
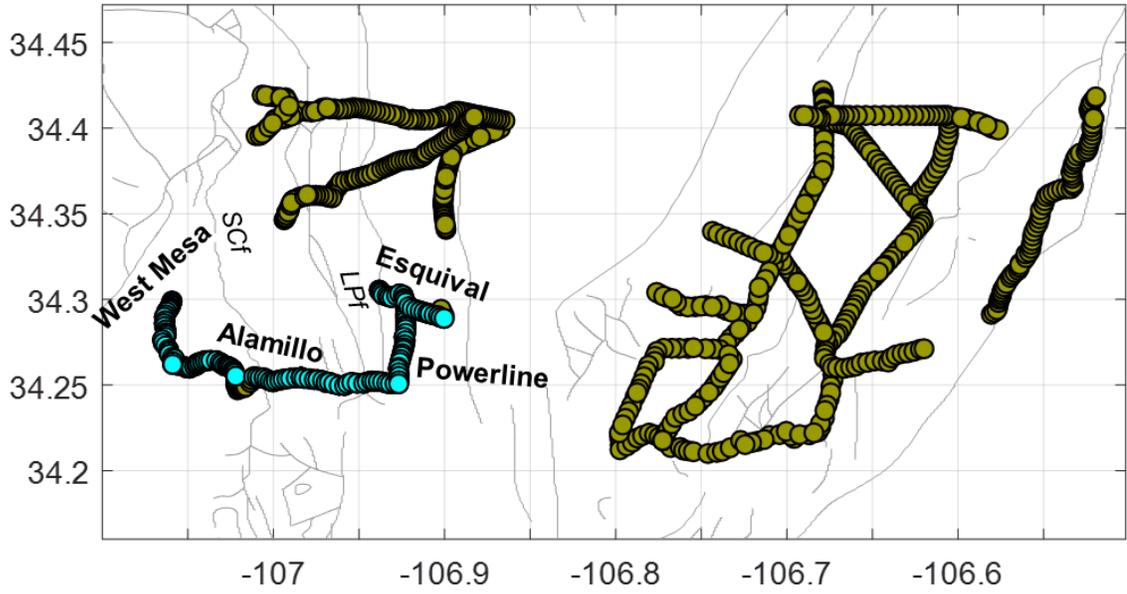
Figure 14: Map of the southwest quadrant of the Sevilleta Array with profile lines highlighted in cyan and labelled. The relevant faults are labelled as follows: LPf – Loma Pelada fault and SCf – Silver Creek fault.

A. West Mesa Line

B. West Mesa Line - Annotated
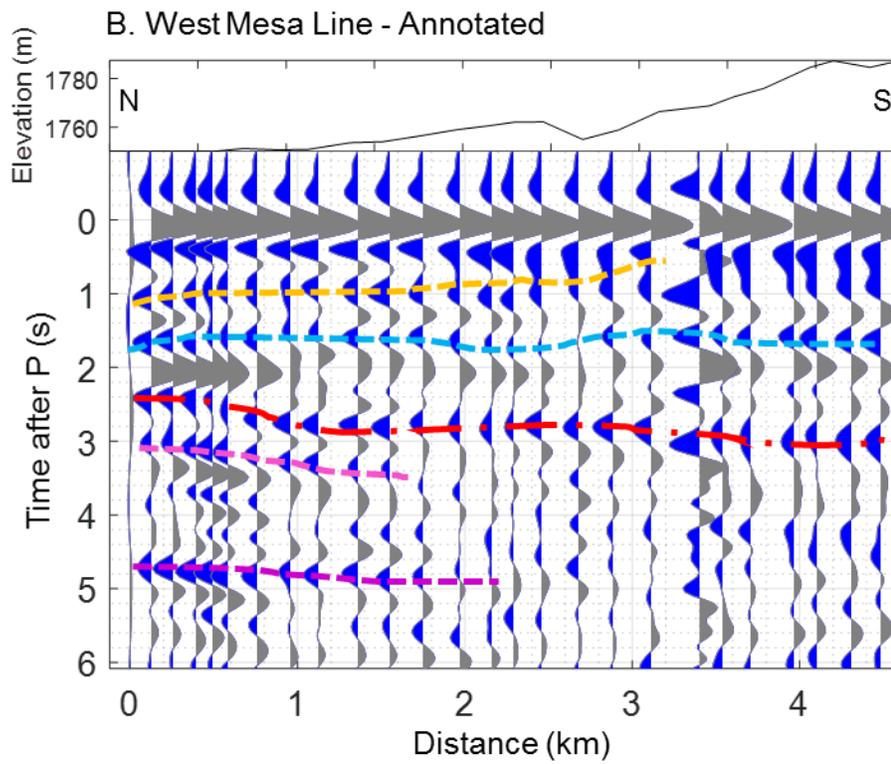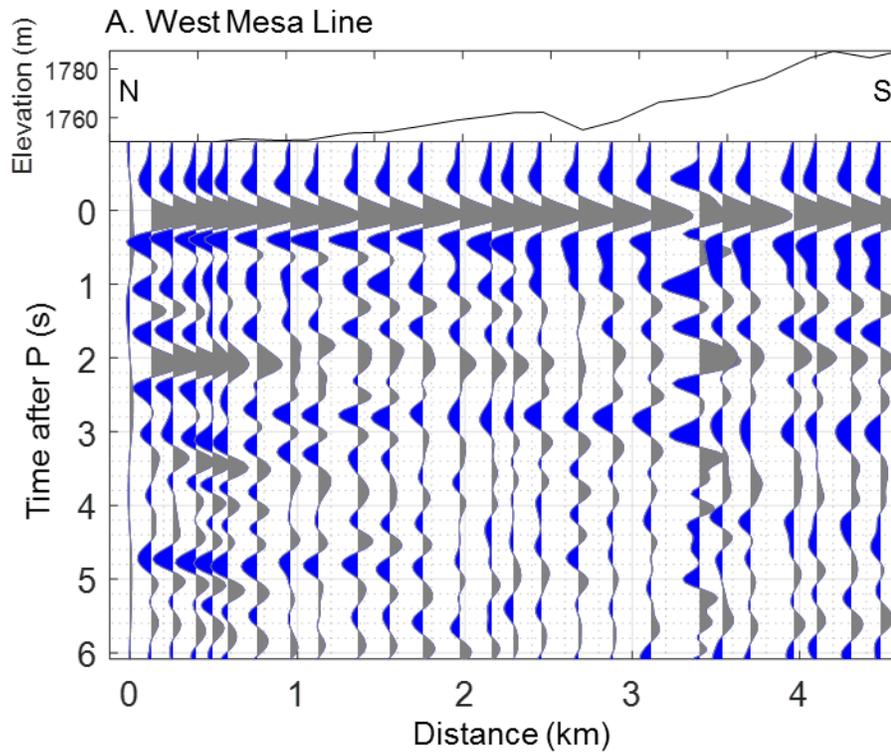
Figure 15: A. The West Mesa line TVR profile overlain by corresponding topography. Time is shown to 6 seconds depth (~20 kilometers) to focus on shallow crustal arrivals. Distance is from the northernmost trace. B. The same as A, but with annotated features discussed in the text.

West Mesa Line – Northwest frequency bins
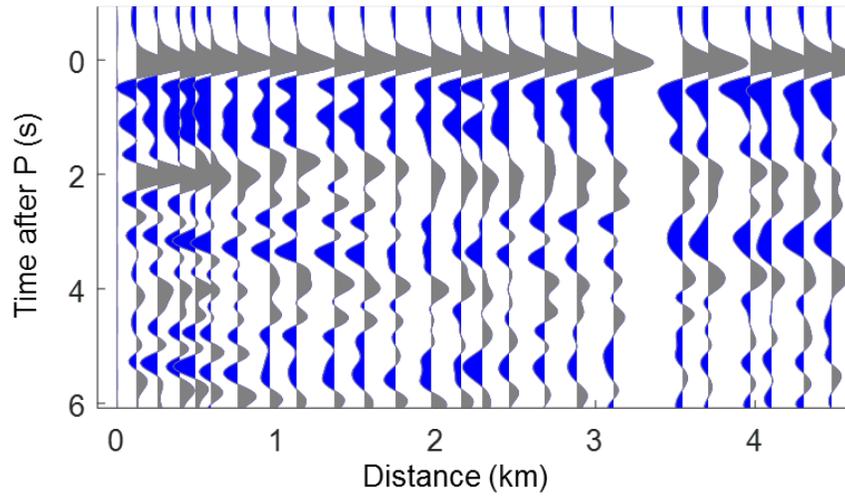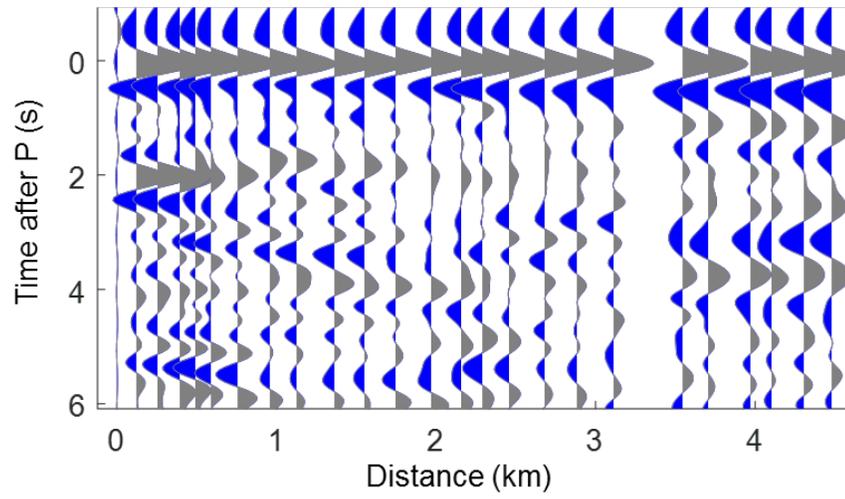
A. 0.1 – 0.5 Hz
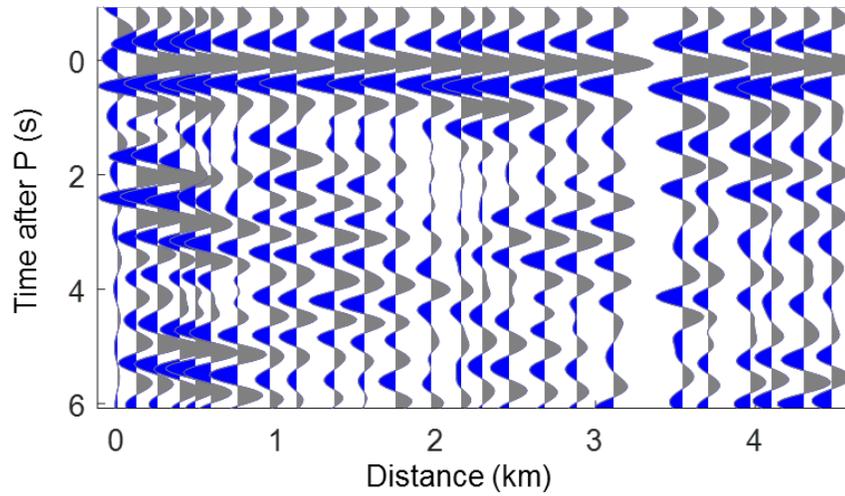
B. 0.5 – 1.0 Hz

## C. 1.0 – 1.5 Hz

West Mesa Line – Southeast frequency bins

D. 0.1 – 0.5 Hz
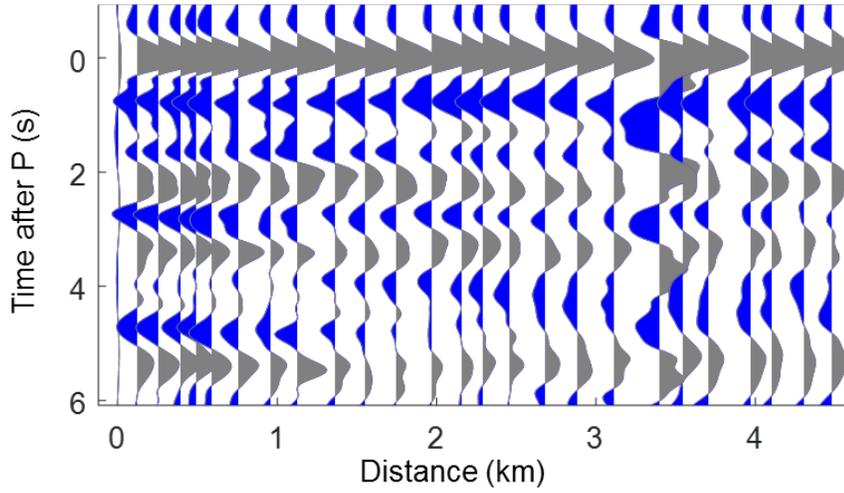
E. 0.5 – 1.0 Hz
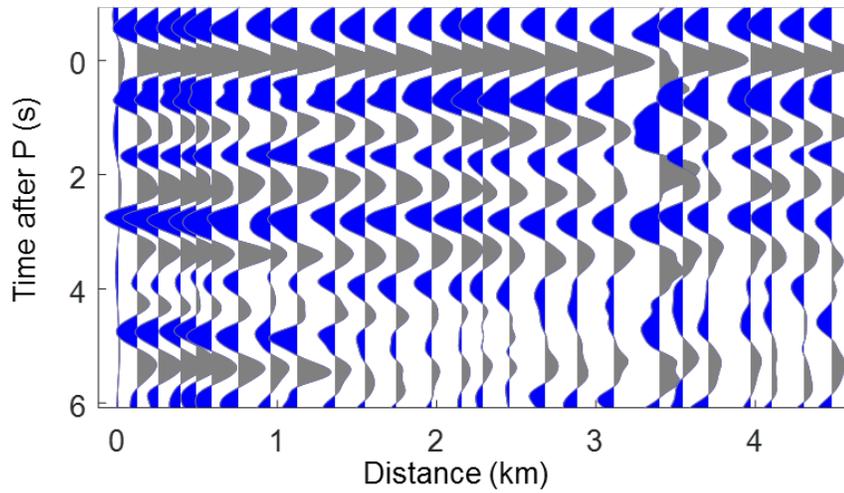
F. 1.0 – 1.5 Hz
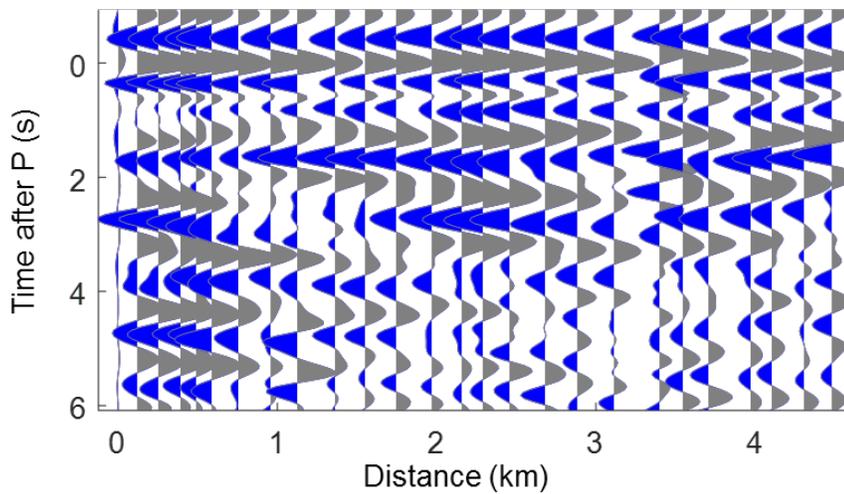
Figure 16: West Mesa TVR profile separated by azimuth and by frequency bin. Northwest events (A,B,C) are Russia and Japan. Southwest events (D,E,F) are both Colombia earthquakes and Argentina. Frequency bins only extend to 1.5 Hz due to signal-to-noise degradation at higher frequencies.

A. Alamillo Line

B. Alamillo Line - Annotated
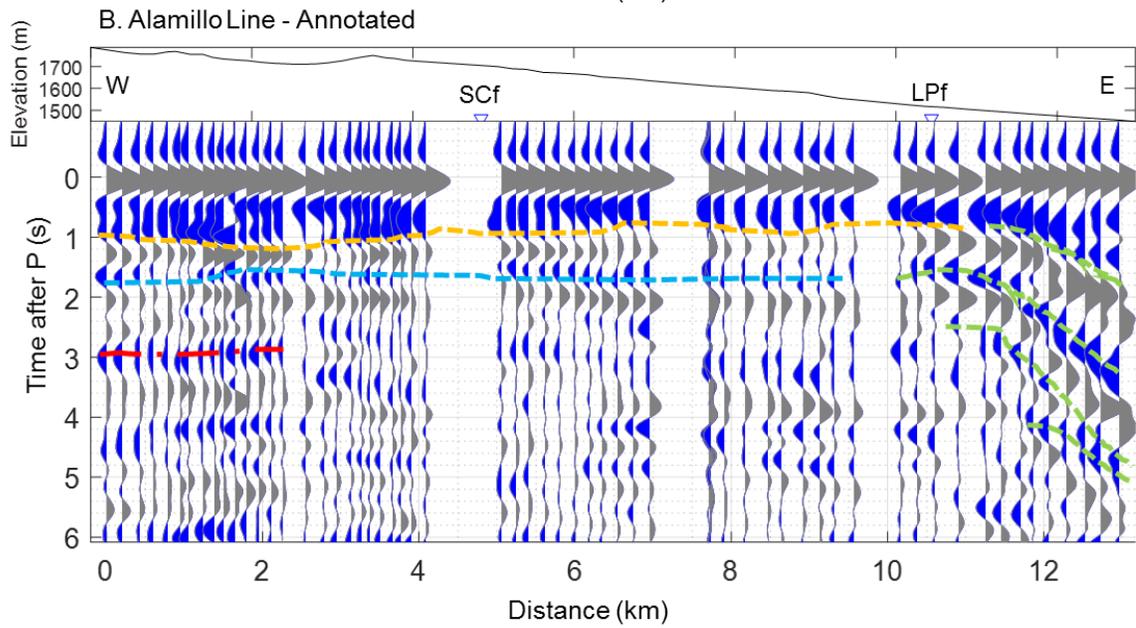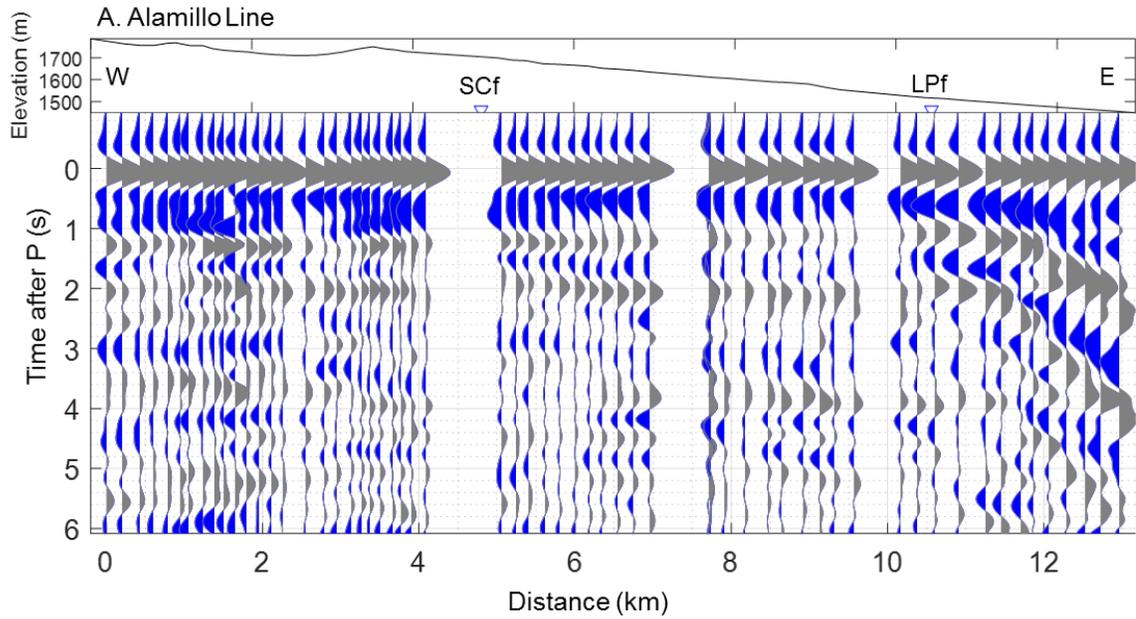
Figure 17: A. The Alamillo line TVR profile overlain by corresponding topography. Time is shown to 6 seconds depth (~20 kilometers) to focus on shallow crustal arrivals. Distance is from the westernmost trace. Faults are labelled as follows: SCf – Silver Creek fault, LPf – Loma Pelada fault. B. The same as A, but with annotated features discussed in the text.

Alamillo Line – Northwest frequency bins
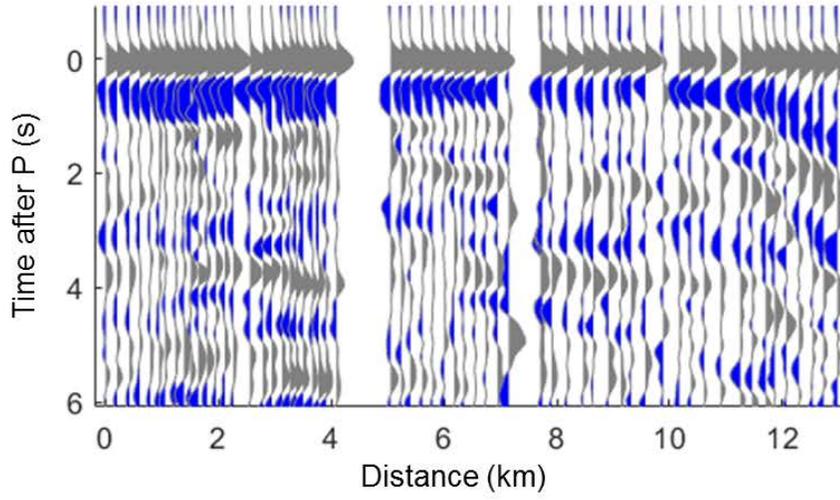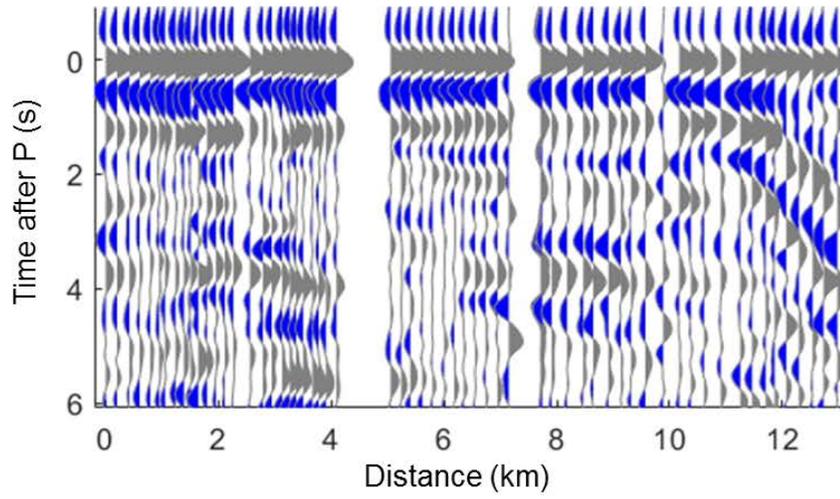
A. 0.1 – 0.5 Hz
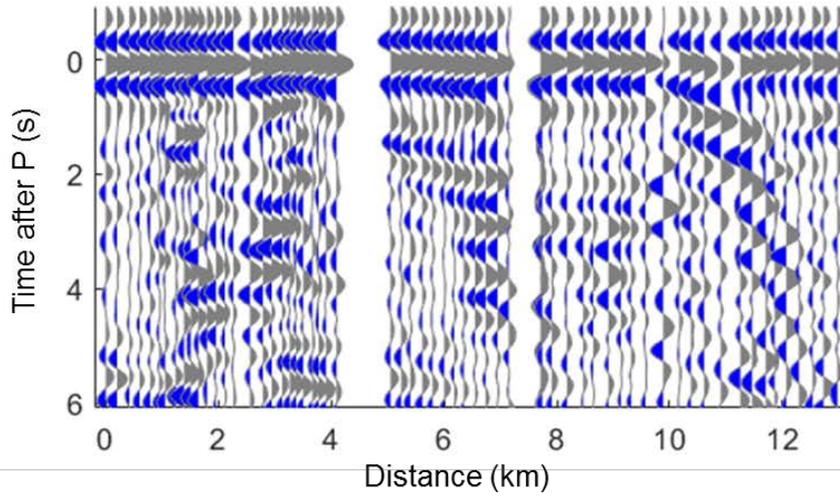
B. 0.5 – 1.0 Hz

C. 1.0 – 1.5 Hz

Alamillo Line – Southeast frequency bins

D. 0.1 – 0.5 Hz
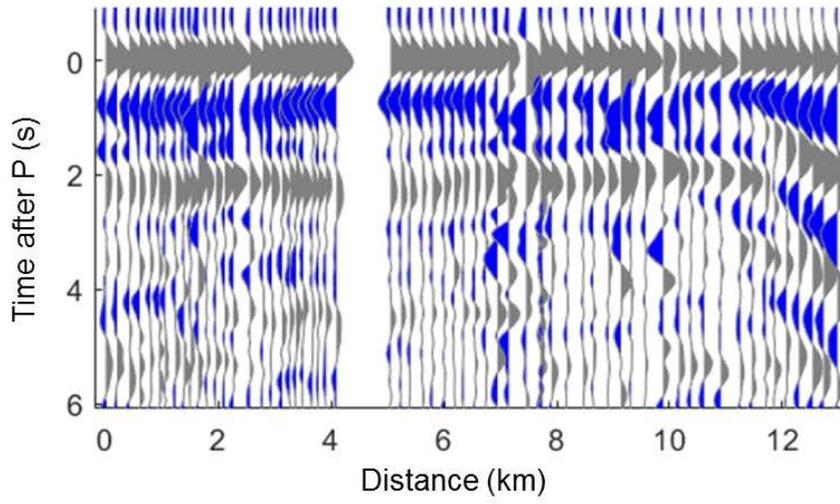
E. 0.5 – 1.0 Hz
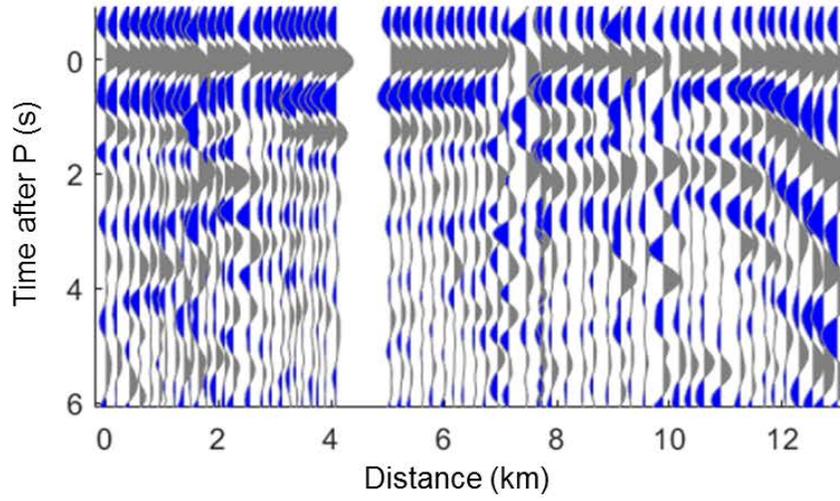
F. 1.0 – 1.5 Hz
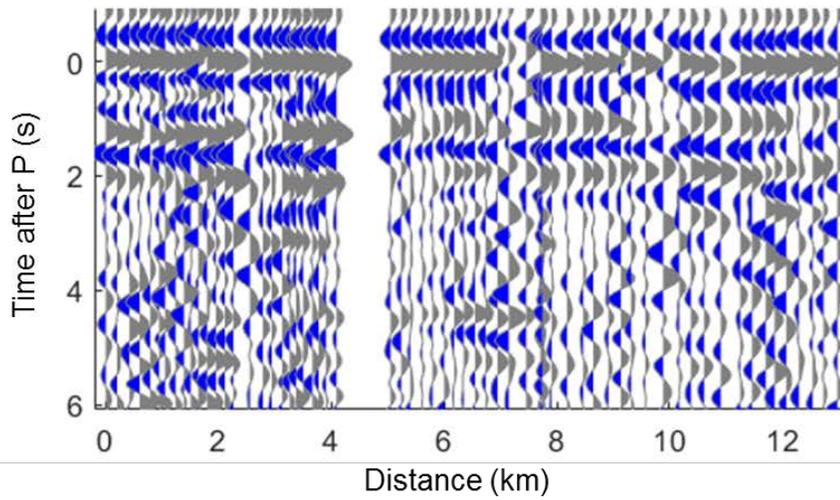
Figure 18: Alamillo TVR profile separated by azimuth and by frequency bin. Northwest events (A,B,C) are Russia and Japan. Southwest events (D,E,F) are both Colombia earthquakes and Argentina. Frequency bins only extend to 1.5 Hz due to signal-to-noise degradation at higher frequencies.

A. Powerline Line

B. Powerline Line - Annotated
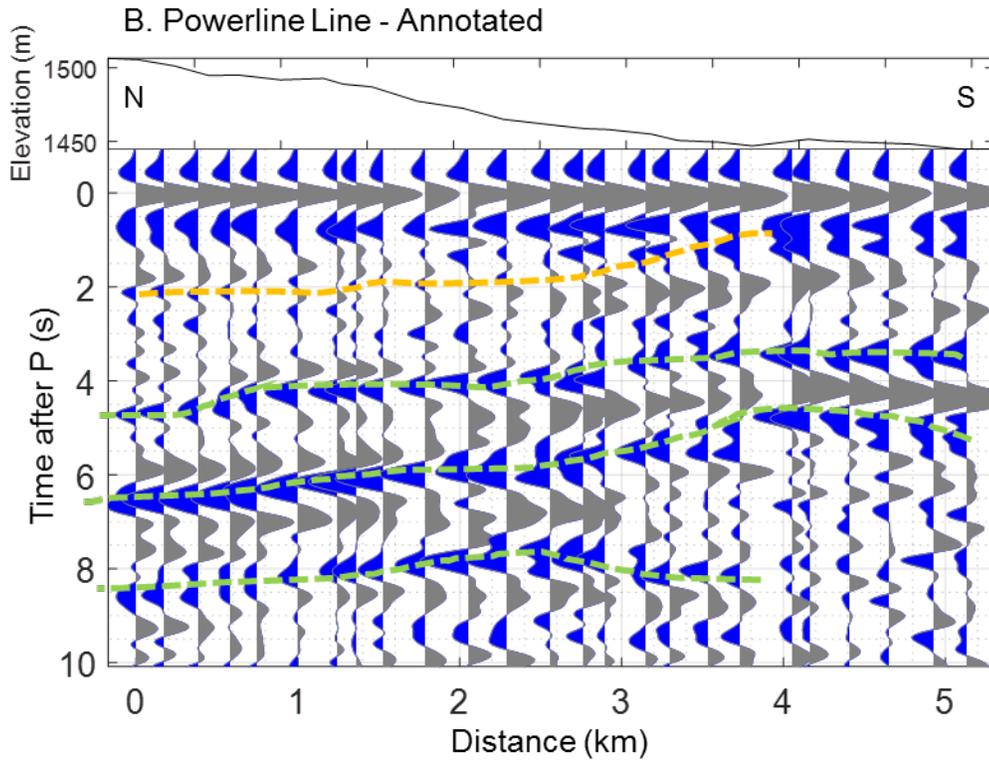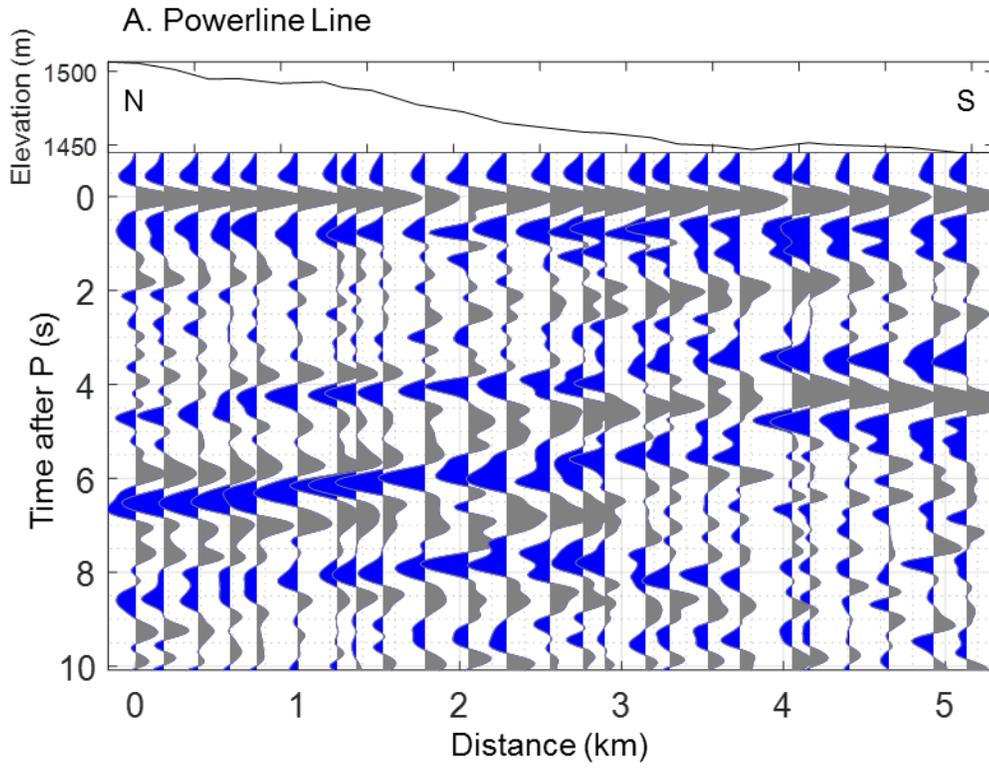
Figure 19: A. The Powerline line TVR profile overlain by corresponding topography. Time is shown to 10 seconds depth (~30 kilometers) to focus display depth of the intense series of reflectors. Distance is from the northernmost trace. B. The same as A, but with annotated features discussed in the text.

# Powerline Line – Northwest frequency bins
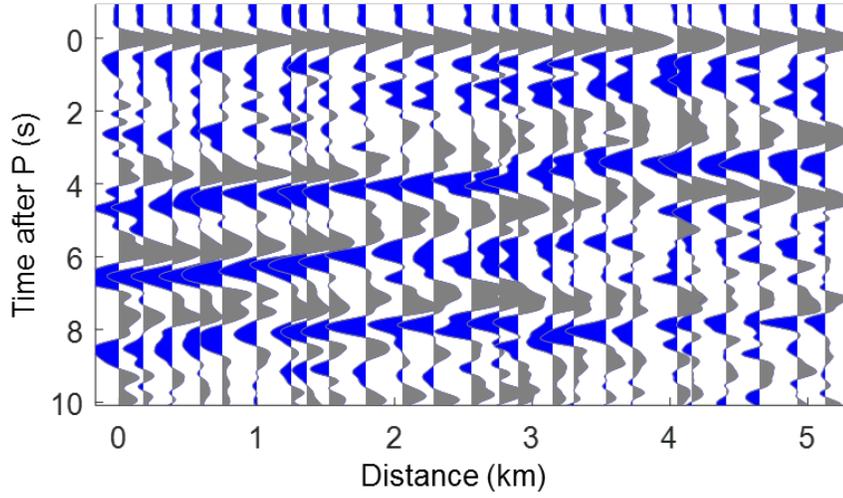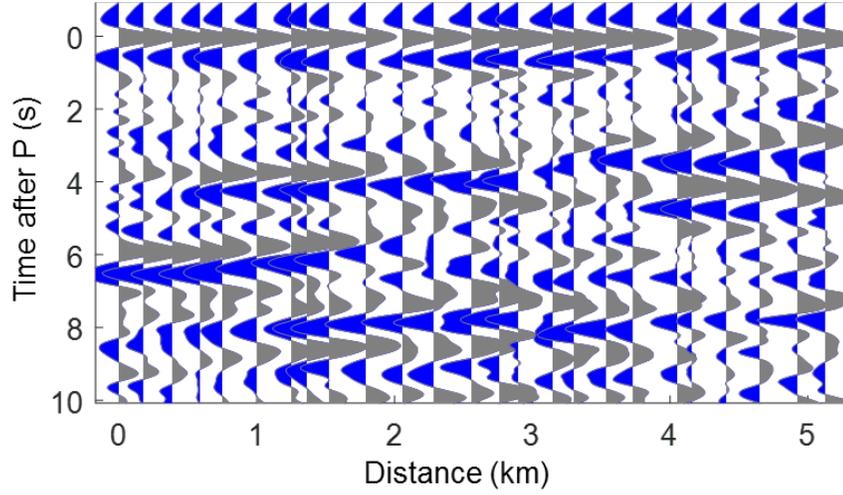
A. 0.1 – 0.5 Hz
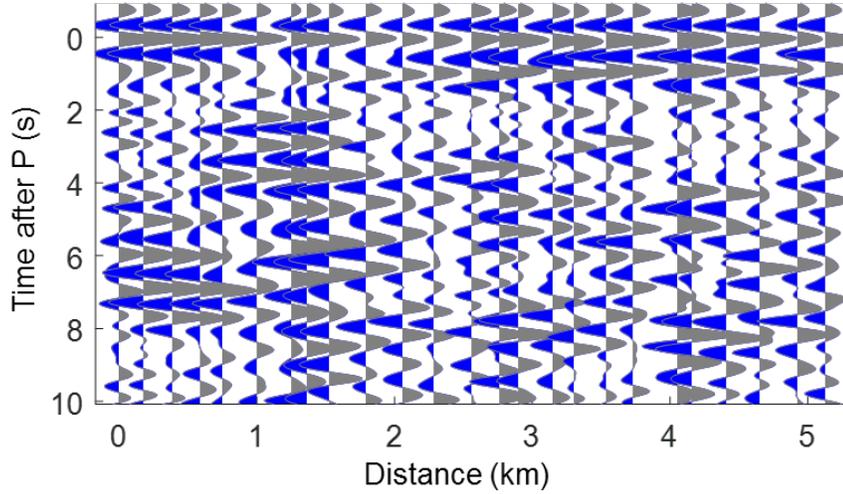
B. 0.5 – 1.0 Hz

C. 1.0 – 1.5 Hz

Powerline Line – Southeast frequency bins

D. 0.1 – 0.5 Hz
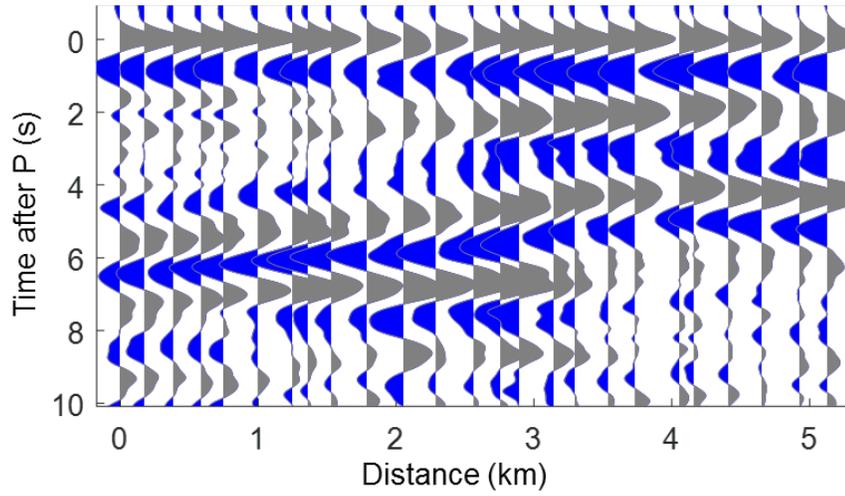
E. 0.5 – 1.0 Hz
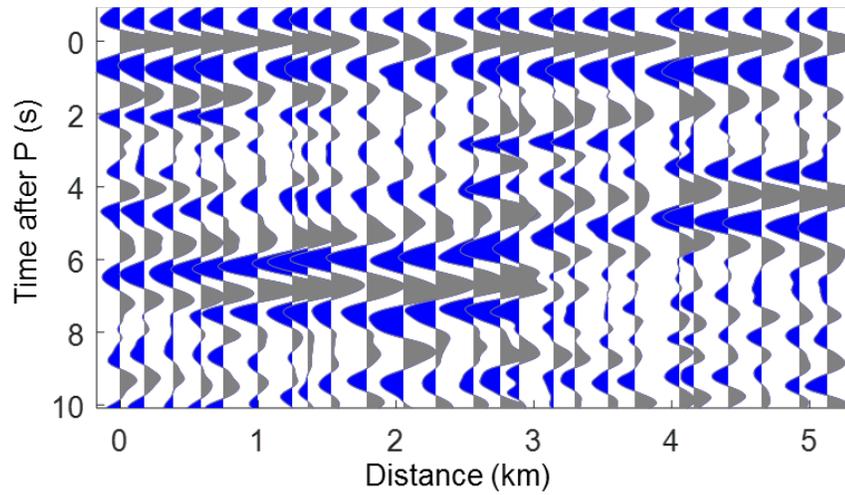
F. 1.0 – 1.5 Hz
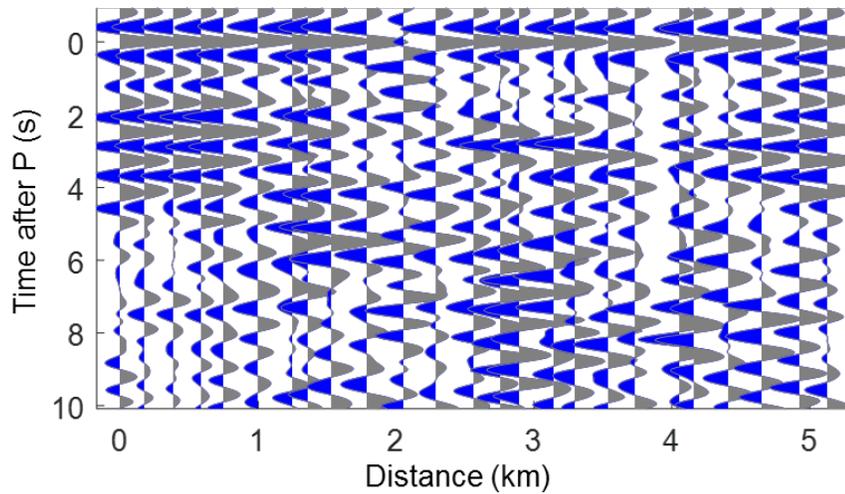
Figure 20: Powerline TVR profiles separated by azimuth and by frequency bin. Northwest events (A,B,C) are Russia and Japan. Southwest events (D,E,F) are both Colombia earthquakes and Argentina. Frequency bins only extend to 1.5 Hz due to signal-to-noise degradation at higher frequencies.
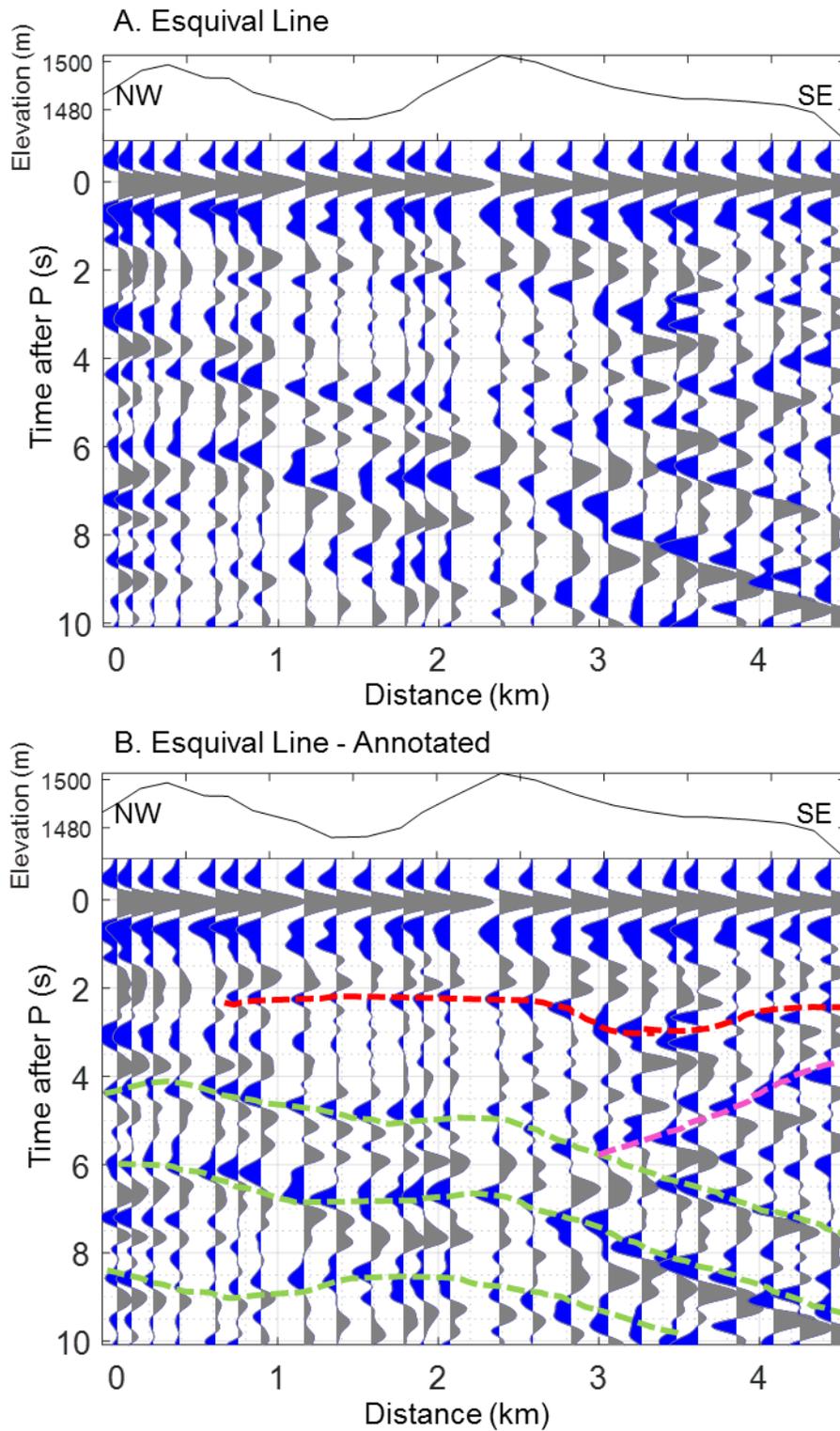
Figure 21: A. The Esquival line TVR profile overlain by corresponding topography. Time is shown to 10 seconds depth (~30 kilometers) to focus display depth of the intense series

of reflectors. Distance is from the northwesternmost trace. B. The same as A, but with annotated features discussed in the text.

Esquival Line – Northwest frequency bins
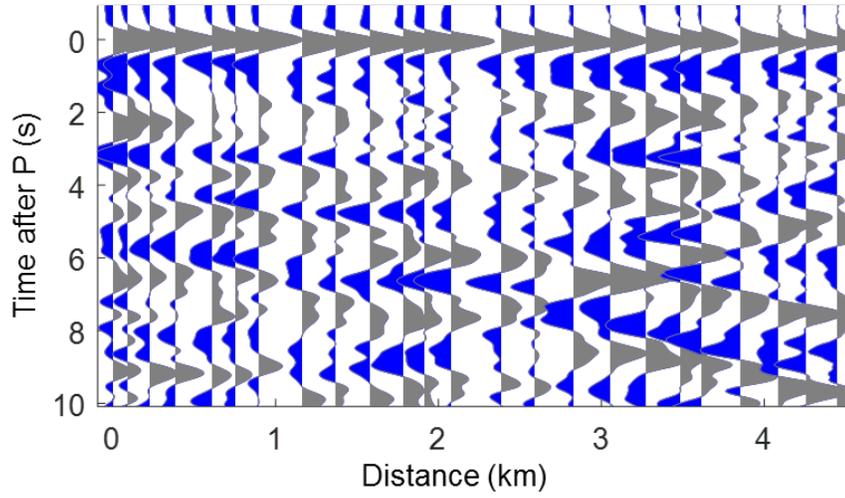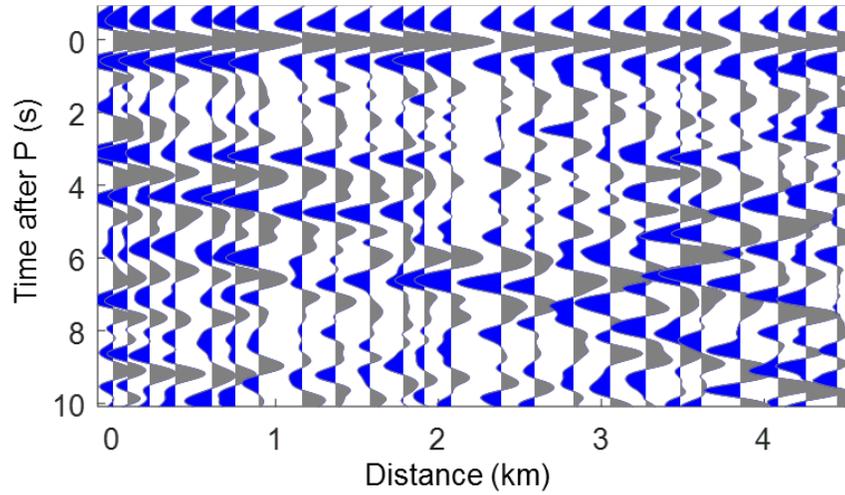
A. 0.1 – 0.5 Hz
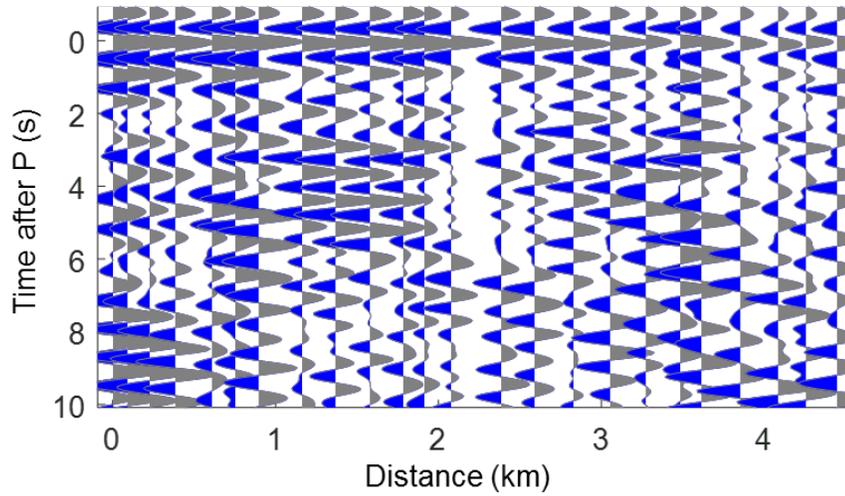
B. 0.5 – 1.0 Hz

C. 1.0 – 1.5 Hz

Esquival Line – Southeast frequency bins

D. 0.1 – 0.5 Hz
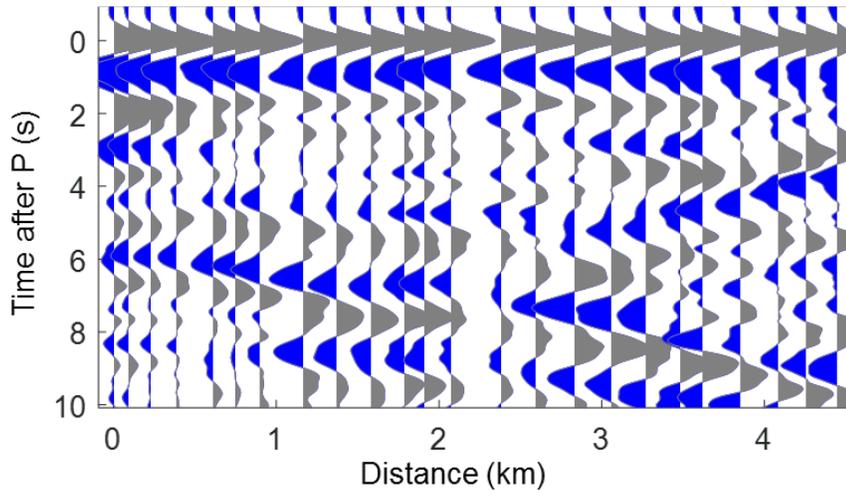
E. 0.5 – 1.0 Hz
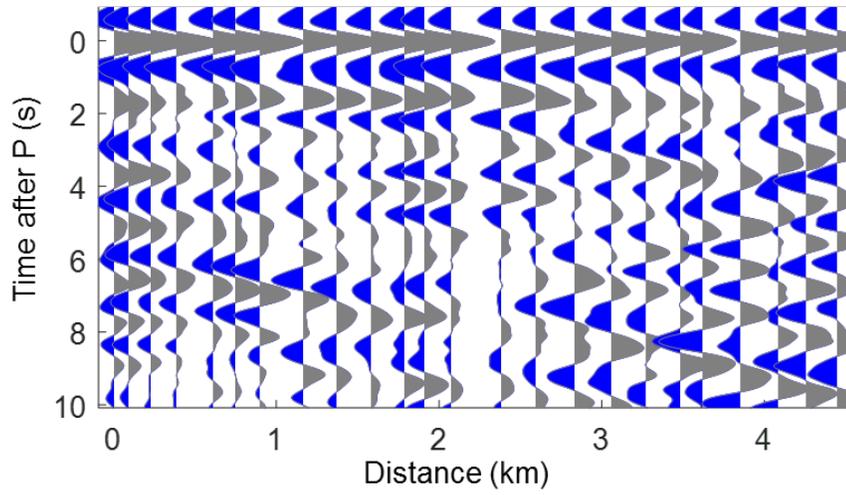
F. 1.0 – 1.5 Hz

Figure 22: Esquival TVR profile separated by azimuth and by frequency bin. Northwest events (A,B,C) are Russia and Japan. Southwest events (D,E,F) are both Colombia earthquakes and Argentina. Frequency bins only extend to 1.5 Hz due to signal-to-noise degradation at higher frequencies.
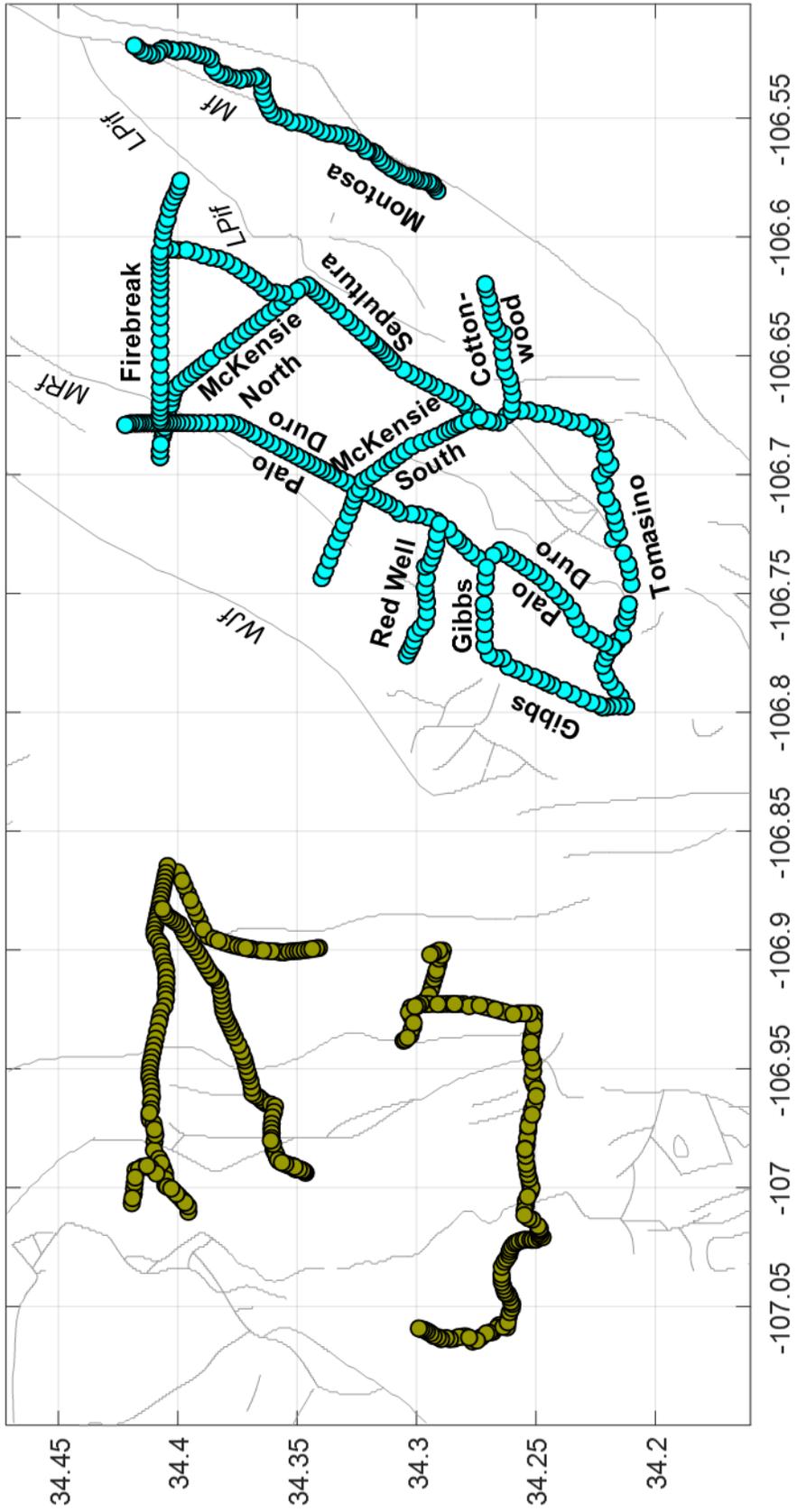
Figure 23: Map of the East half of the Sevilleta Array with profile lines highlighted in cyan and labelled. The relevant faults are labelled as follows: WJf – West Joyita fault, MRf – Military Road fault, LPif – Los Piños fault, Mf – Montosa fault.

A. Firebreak Line

B. Firebreak Line - Annotated
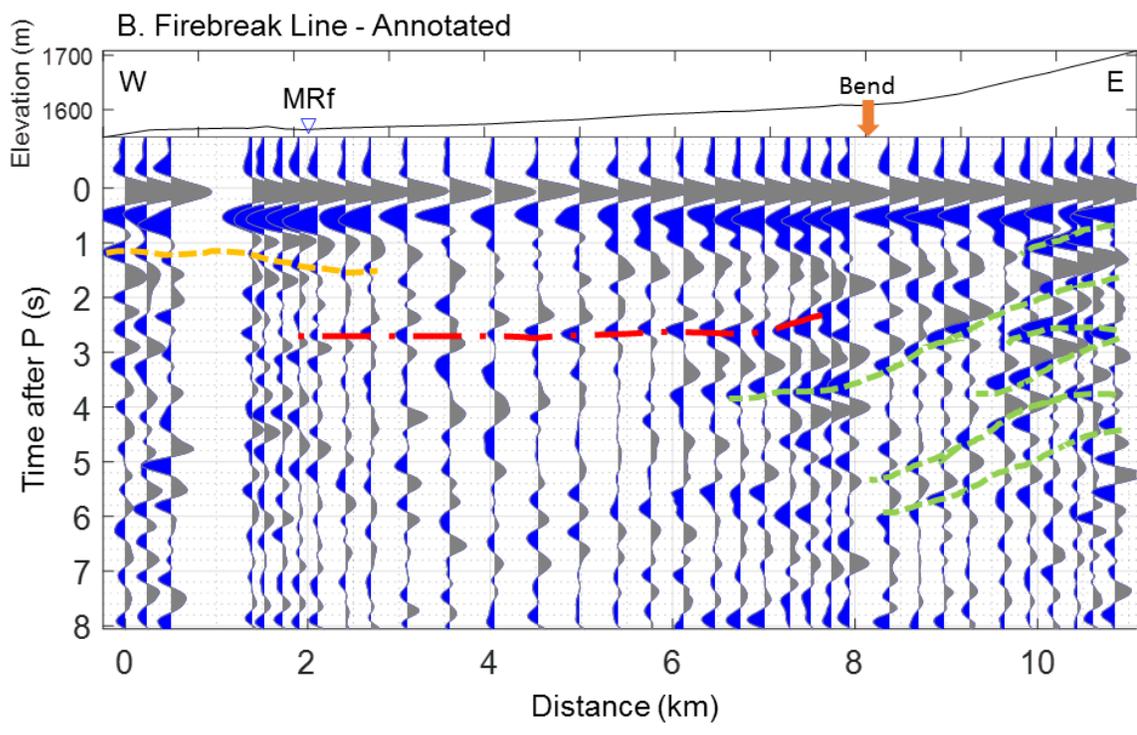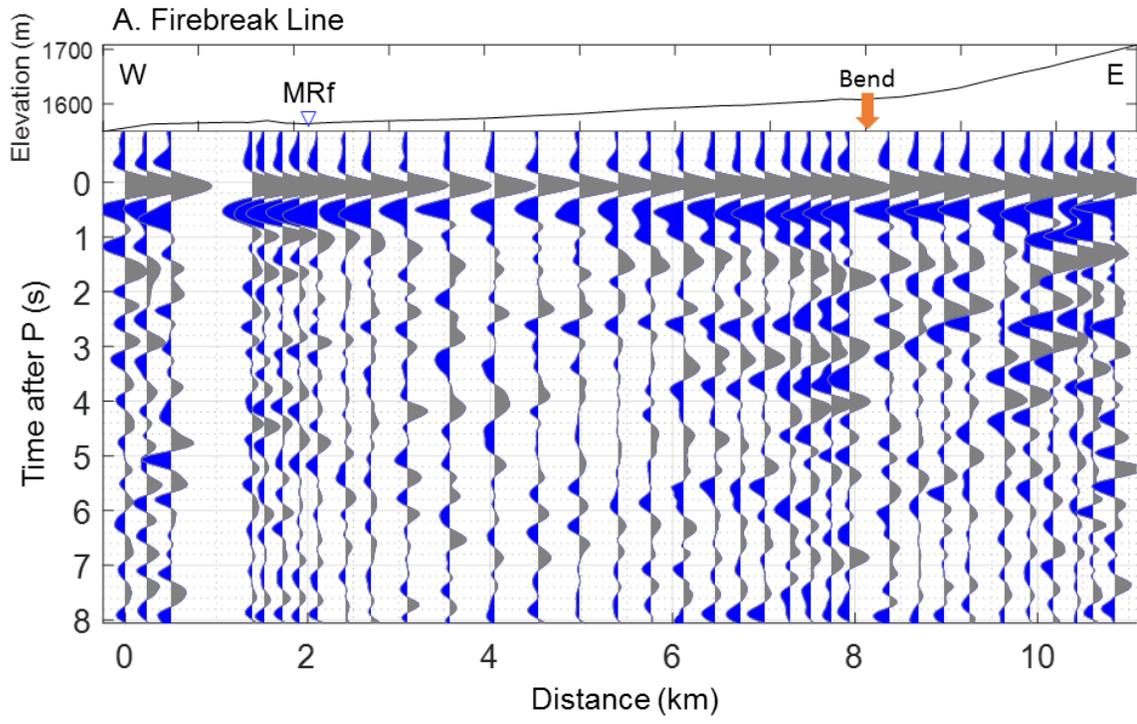
Figure 24: A. The Firebreak line TVR profile overlain by corresponding topography. Time is shown to 8 seconds depth (~25 kilometers) to display the depth of the eastern edge series of arrivals. Distance is from the westernmost trace. A bend in the line to the southeast is marked by an orange arrow. The Military Road fault is labeled as MRf. B. The same as A, but with annotated features discussed in the text.

Firebreak Line – Northwest frequency bins
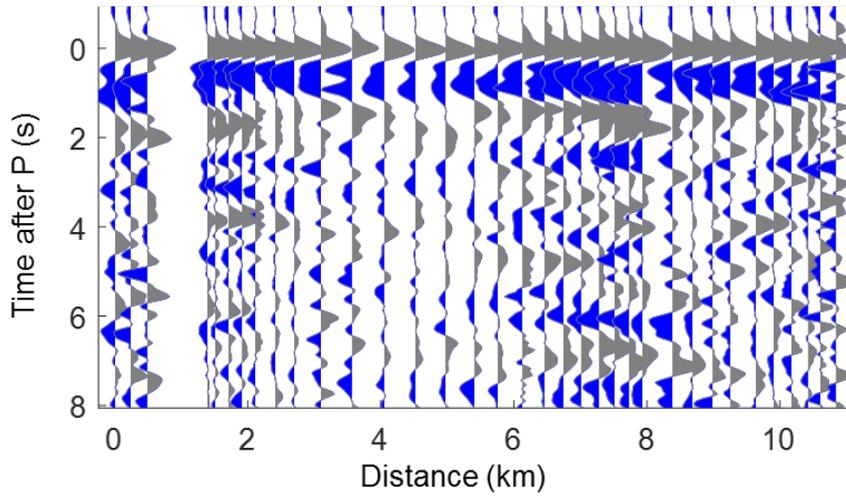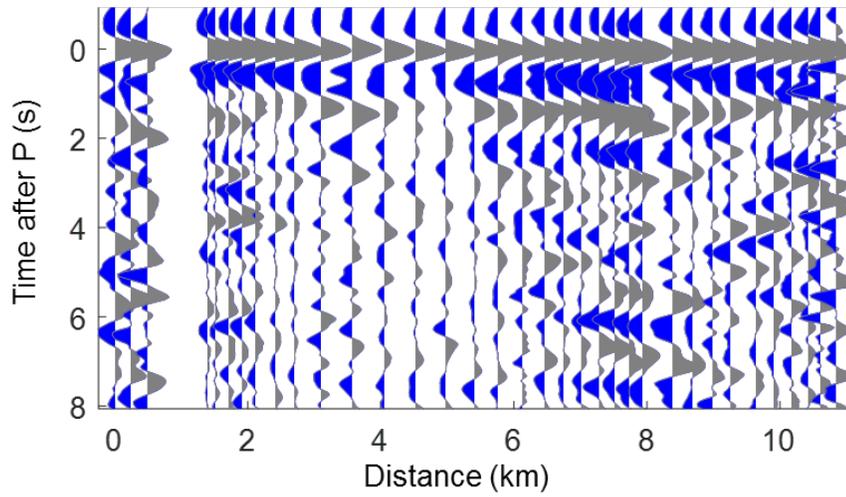
A. 0.1 – 0.5 Hz
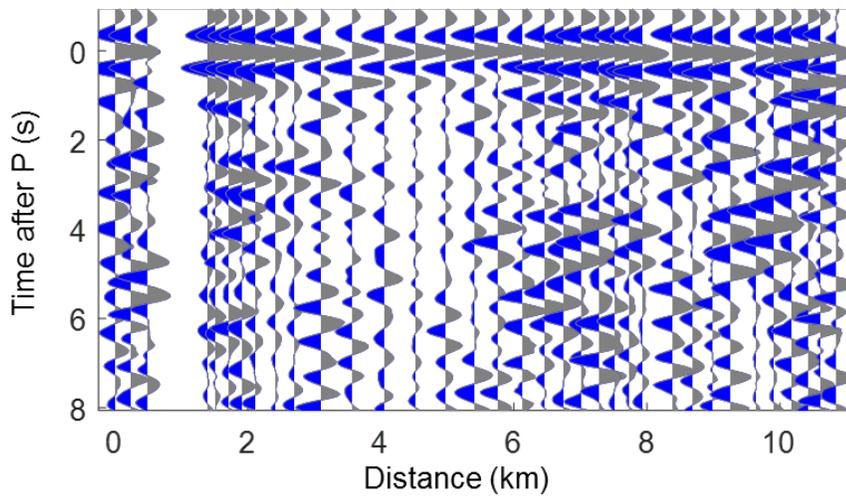
B. 0.5 – 1.0 Hz

C. 1.0 – 1.5 Hz

Firebreak Line – Southeast frequency bins

D. 0.1 – 0.5 Hz
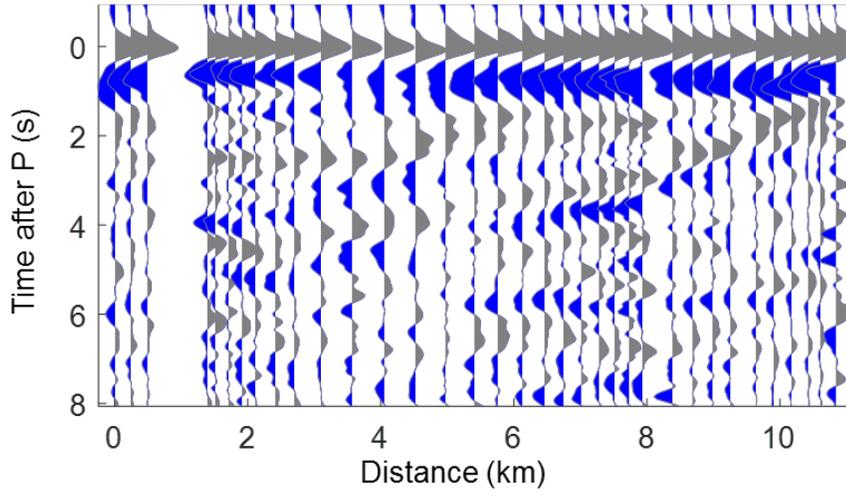
E. 0.5 – 1.0 Hz
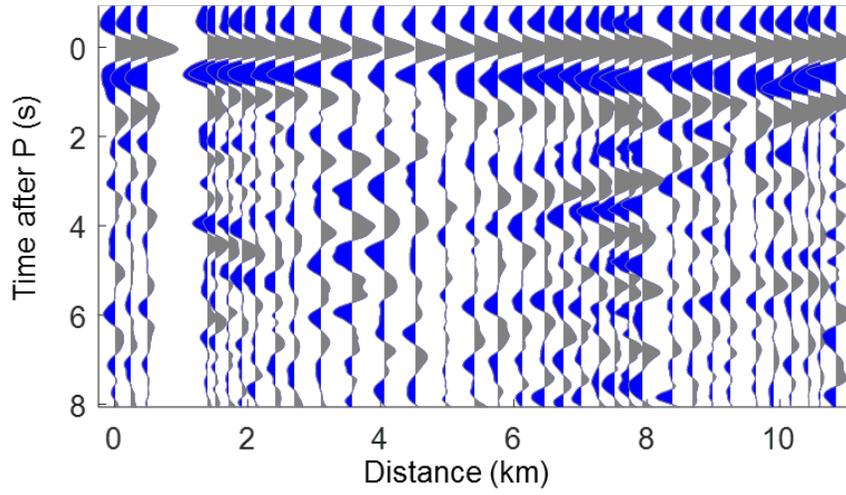
F. 1.0 – 1.5 Hz
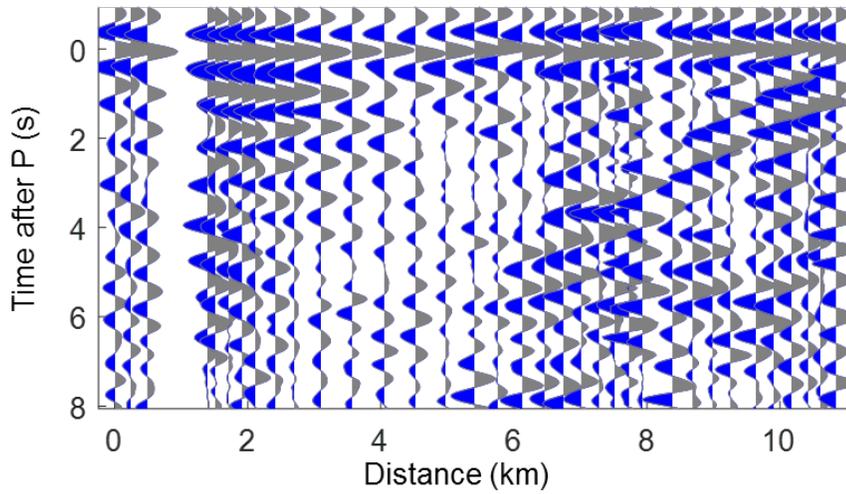
Figure 25: Firebreak TVR profile separated by azimuth and by frequency bin. Northwest events (A,B,C) are Russia and Japan. Southwest events (D,E,F) are both Colombia earthquakes and Argentina. Frequency bins only extend to 1.5 Hz due to signal-to-noise degradation at higher frequencies.

A. McKensie North Line

B. McKensie North Line - Annotated
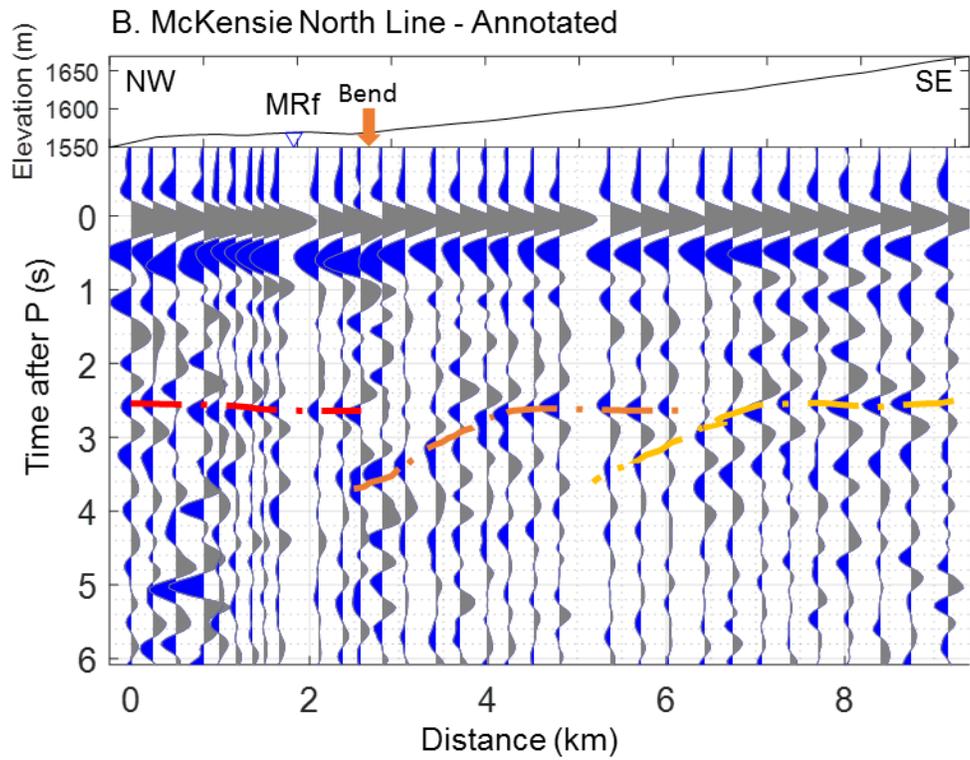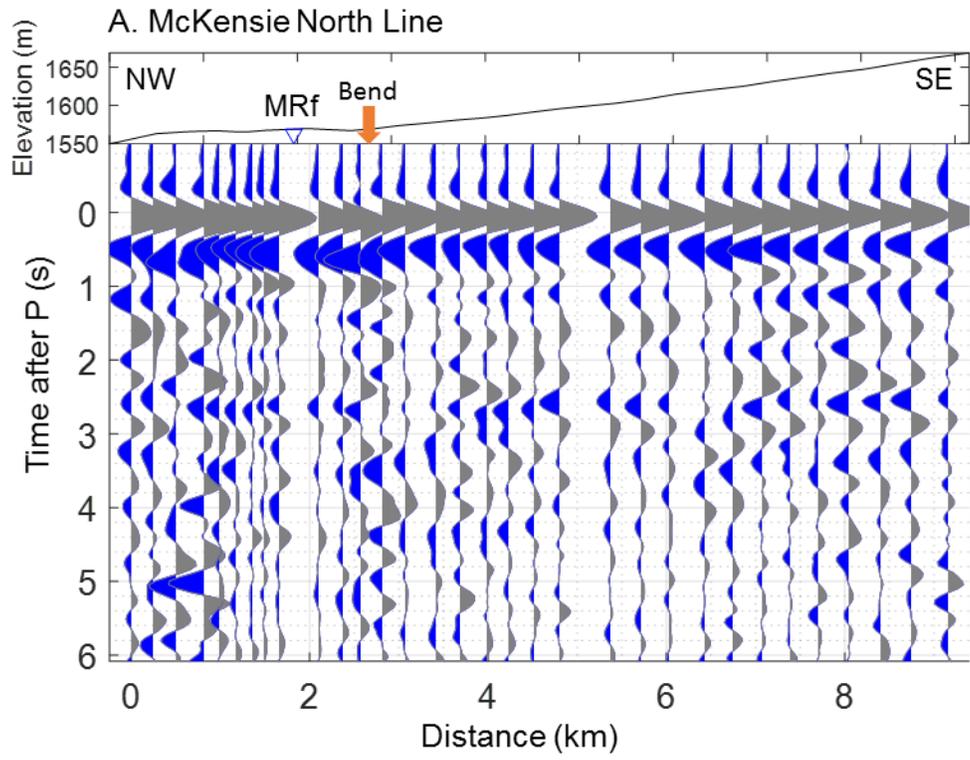
Figure 26: A. The McKensie North line TVR profile overlain by corresponding topography. Time is shown to 6 seconds depth (~20 kilometers) to focus on shallow crustal arrivals. Distance is from the northwesternmost trace. A more south-striking bend in the line is marked by an orange arrow. The Military Road fault is labeled as MRf. B. The same as A, but with annotated features discussed in the text.

McKensie North Line – Northwest frequency bins
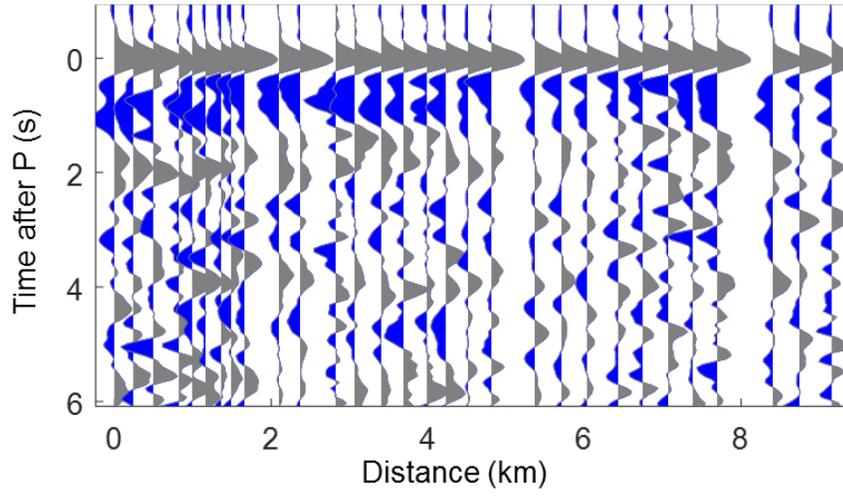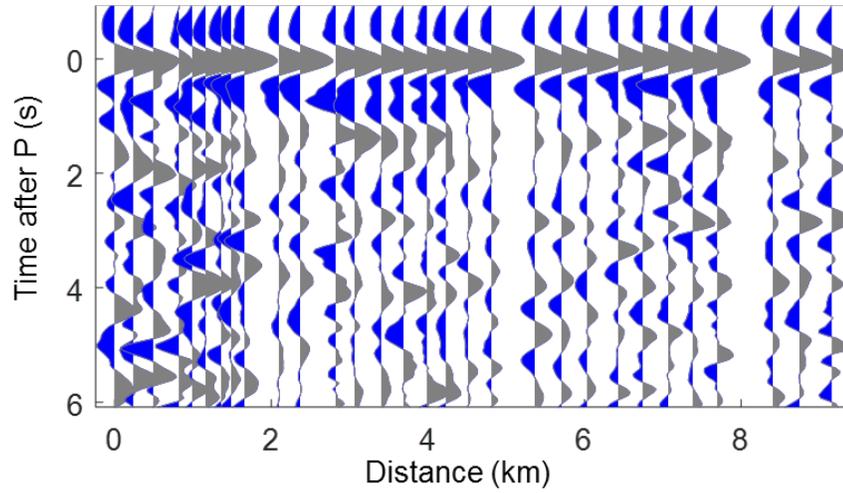
A. 0.1 – 0.5 Hz
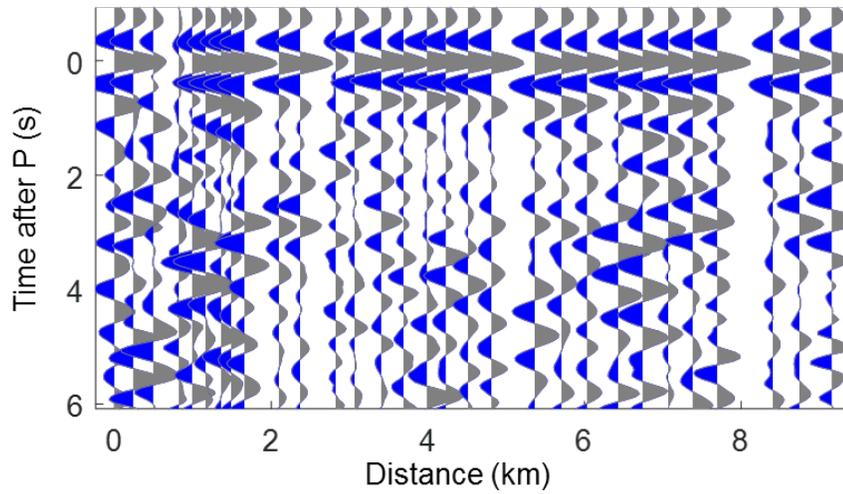
B. 0.5 – 1.0 Hz

C. 1.0 – 1.5 Hz

McKensie North Line – Southeast frequency bins

D. 0.1 – 0.5 Hz
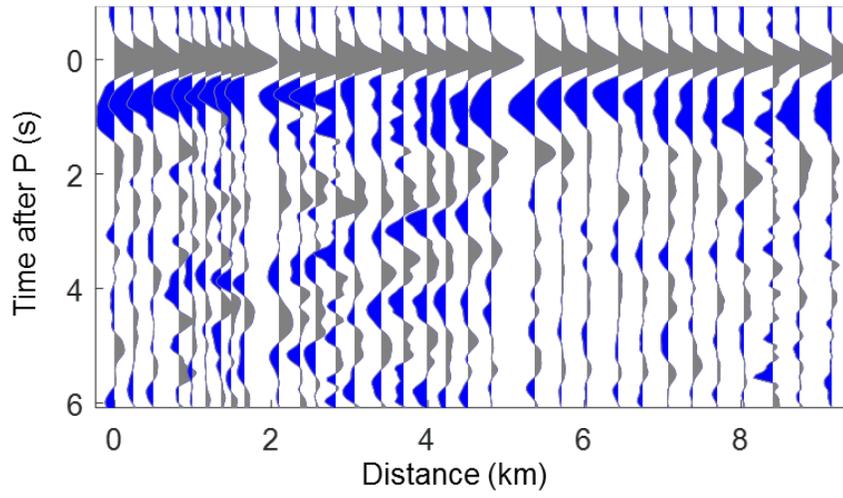
E. 0.5 – 1.0 Hz
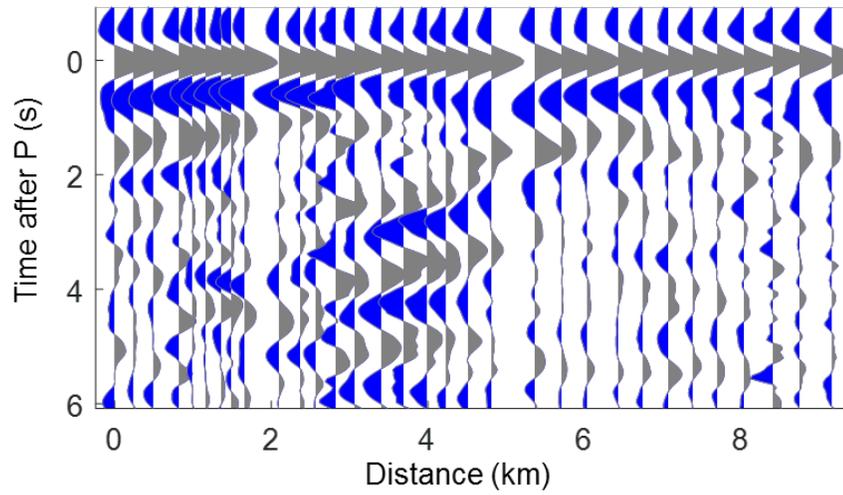
F. 1.0 – 1.5 Hz
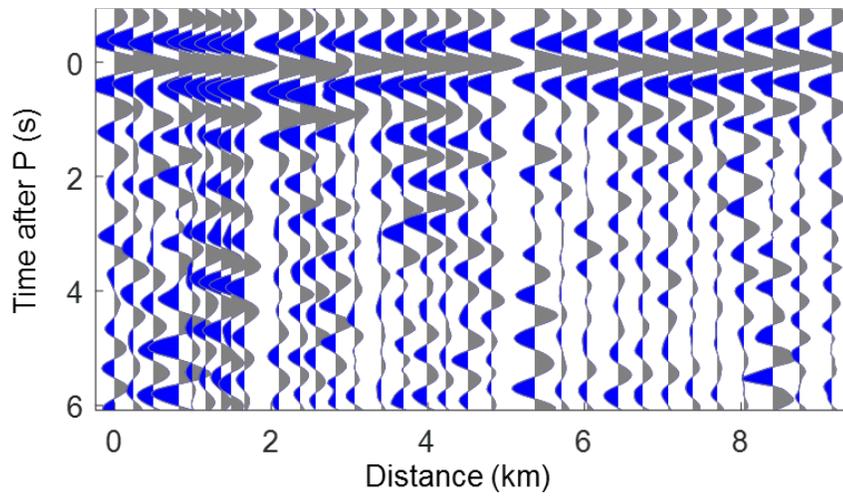
Figure 27: McKensie North TVR profile separated by azimuth and by frequency bin. Northwest events (A,B,C) are Russia and Japan. Southwest events (D,E,F) are both Colombia earthquakes and Argentina. Frequency bins only extend to 1.5 Hz due to signal-to-noise degradation at higher frequencies.

A. McKensie South Line – TVR Profile

B. McKensie South Line - Annotated

C. SE Earthquakes TVR Profile

D. NW Earthquakes TVR Profile
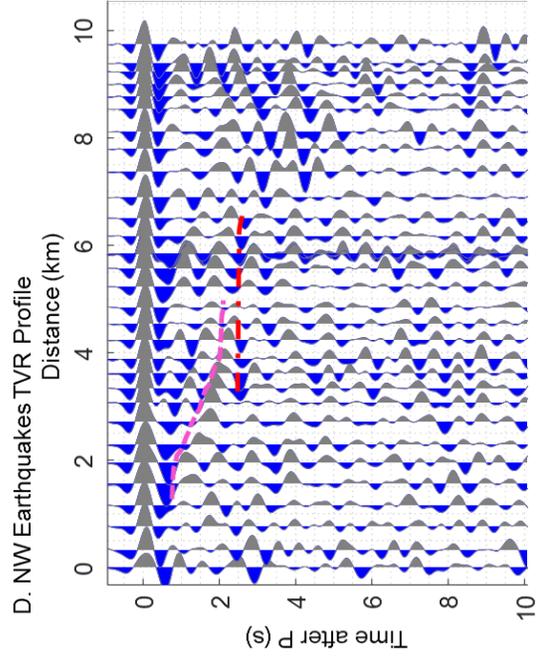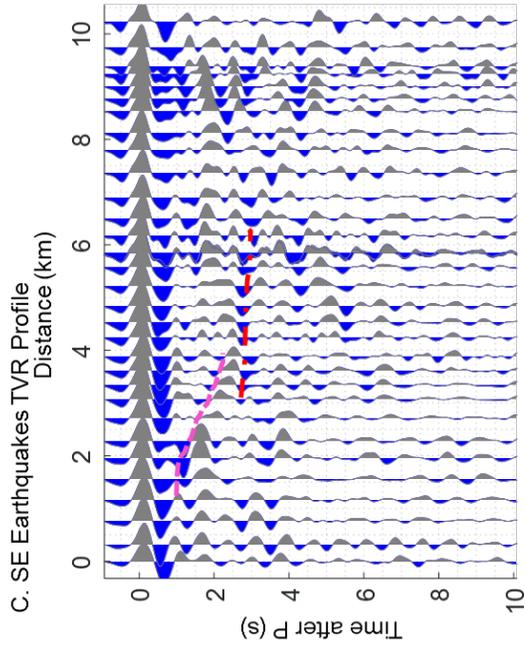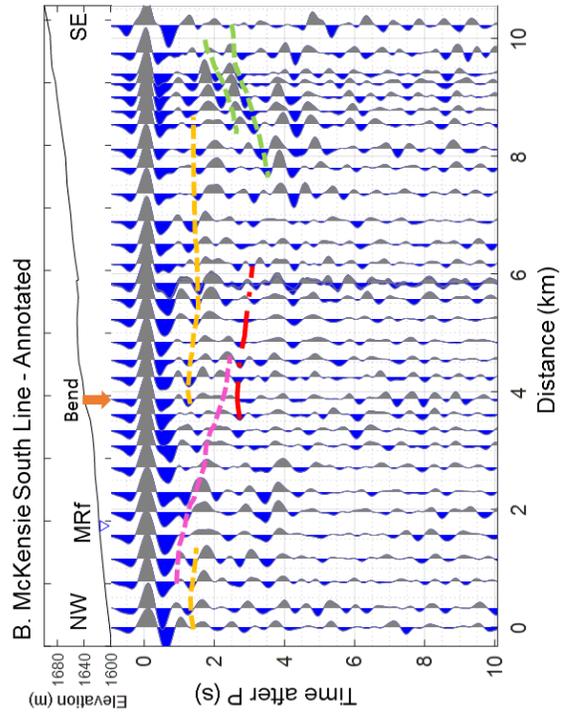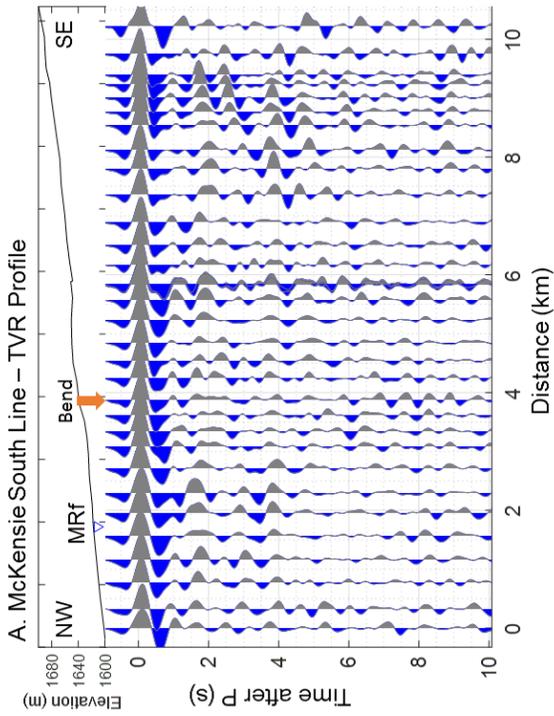
Figure 28: A. The McKensie South line TVR profile overlain by corresponding topography. Time is shown to 10 seconds depth (~30 kilometers) to allow better comparison with azimuthal TVR profiles in C and D. Distance is from the northwesternmost trace. A more south-striking bend in the line is marked by an orange arrow. The Military Road fault is labeled as MRf. B. The same as A, but with annotated features discussed in the text. C. TVR profile of the McKensie South line using the M5.1 an M5.5 from Colombia and the M6.7 from Argentina. Annotations show shared features with parts B and D. D. TVR profile of the McKensie South line using the M5.4 from Russia and the M5.5 from Japan. Annotations show shared features with B and C.

# McKensie South Line – Northwest frequency bins
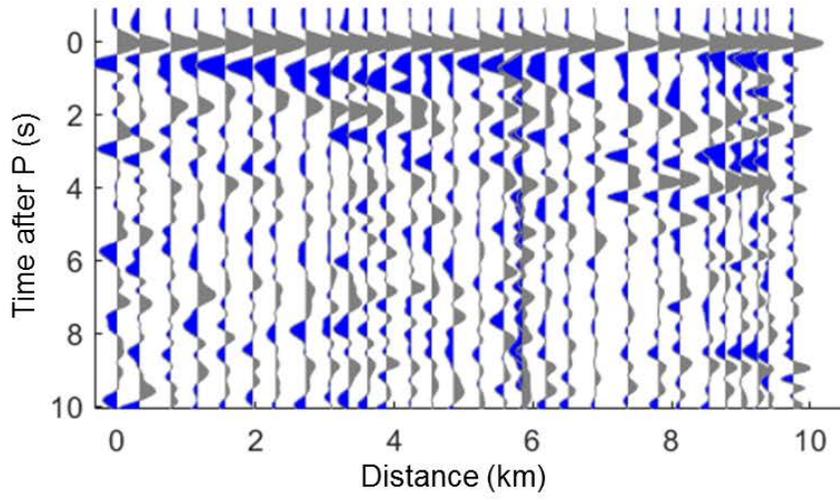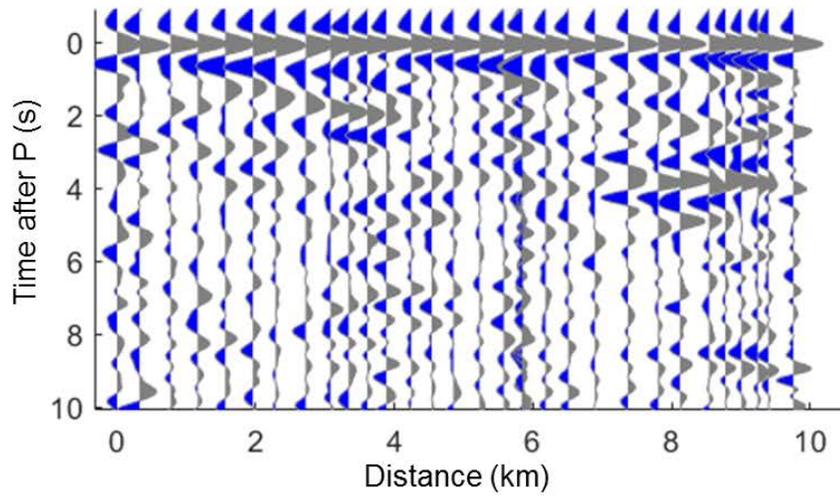
A. 0.1 – 0.5 Hz
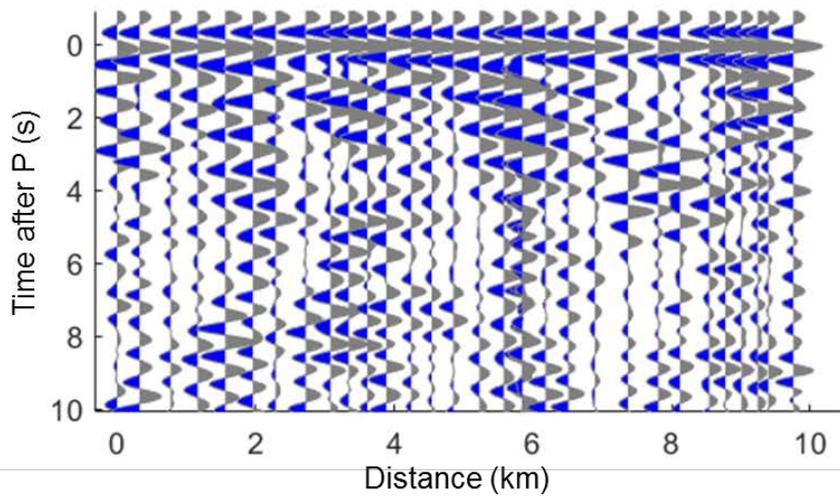
B. 0.5 – 1.0 Hz

C. 1.0 – 1.5 Hz

McKensie South Line – Southeast frequency bins

D. 0.1 – 0.5 Hz

E. 0.5 – 1.0 Hz

F. 1.0 – 1.5 Hz

118
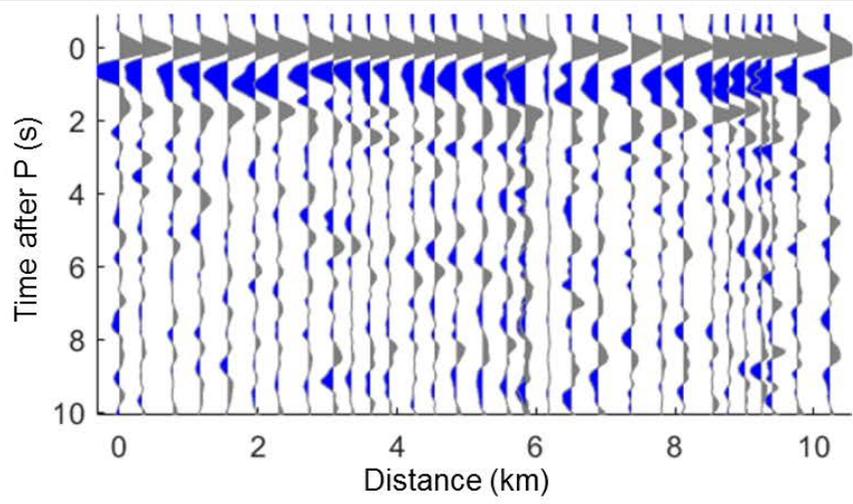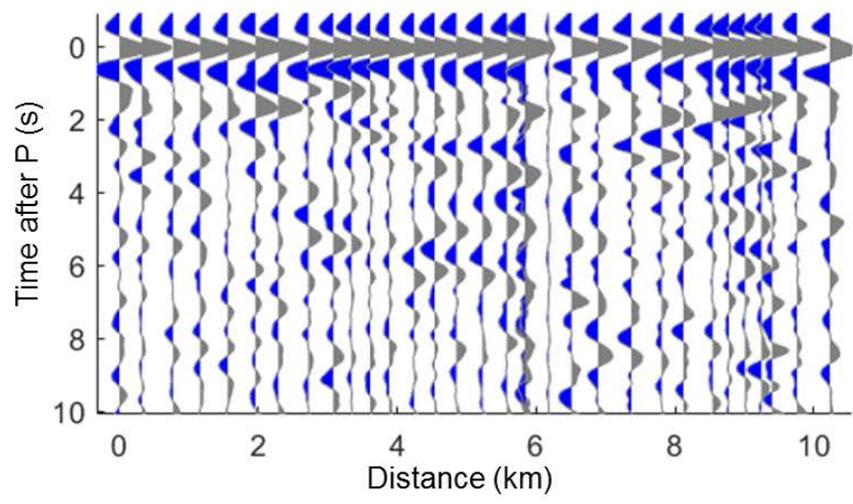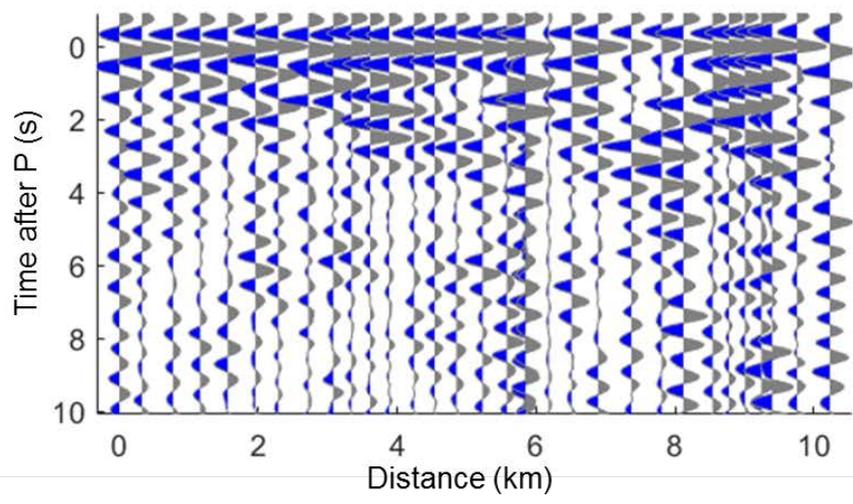
Figure 29: McKensie South TVR profile separated by azimuth and by frequency bin. Northwest events (A,B,C) are Russia and Japan. Southwest events (D,E,F) are both Colombia earthquakes and Argentina. Frequency bins only extend to 1.5 Hz due to signal-to-noise degradation at higher frequencies.
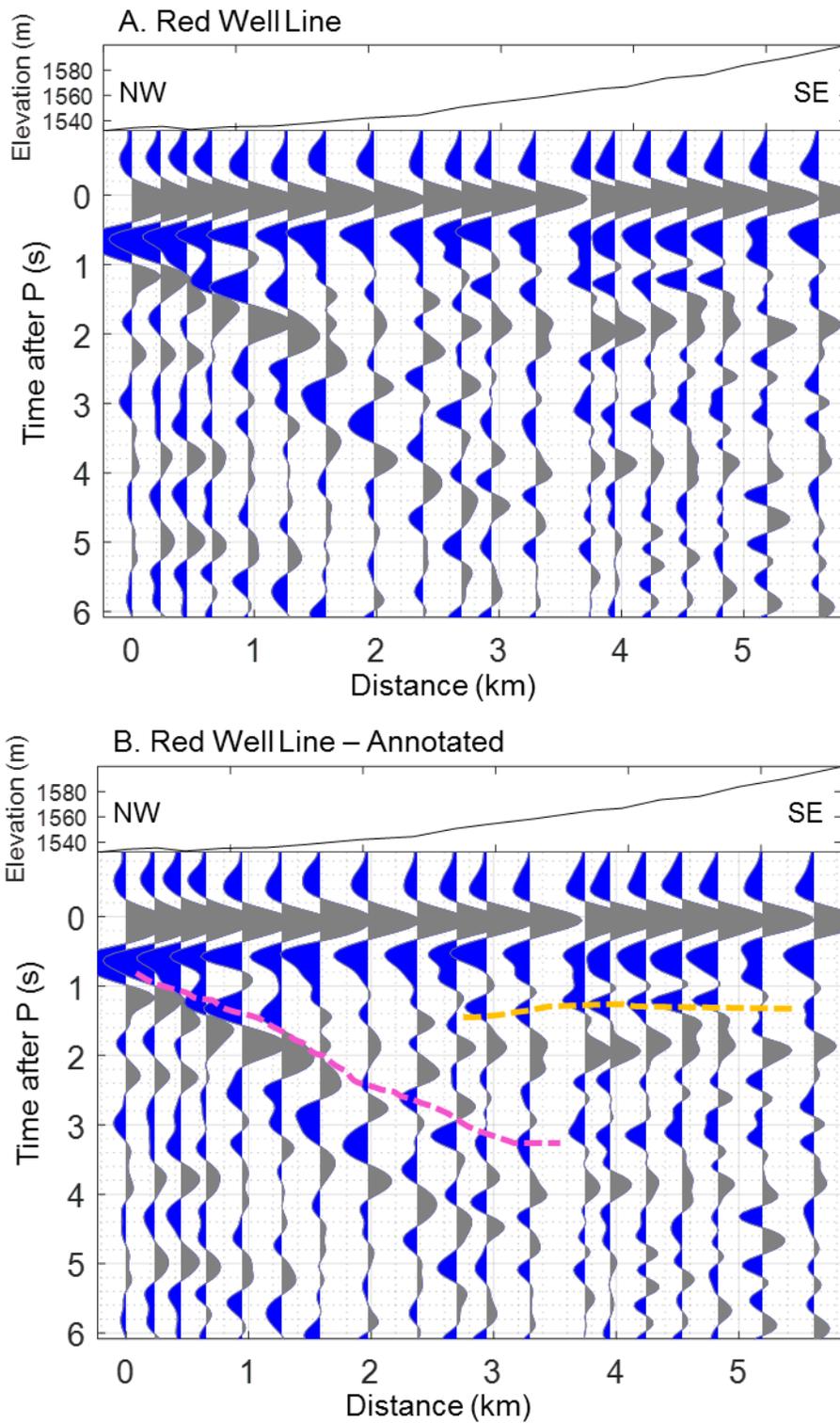
Figure 30: A. The Red Well line TVR profile overlain by corresponding topography.
Time is shown to 6 seconds depth (~20 kilometers) to focus on shallow crustal arrivals.

Distance is from the northwesternmost trace. B. The same as A, but with annotated features discussed in the text.

# Red Well Line – Northwest frequency bins
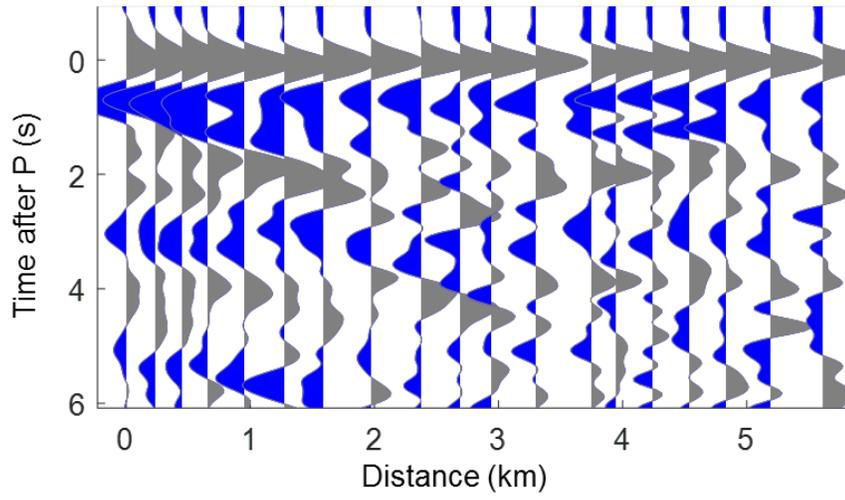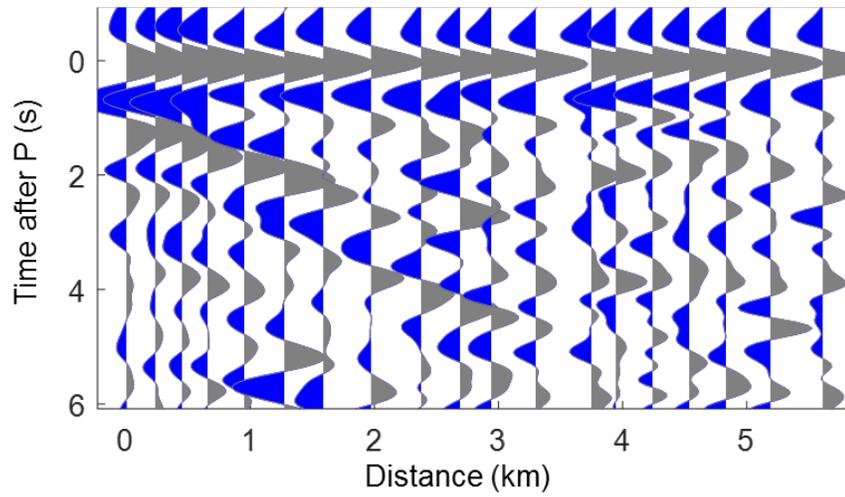
A. 0.1 – 0.5 Hz
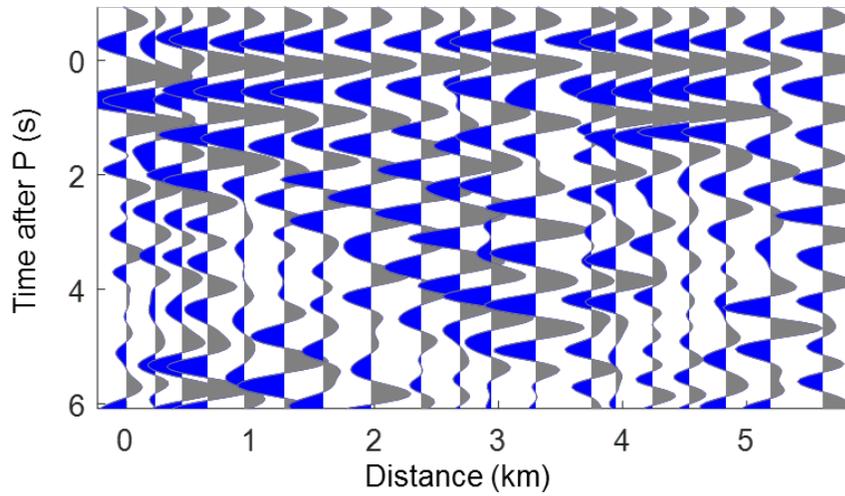
B. 0.5 – 1.0 Hz

C. 1.0 – 1.5 Hz

Red Well Line – Southeast frequency bins

D. 0.1 – 0.5 Hz
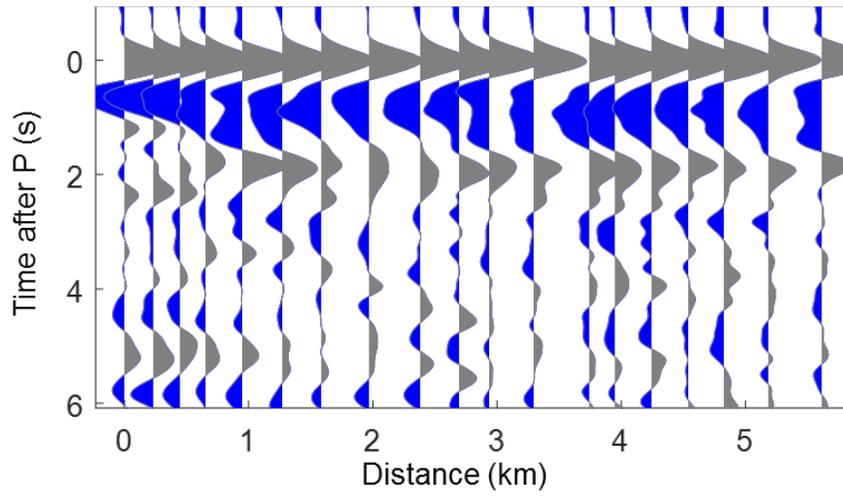
E. 0.5 – 1.0 Hz
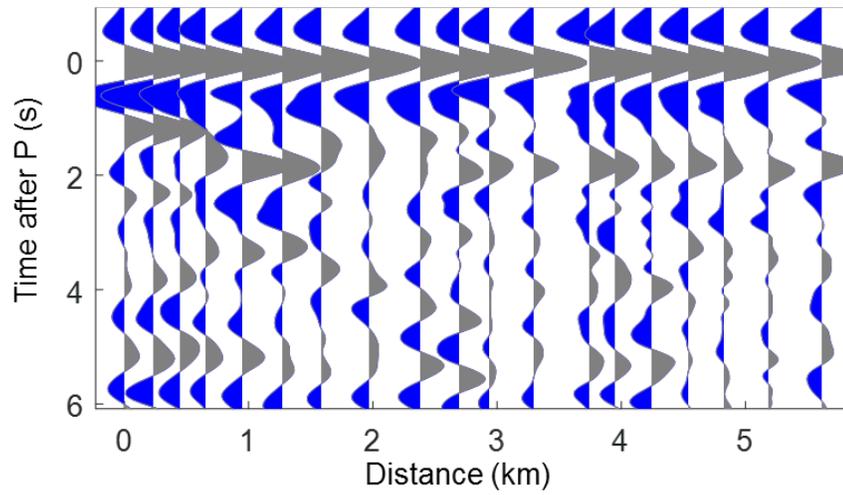
F. 1.0 – 1.5 Hz
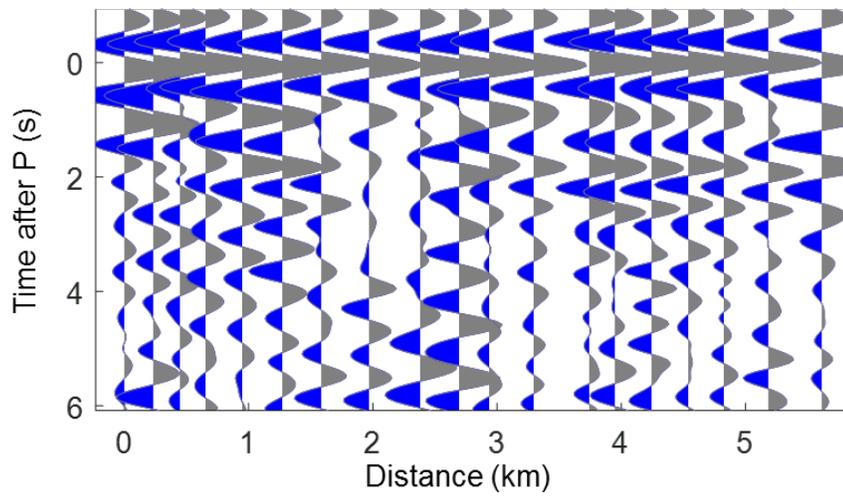
Figure 31: Red Well TVR profile separated by azimuth and by frequency bin. Northwest events (A,B,C) are Russia and Japan. Southwest events (D,E,F) are both Colombia earthquakes and Argentina. Frequency bins only extend to 1.5 Hz due to signal-to-noise degradation at higher frequencies.

A. Palo Duro Line

B. Palo Duro Line – Annotated
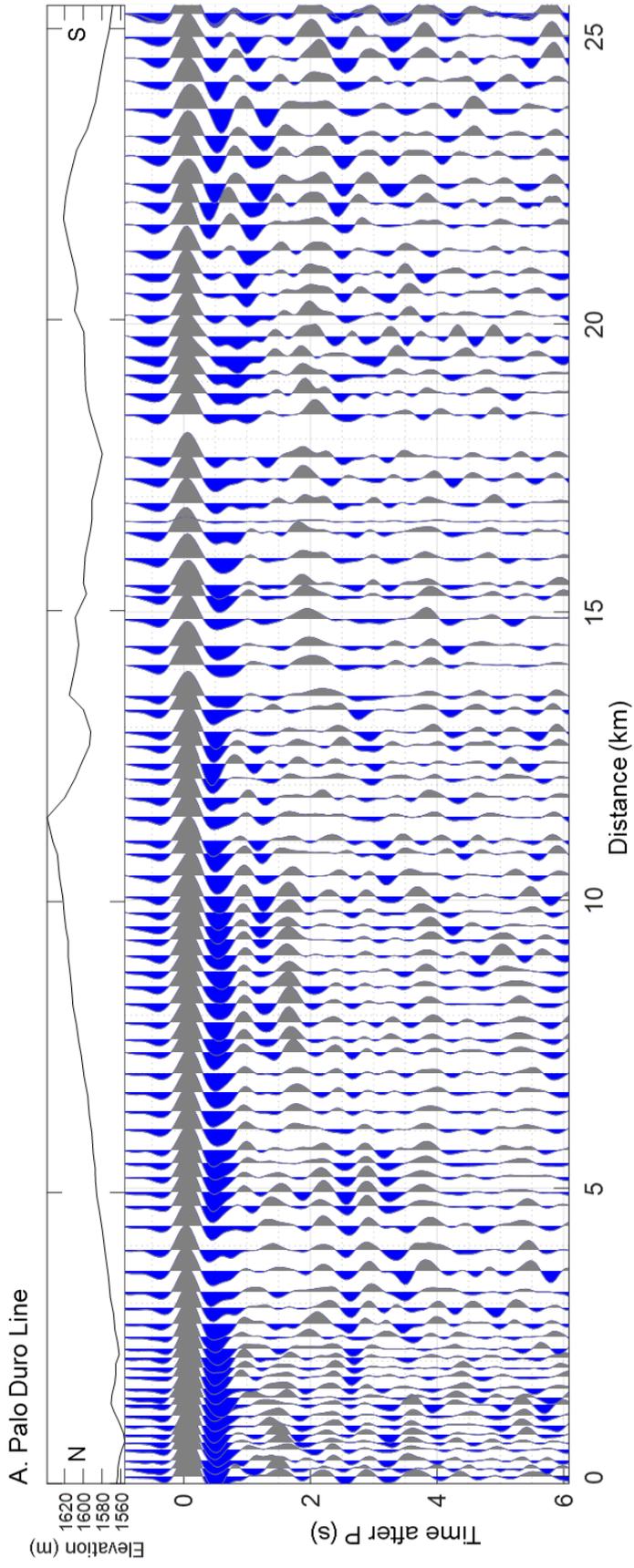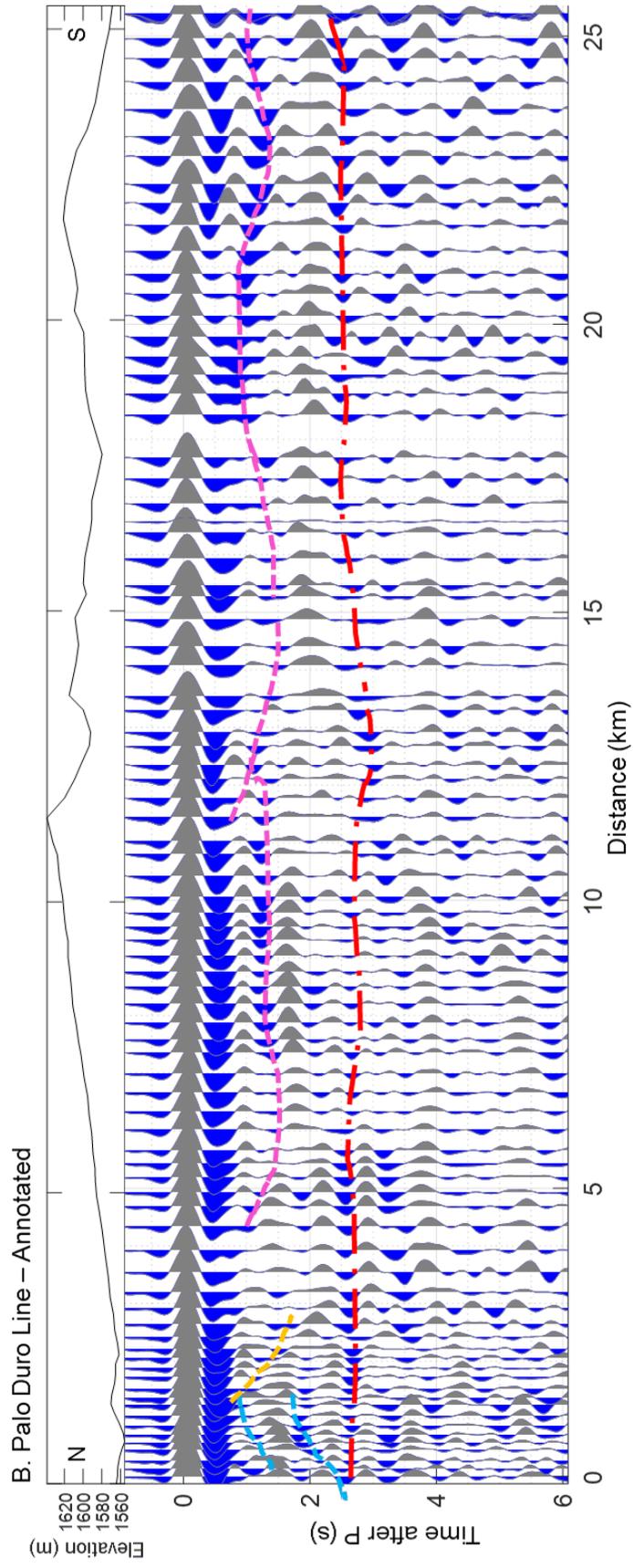
Figure 32: A. The Palo Duro line TVR profile overlain by corresponding topography. Time is shown to 6 seconds depth (~20 kilometers) to focus on shallow crustal arrivals. Distance is from the northernmost trace. B. The same as A, but with annotated features discussed in the text.

Palo duro Line – Northwest frequency bins
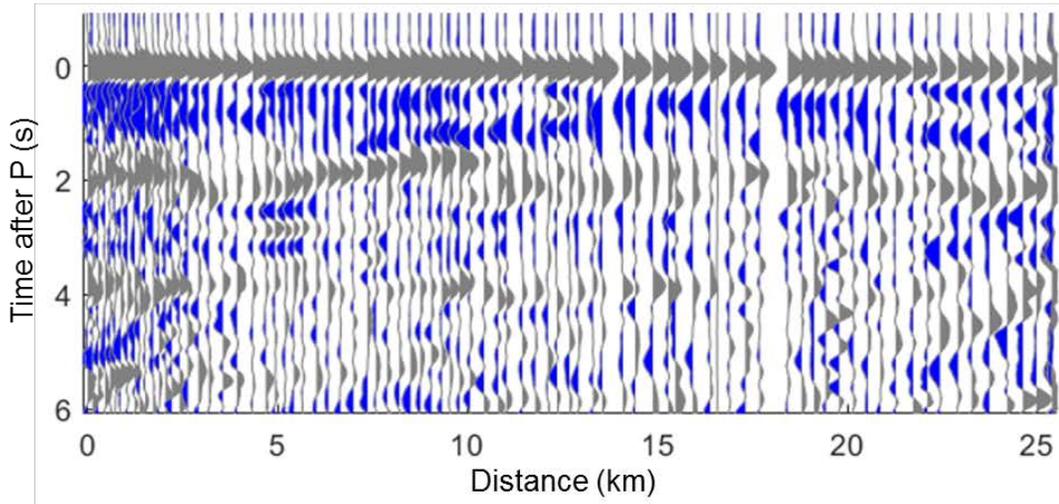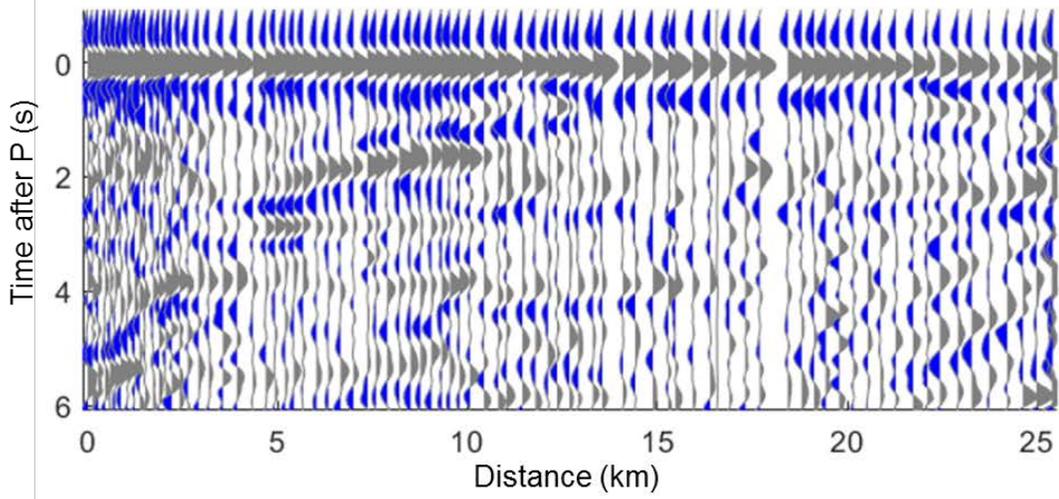
A. 0.1 – 0.5 Hz
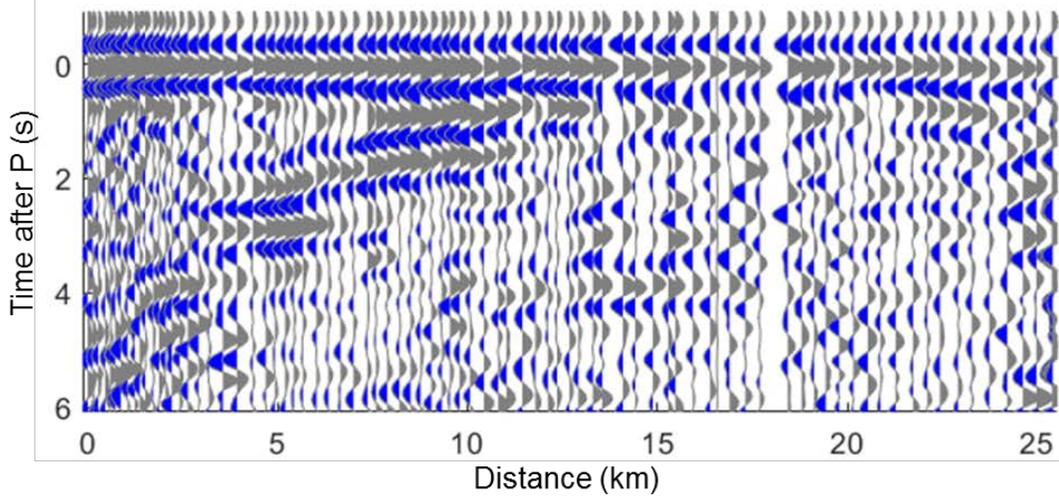
B. 0.5 – 1.0 Hz

C. 1.0 – 1.5 Hz

Palo duro Line – Southeast frequency bins

D. 0.1 – 0.5 Hz


E. 0.5 – 1.0 Hz

F. 1.0 – 1.5 Hz

129
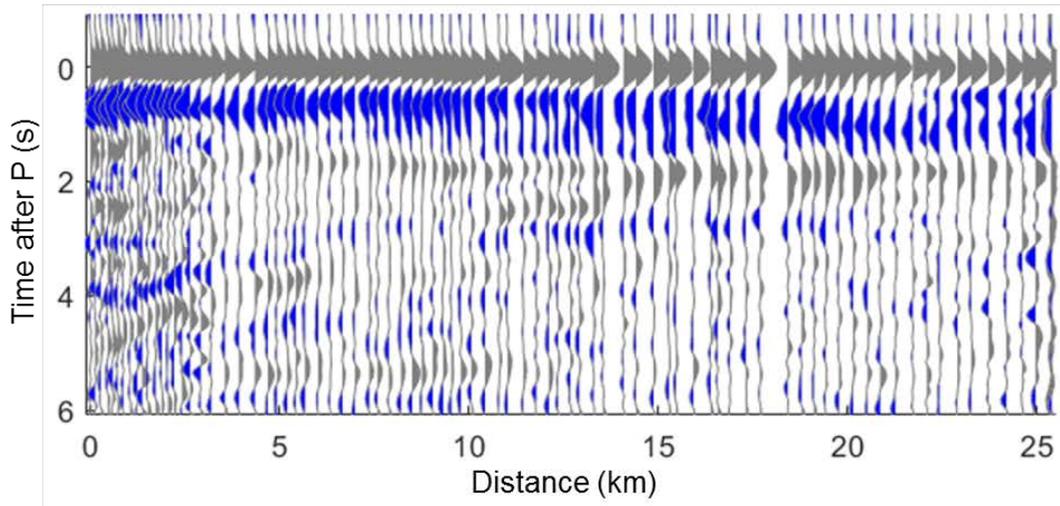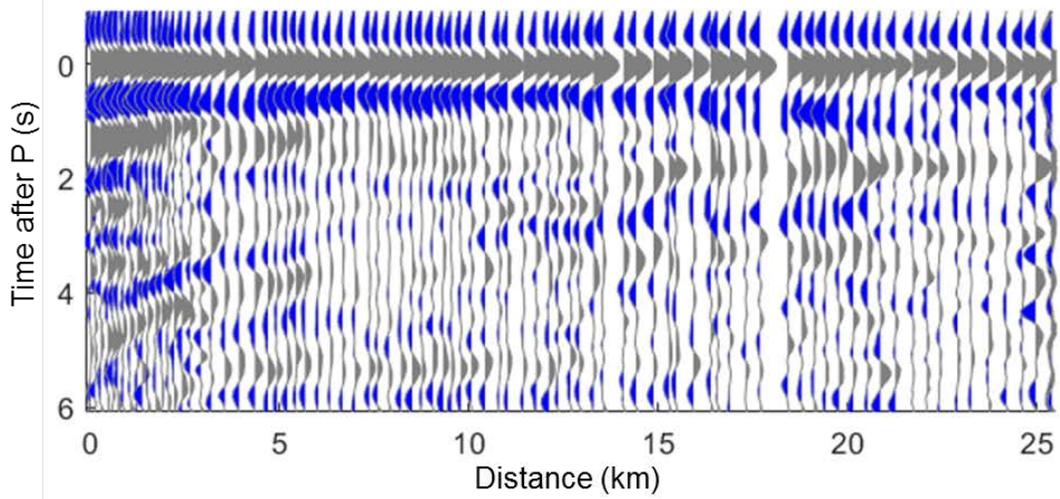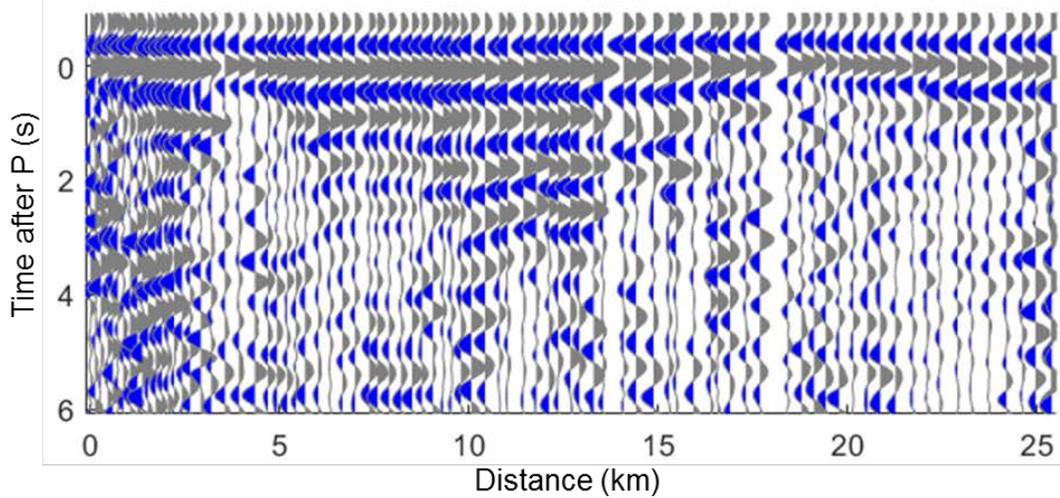
Figure 33: Palo Duro TVR profile separated by azimuth and by frequency bin. Northwest events (A,B,C) are Russia and Japan. Southwest events (D,E,F) are both Colombia earthquakes and Argentina. Frequency bins only extend to 1.5 Hz due to signal-to-noise degradation at higher frequencies.

A. Gibbs Line

B. Gibbs Line – Annotated
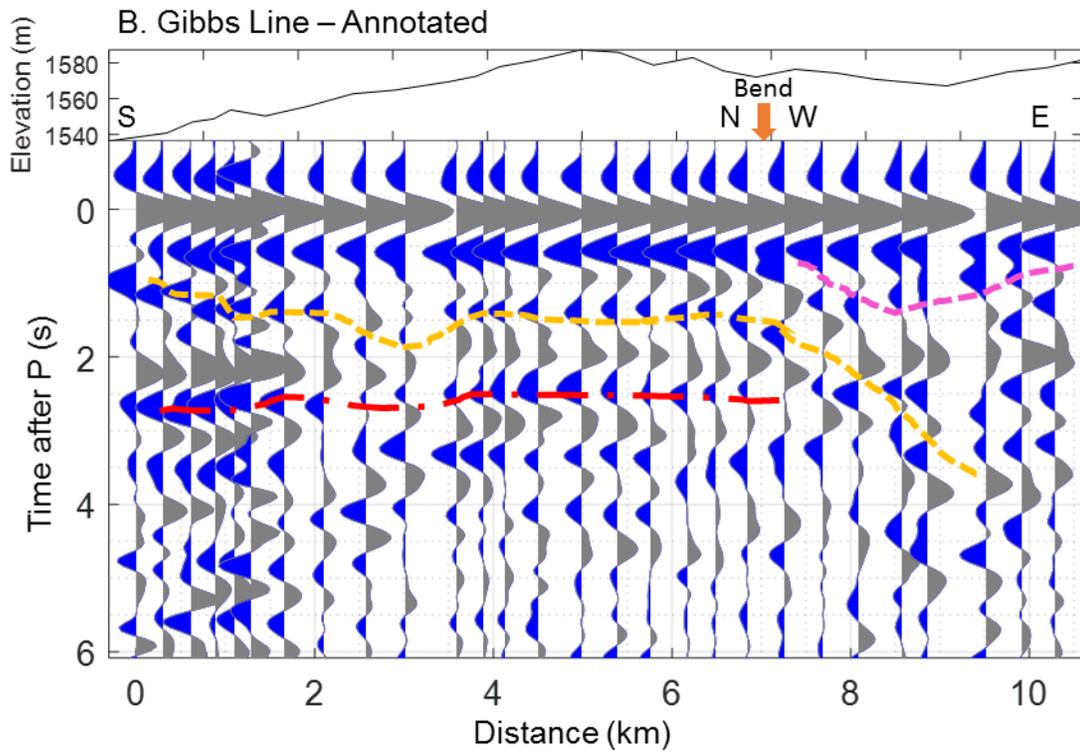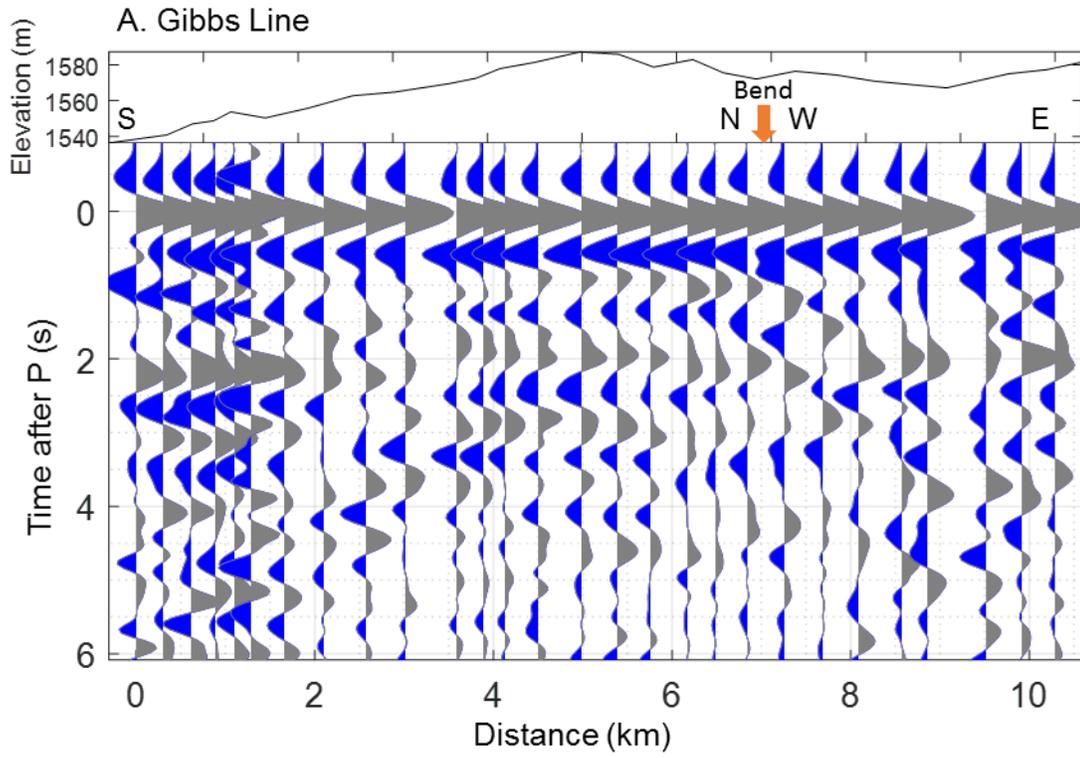
Figure 34: A. The Gibbs line TVR profile overlain by corresponding topography. Time is shown to 6 seconds depth (~20 kilometers) to focus on shallow crustal arrivals. Distance is from the southernmost trace. A bend in the line turning east is marked by an orange arrow. B. The same as A, but with annotated features discussed in the text.

Gibbs Line – Northwest frequency bins
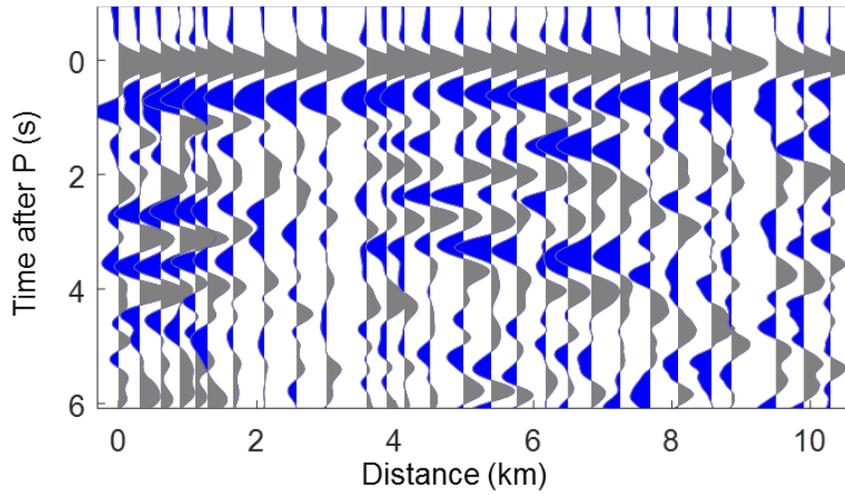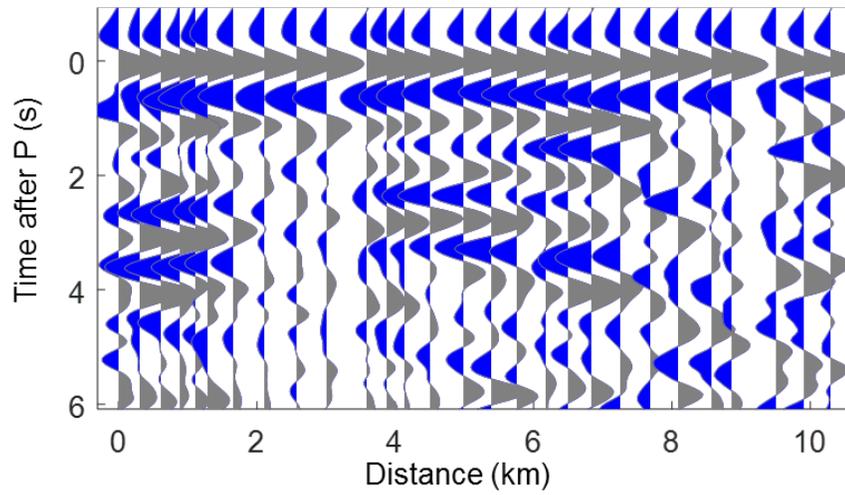
A. 0.1 – 0.5 Hz
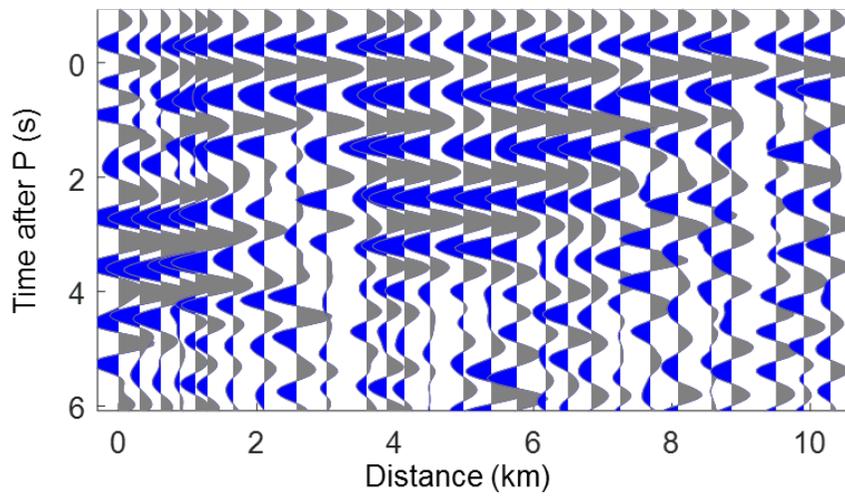
B. 0.5 – 1.0 Hz

C. 1.0 – 1.5 Hz

Gibbs Line – Southeast frequency bins

D. 0.1 – 0.5 Hz
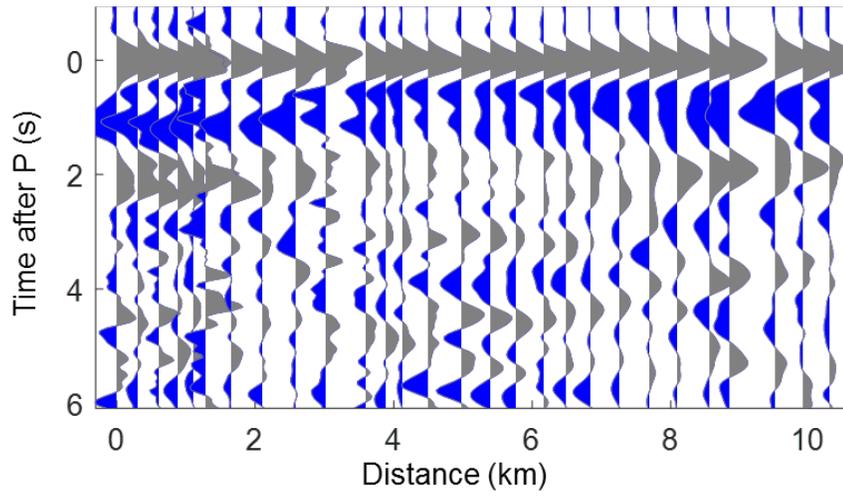
E. 0.5 – 1.0 Hz
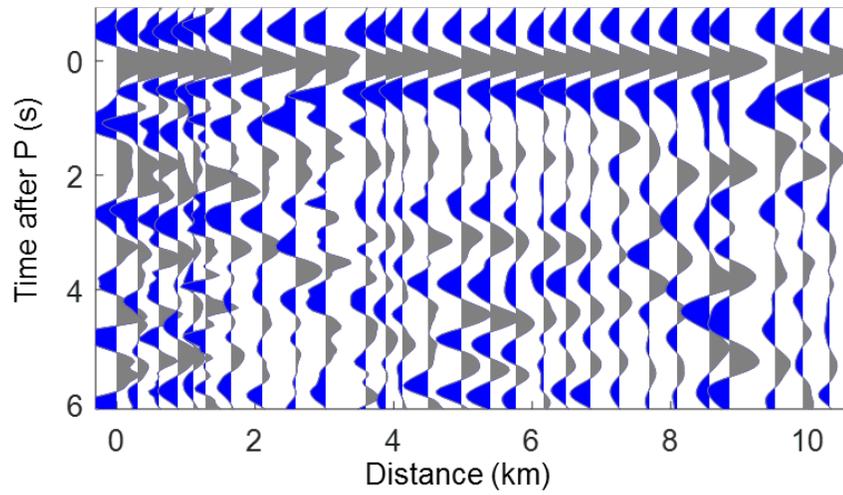
F. 1.0 – 1.5 Hz
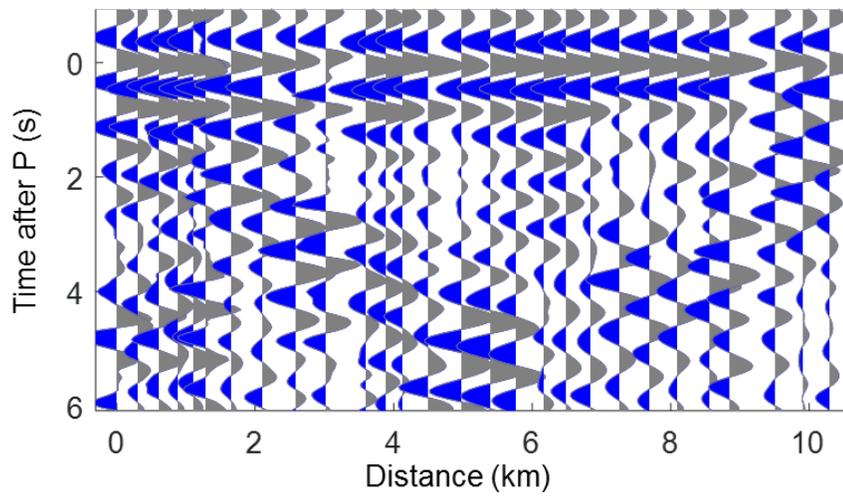
Figure 35: Gibbs TVR profile separated by azimuth and by frequency bin. Northwest events (A,B,C) are Russia and Japan. Southwest events (D,E,F) are both Colombia earthquakes and Argentina. Frequency bins only extend to 1.5 Hz due to signal-to-noise degradation at higher frequencies.

A. Tomasino Line

B. Tomasino Line – Annotated
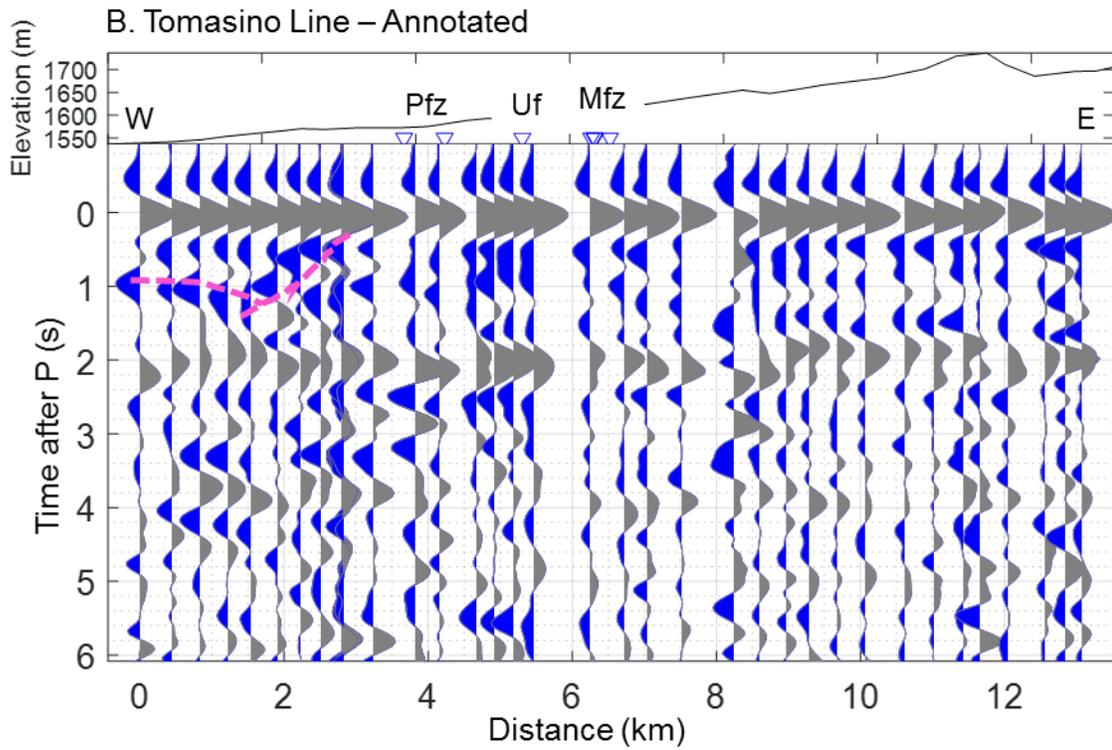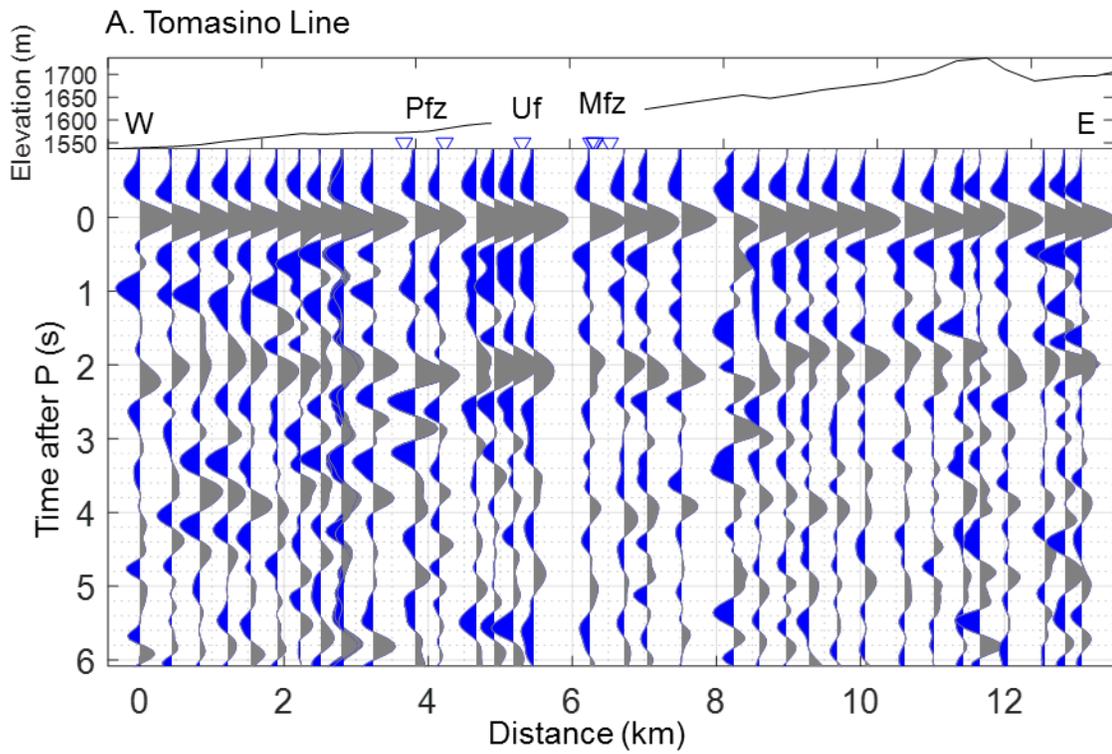
Figure 36: A. The Tomasino line TVR profile overlain by corresponding topography. Time is shown to 6 seconds depth (~20 kilometers) to focus on shallow crustal arrivals. Distance is from the westernmost trace. Faults are labelled as follows: Pfz – Parida fault zone, Uf – Unnamed fault, Mfz – Montosa fault zone. B. The same as A, but with annotated features discussed in the text.

Tomasino Line – Northwest frequency bins
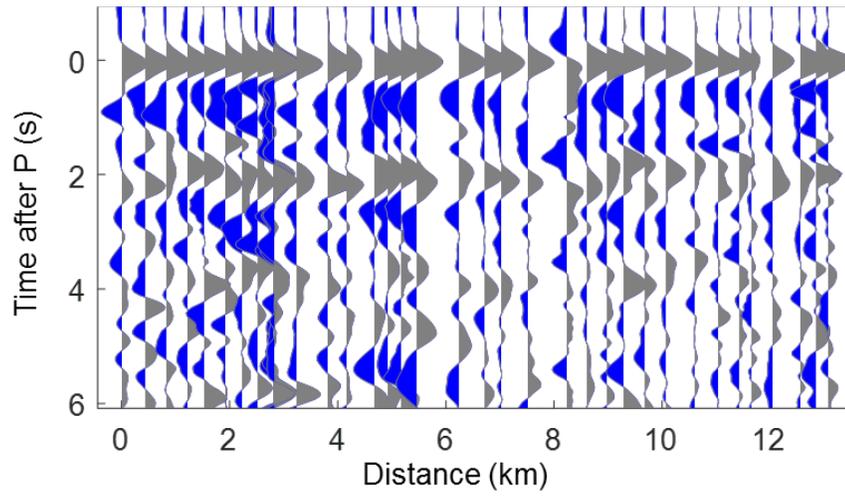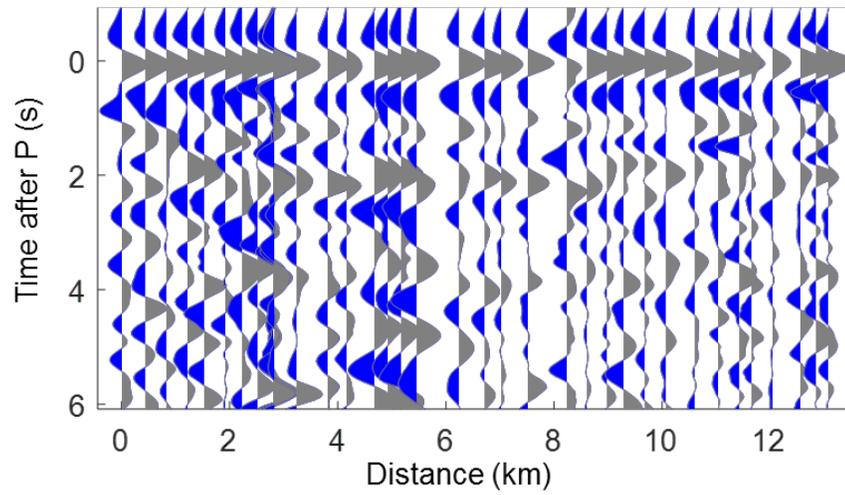
A. 0.1 – 0.5 Hz
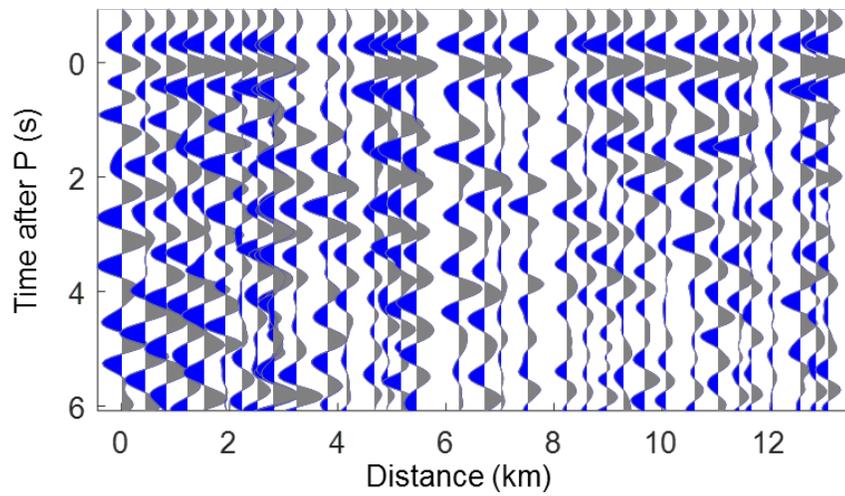
B. 0.5 – 1.0 Hz

C. 1.0 – 1.5 Hz

Tomasino Line – Southeast frequency bins

### D. 0.1 – 0.5 Hz
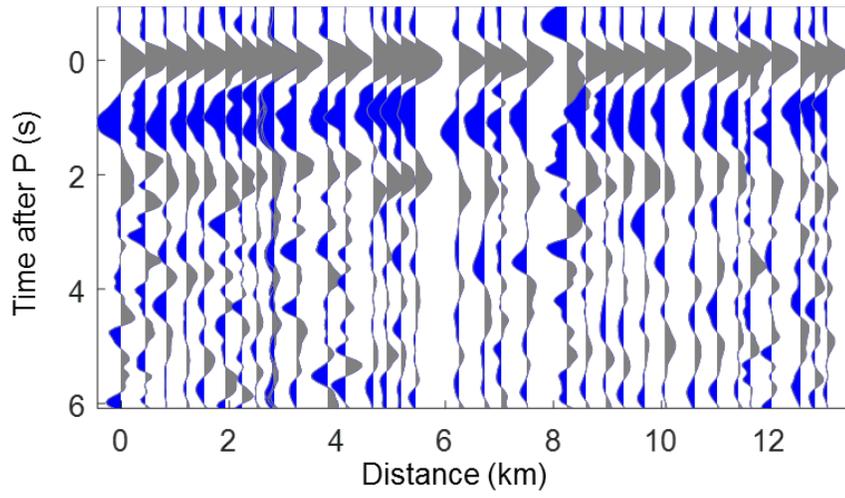
E. 0.5 – 1.0 Hz
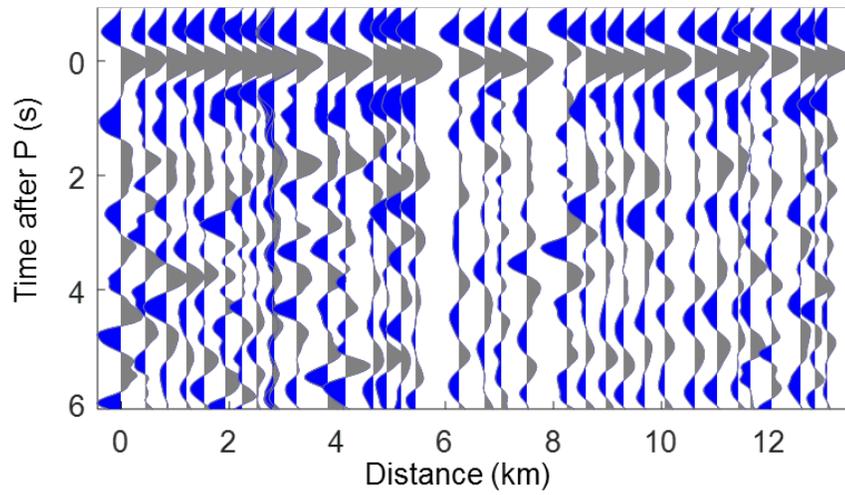
F. 1.0 – 1.5 Hz
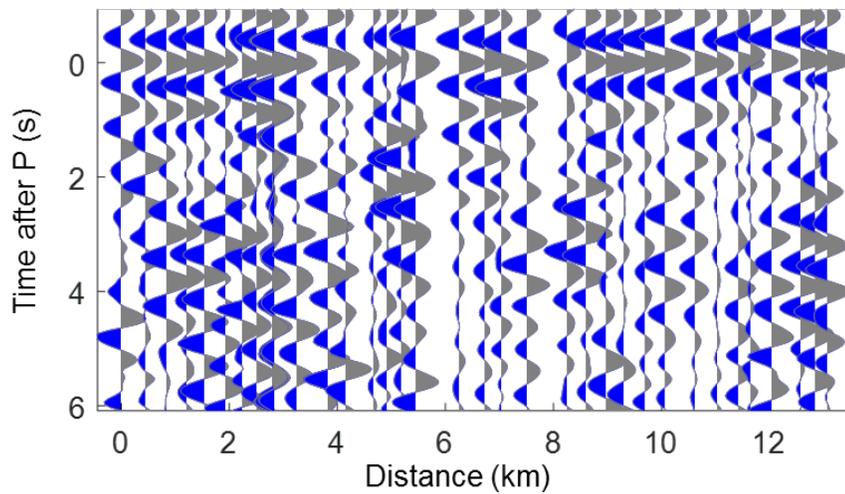
Figure 37: Tomasino TVR profile separated by azimuth and by frequency bin. Northwest events (A,B,C) are Russia and Japan. Southwest events (D,E,F) are both Colombia earthquakes and Argentina. Frequency bins only extend to 1.5 Hz due to signal-to-noise degradation at higher frequencies.

A. Sepultura Line

B. Sepultura Line – Annotated
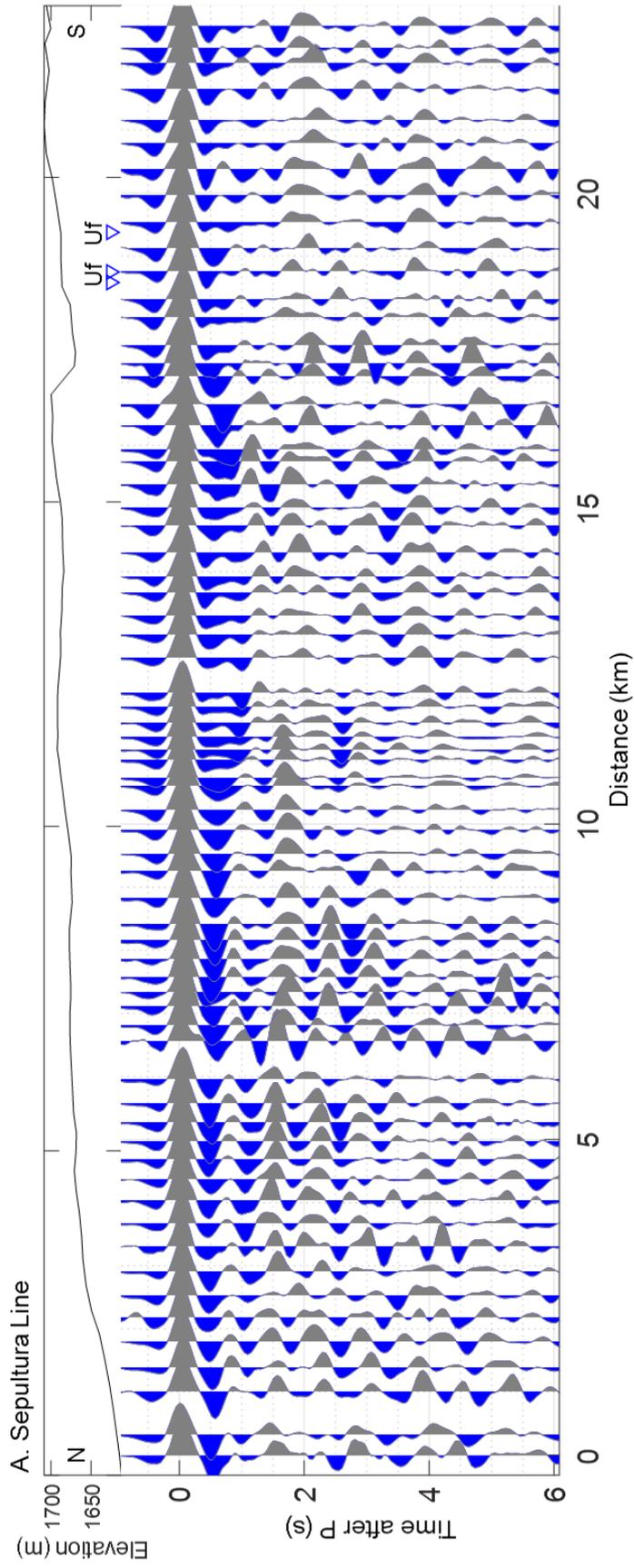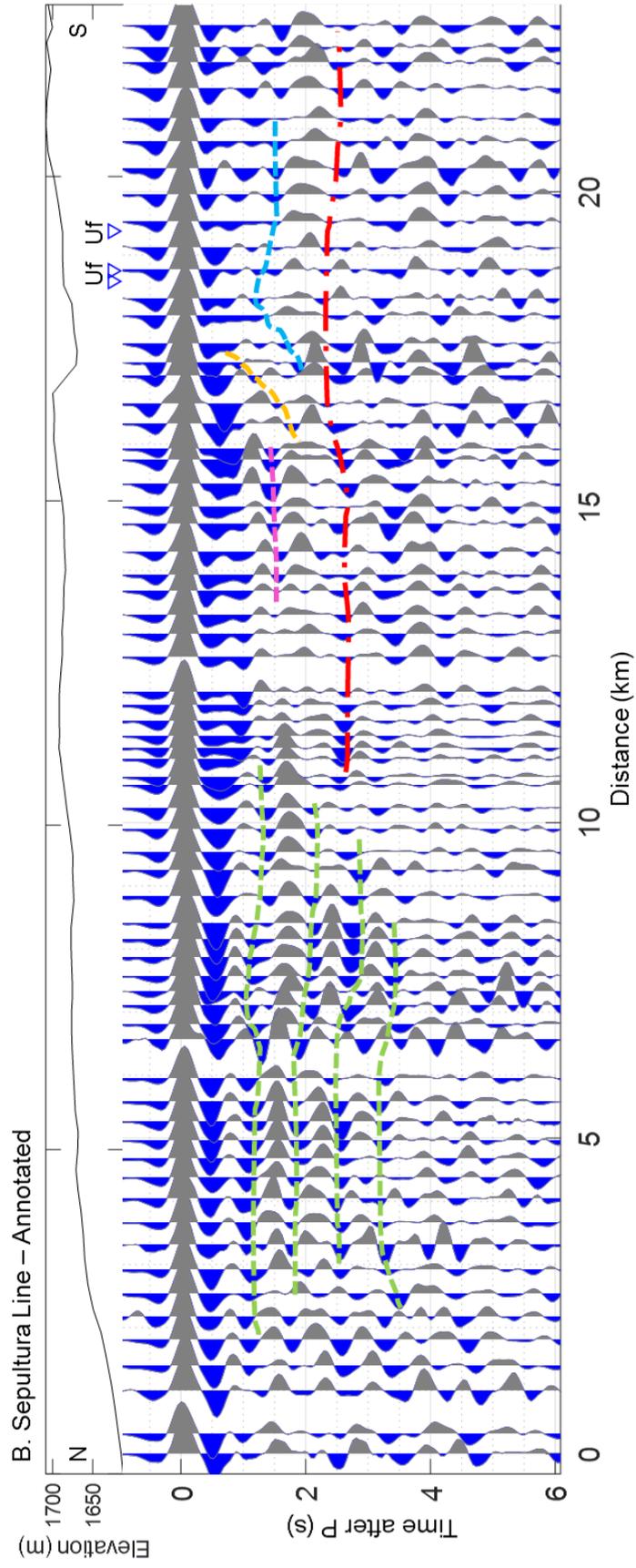
Figure 38: A. The Sepultura line TVR profile overlain by corresponding topography. Time is shown to 6 seconds depth (~20 kilometers) to focus on shallow crustal arrivals. Distance is from the northernmost trace. Faults labelled as Uf are unnamed faults. B. The same as A, but with annotated features discussed in the text.

# Sepultura Line – Northwest frequency bins
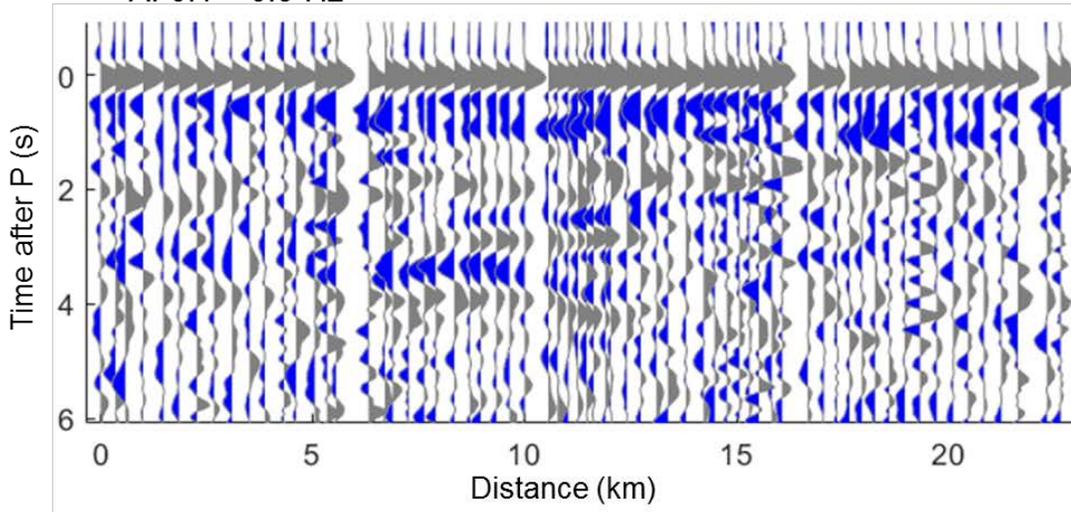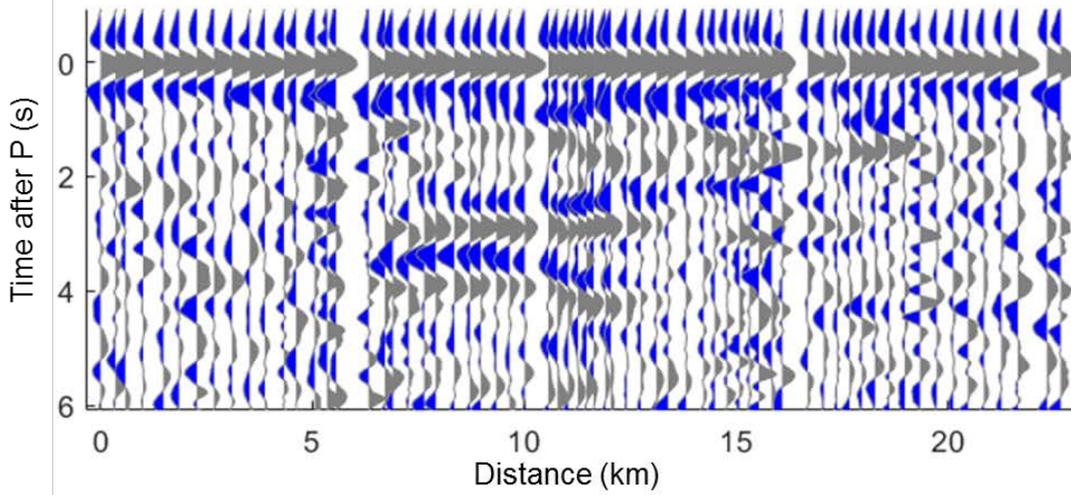
## A. 0.1 – 0.5 Hz
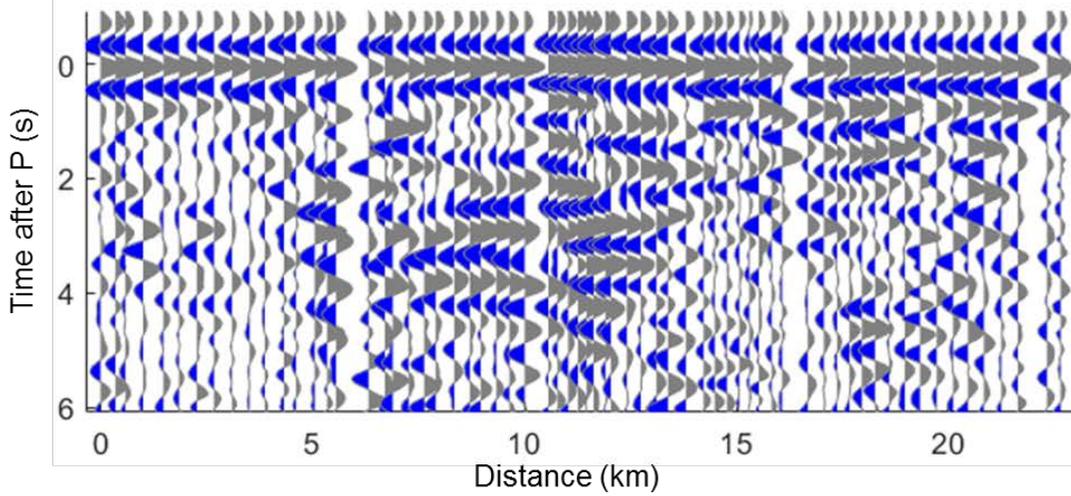
B. 0.5 – 1.0 Hz

C. 1.0 – 1.5 Hz

Sepultura Line – Southeast frequency bins

D. 0.1 – 0.5 Hz
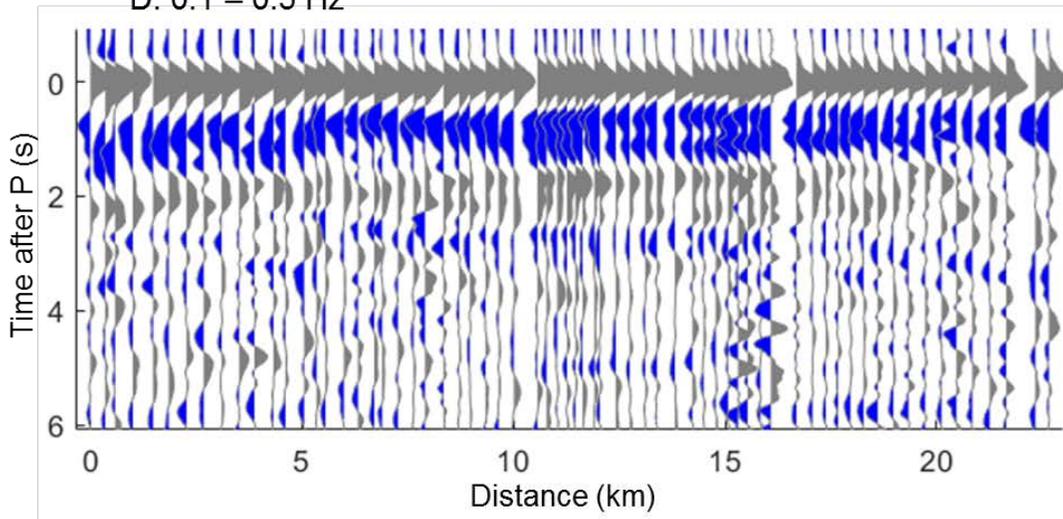
E. 0.5 – 1.0 Hz
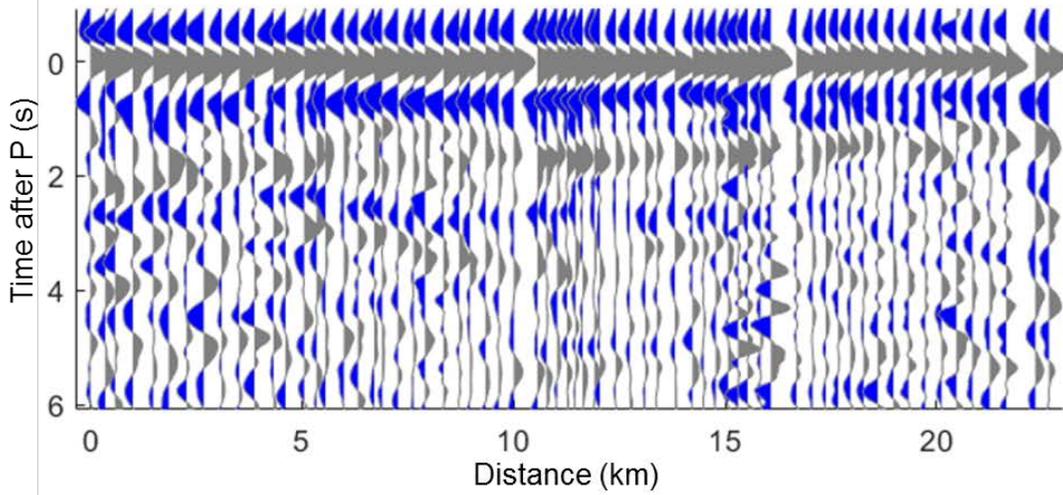
F. 1.0 – 1.5 Hz
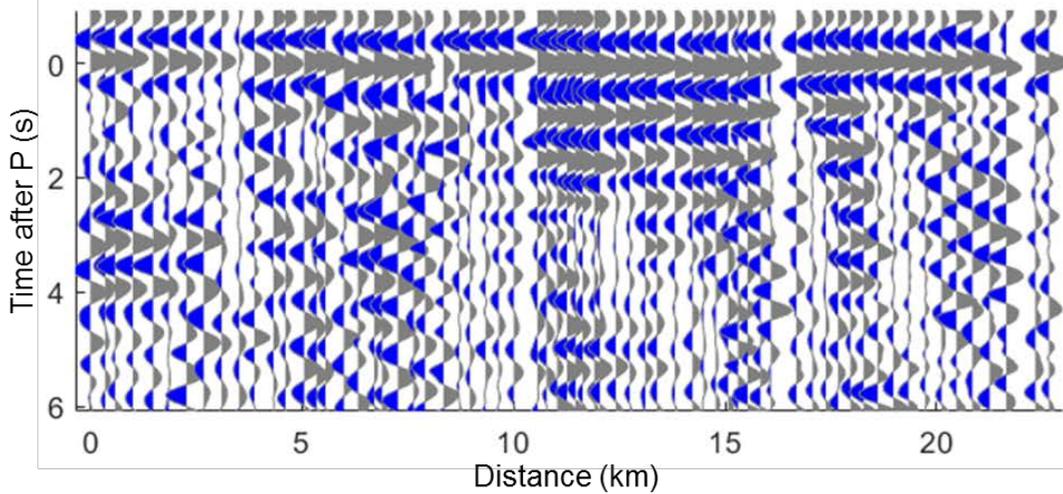
Figure 39: Sepultura TVR profile separated by azimuth and by frequency bin. Northwest events (A,B,C) are Russia and Japan. Southwest events (D,E,F) are both Colombia earthquakes and Argentina. Frequency bins only extend to 1.5 Hz due to signal-to-noise degradation at higher frequencies.

A. Cottonwood Line

B. Cottonwood Line – Annotated
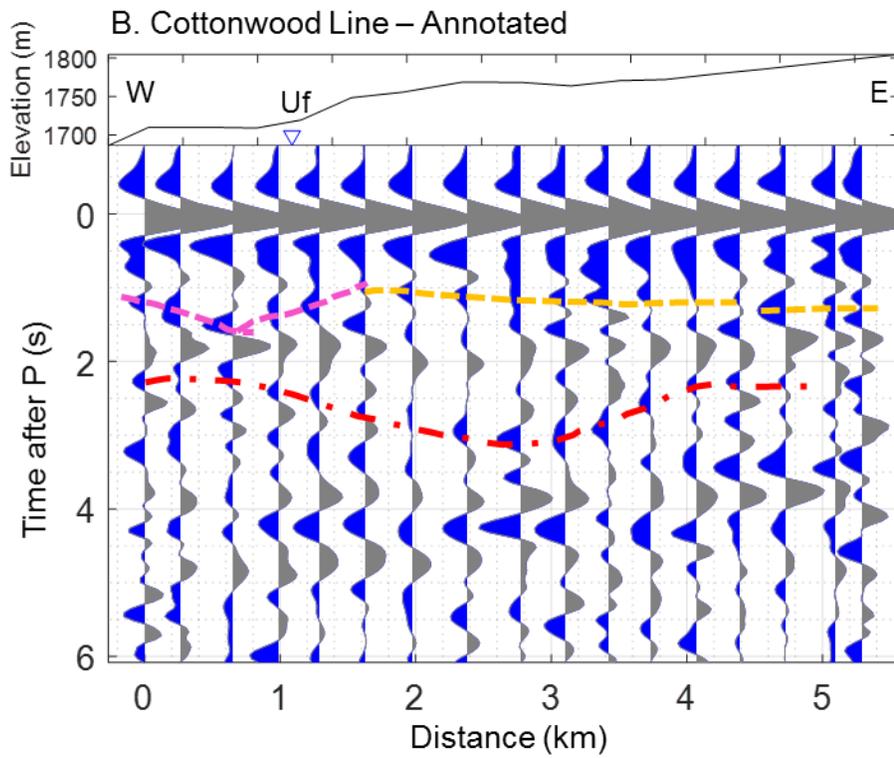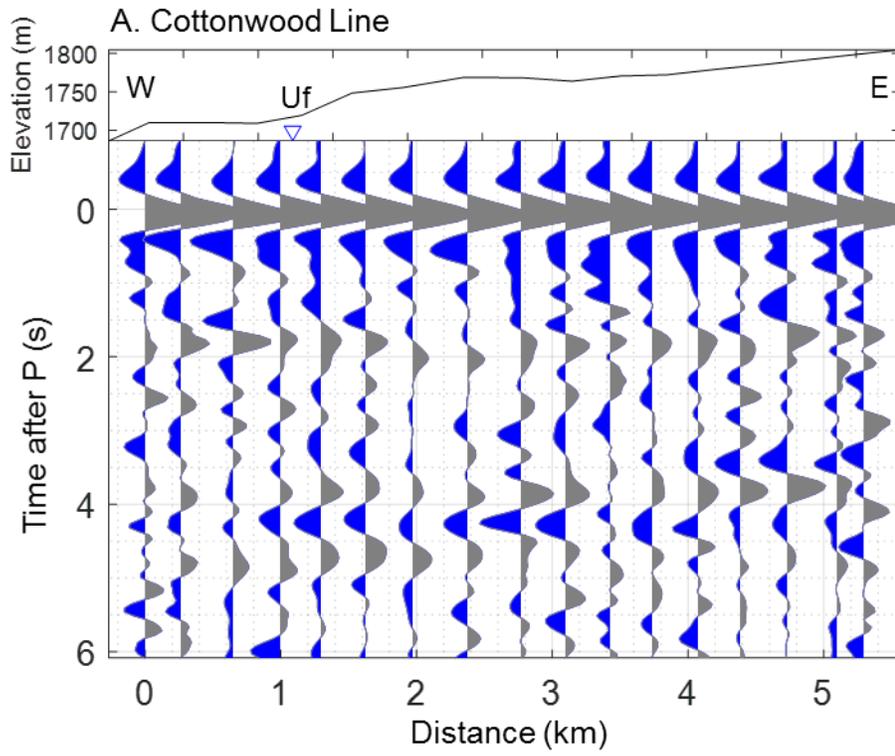
Figure 40: A. The Cottonwood line TVR profile overlain by corresponding topography. Time is shown to 6 seconds depth (~20 kilometers) to focus on shallow crustal arrivals. Distance is from the westernmost trace. Uf marks an unnamed fault. B. The same as A, but with annotated features discussed in the text.

Cottonwood Line – Northwest frequency bins
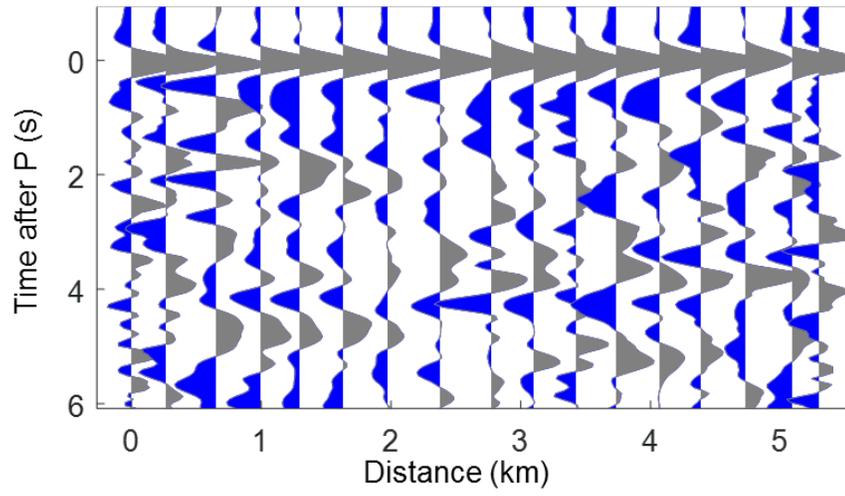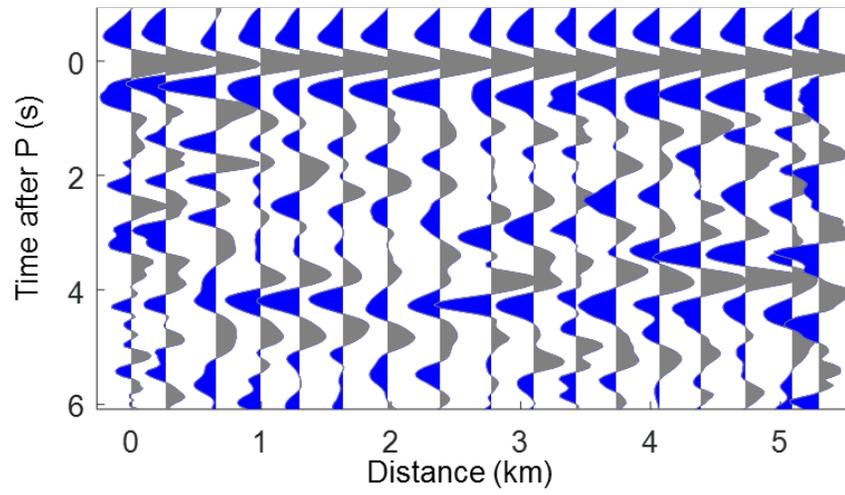
A. 0.1 – 0.5 Hz
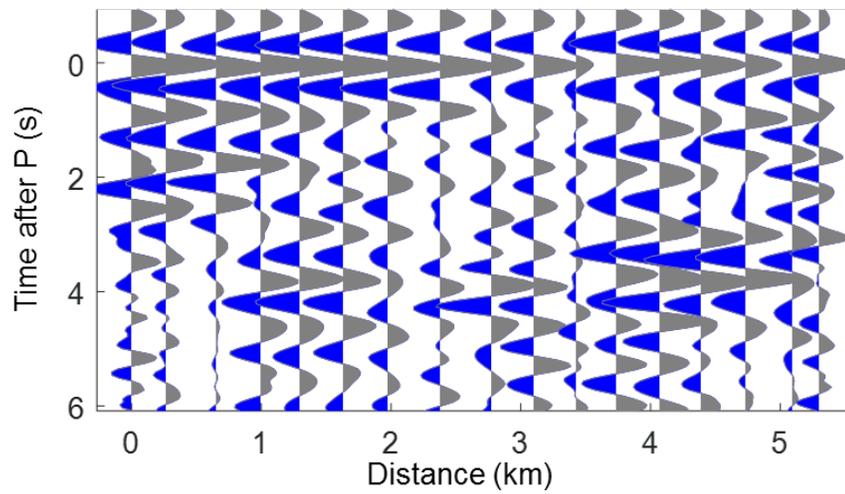
B. 0.5 – 1.0 Hz

C. 1.0 – 1.5 Hz

Cottonwood Line – Southeast frequency bins

D. 0.1 – 0.5 Hz
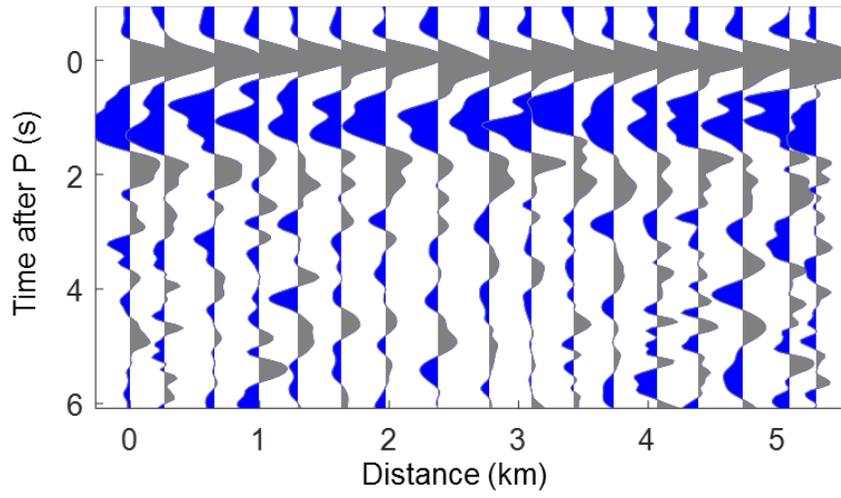
E. 0.5 – 1.0 Hz
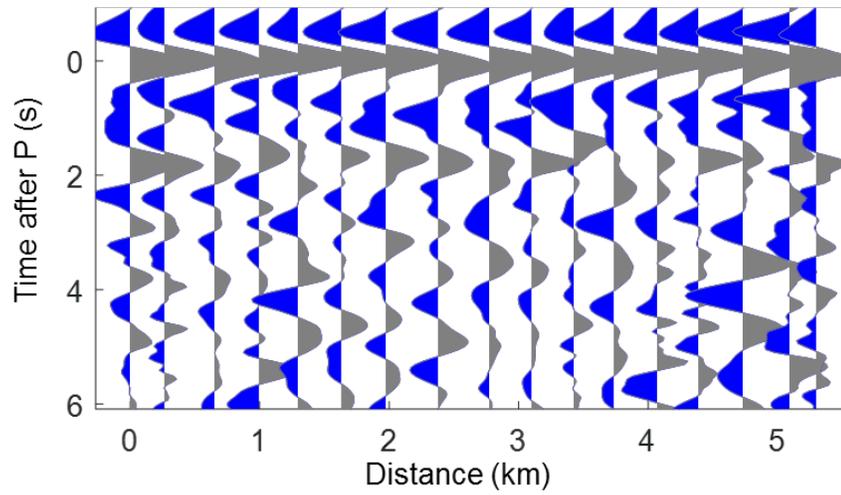
F. 1.0 – 1.5 Hz
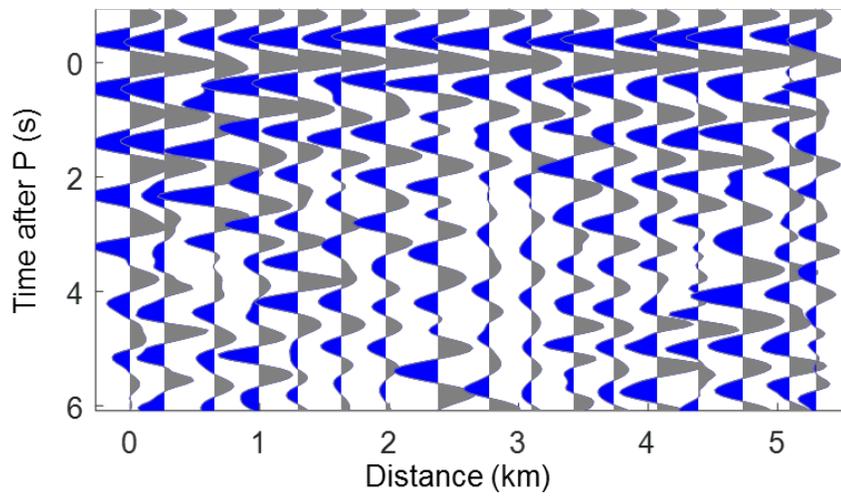
Figure 41: Cottonwood TVR profile separated by azimuth and by frequency bin. Northwest events (A,B,C) are Russia and Japan. Southwest events (D,E,F) are both Colombia earthquakes and Argentina. Frequency bins only extend to 1.5 Hz due to signal-to-noise degradation at higher frequencies.

B. Montosa Line – Annotated
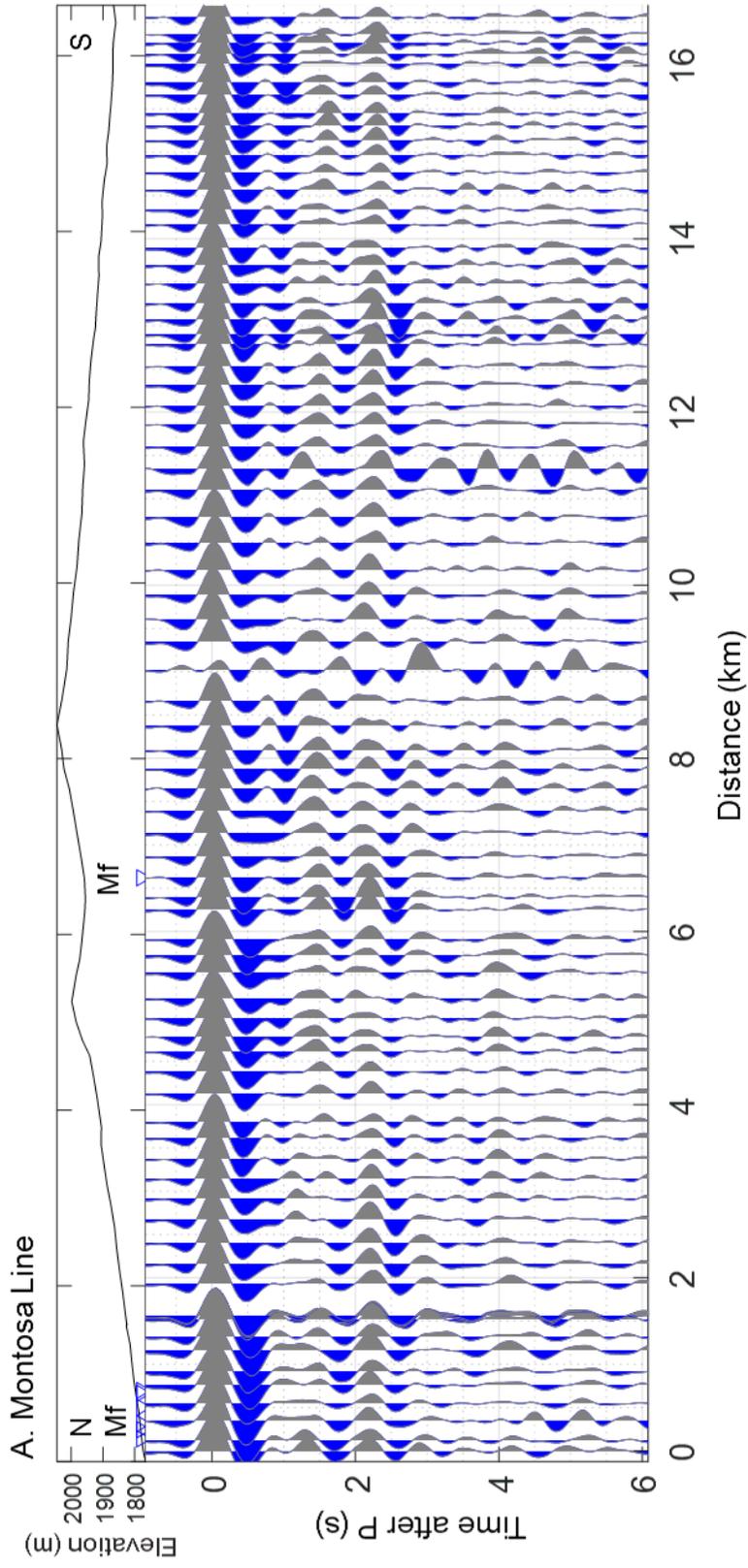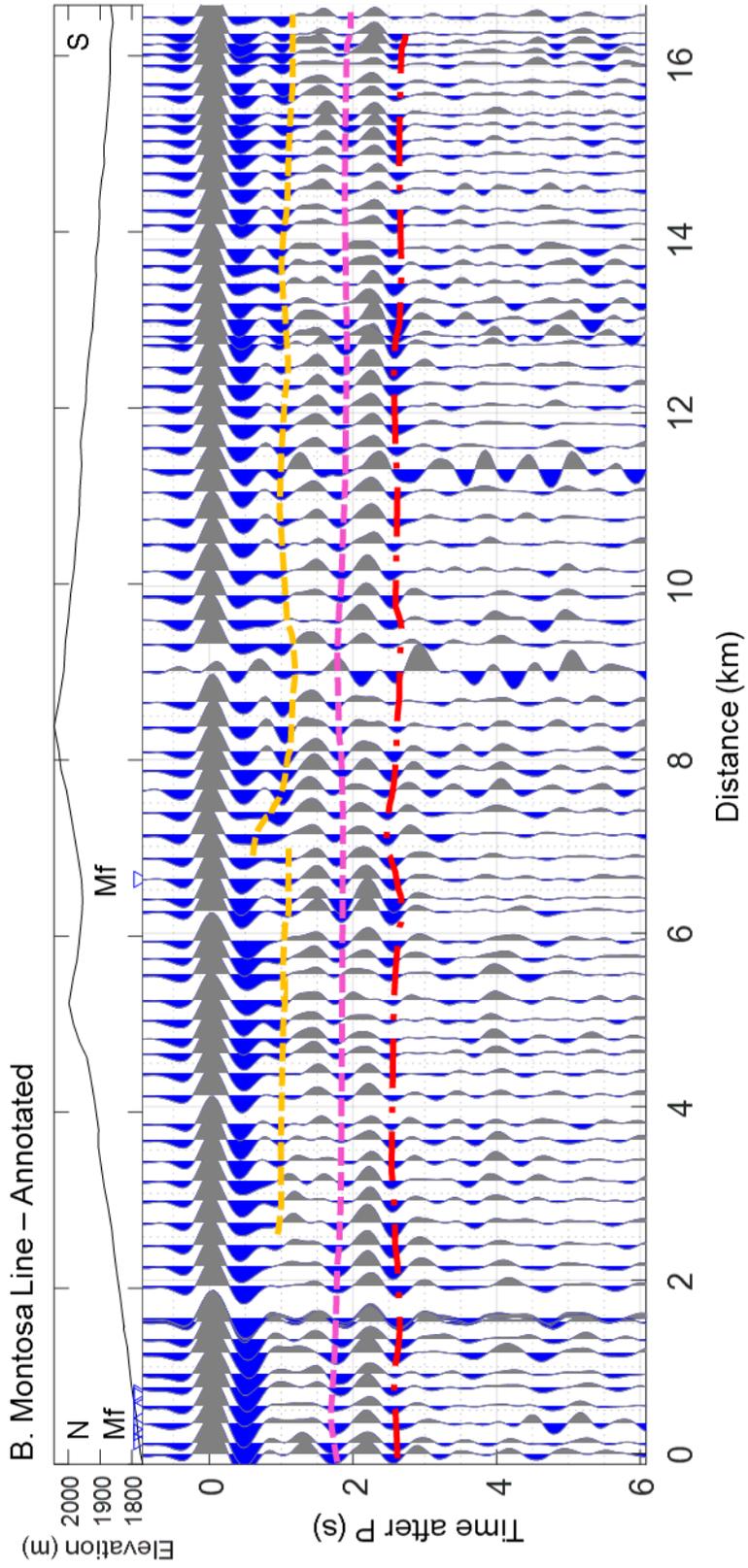
Figure 42: A. The Montosa line TVR profile overlain by corresponding topography. Time is shown to 6 seconds depth (~20 kilometers) to focus on shallow crustal arrivals. Distance is from the northernmost trace. Mf marks the Montosa fault. B. The same as A, but with annotated features discussed in the text.

Montosa Line – Northwest frequency bins
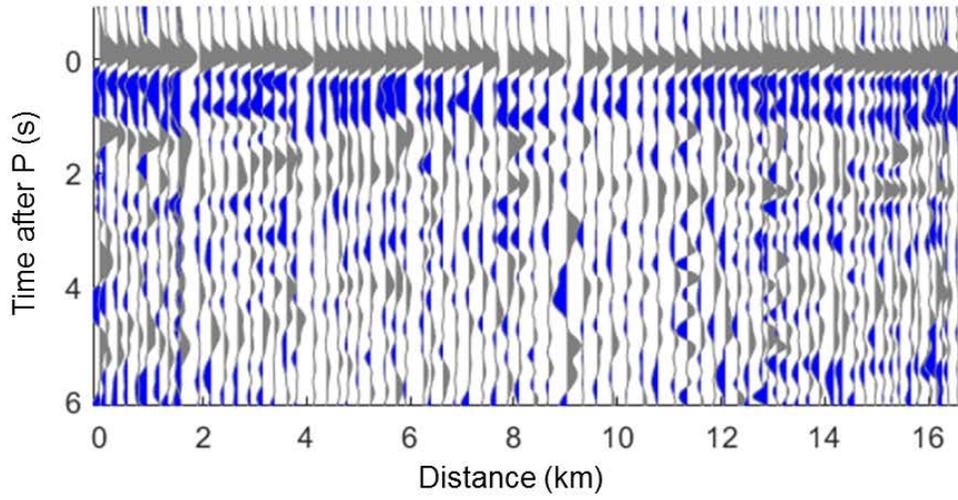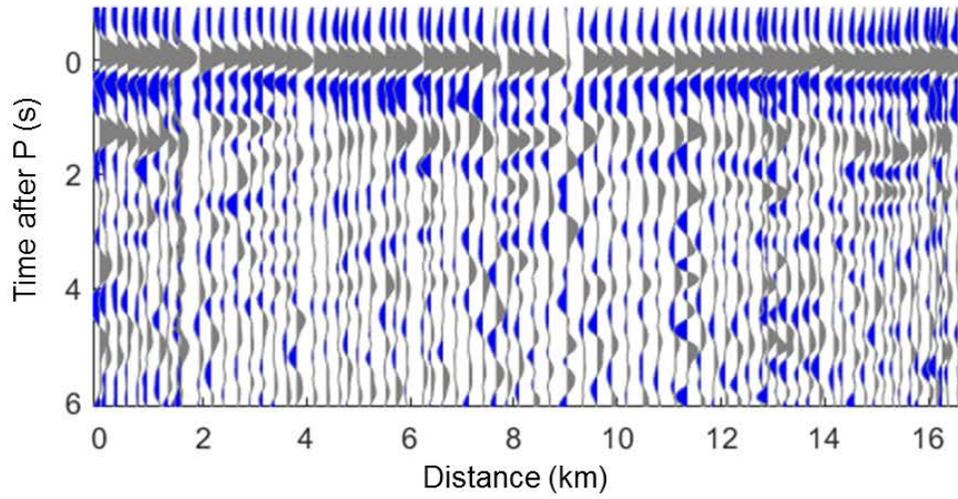
A. 0.1 – 0.5 Hz
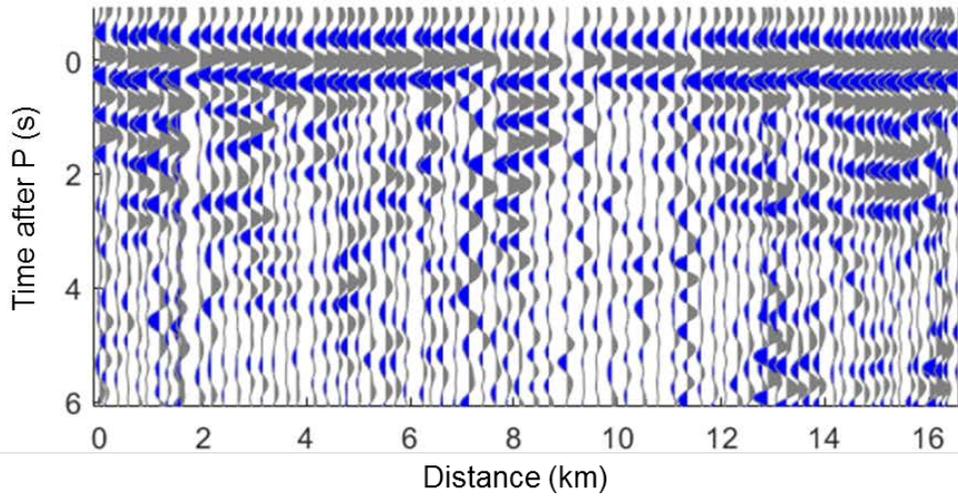
B. 0.5 – 1.0 Hz

C. 1.0 – 1.5 Hz

Montosa Line – Southeast frequency bins

D. 0.1 – 0.5 Hz

E. 0.5 – 1.0 Hz

F. 1.0 – 1.5 Hz

157
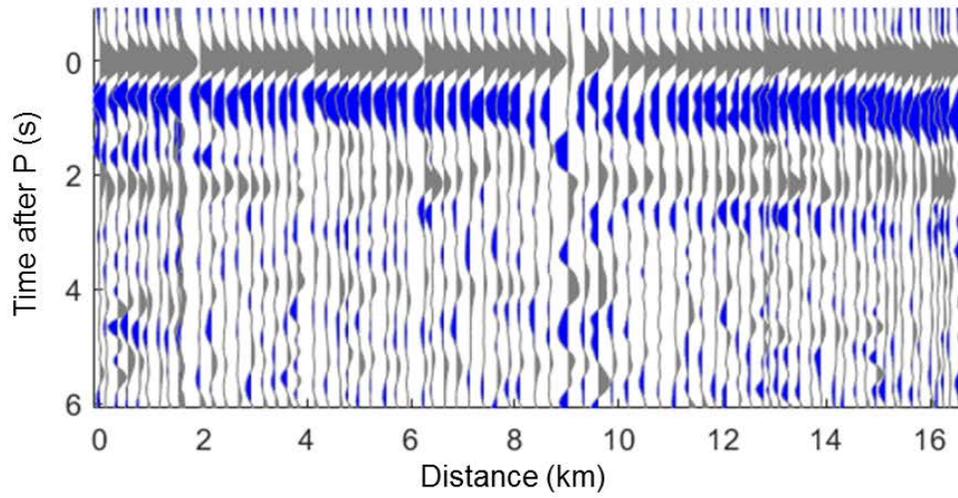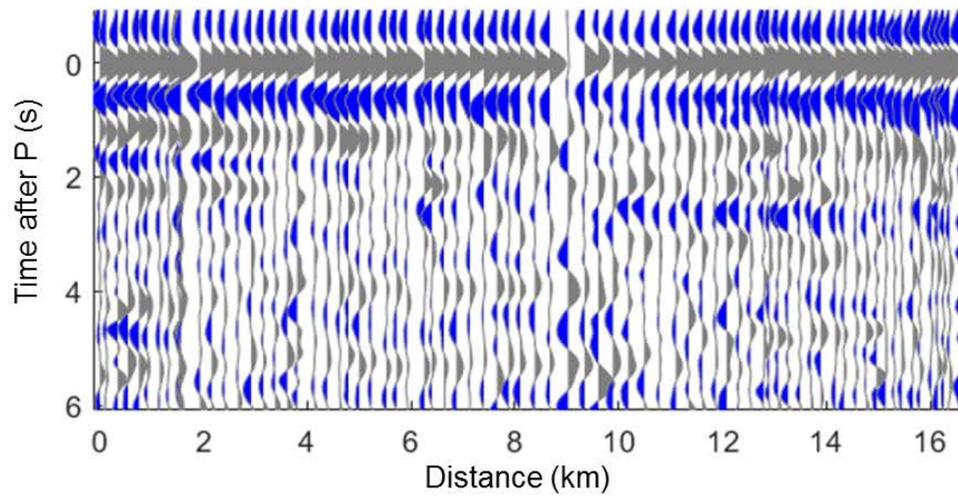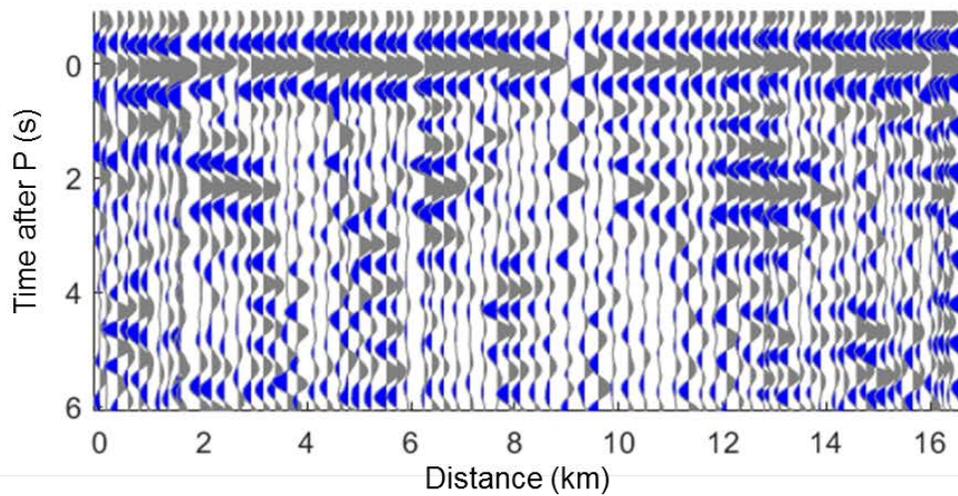
Figure 43: Montosa TVR profile separated by azimuth and by frequency bin. Northwest events (A,B,C) are Russia and Japan. Southwest events (D,E,F) are both Colombia earthquakes and Argentina. Frequency bins only extend to 1.5 Hz due to signal-to-noise degradation at higher frequencies.

A. Synthetic Traces by Component

Vertical Component

Radial Component
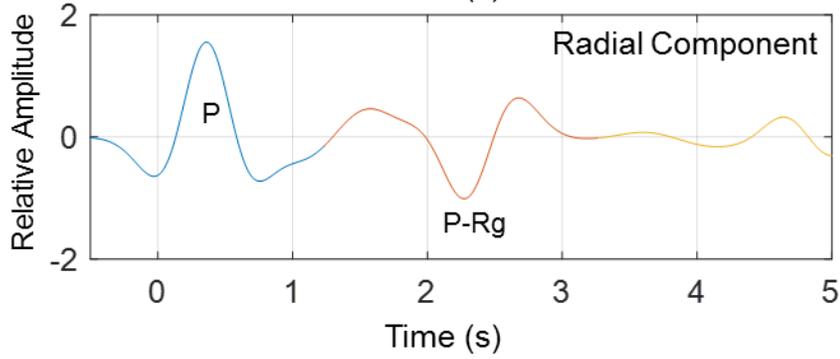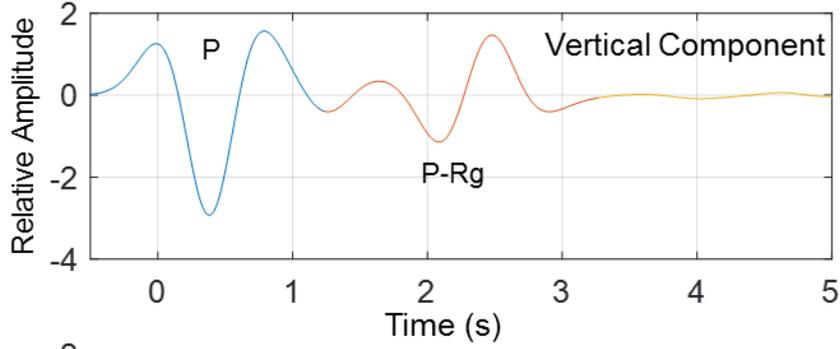
B. Synthetic Particle Motion
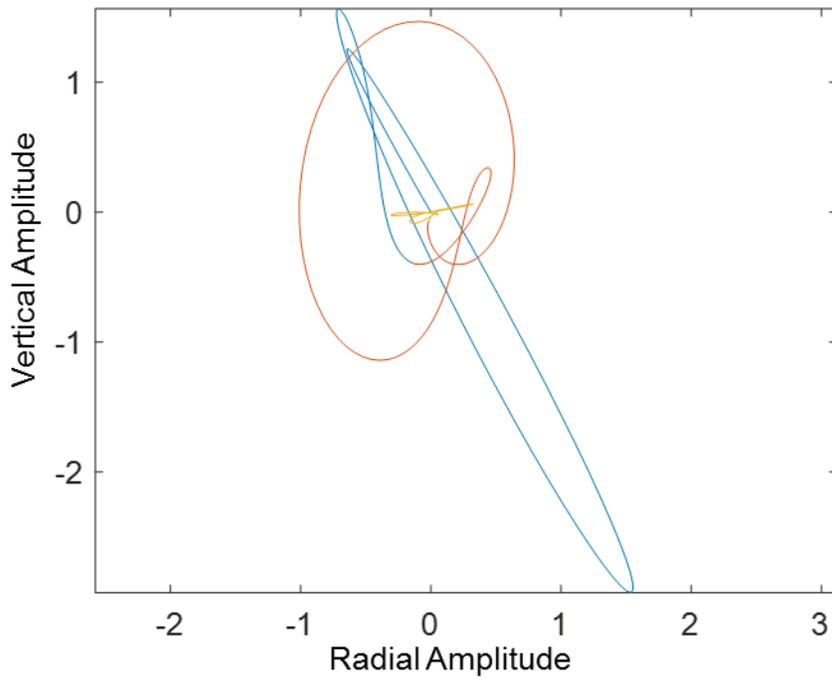
Figure 44: Basin 2 synthetic seismogram trace number 903, ~135.4 km across profile, as an example of particle motion in synthetic seismograms. A. The first five seconds of both the vertical (top) and radial (bottom) component, with the initial P-wave arrival (P, blue) and the P-to-Rayleigh (P-Rg, red) conversion labelled. B. Particle motion plot showing radial vs vertical amplitude. Colors correspond to A (blue P, and red P-Rg).

A. Broadband Traces by Component

Vertical Component

P

P-Rg

Radial Component

P

P-Rg

B. Broadband Particle Motion
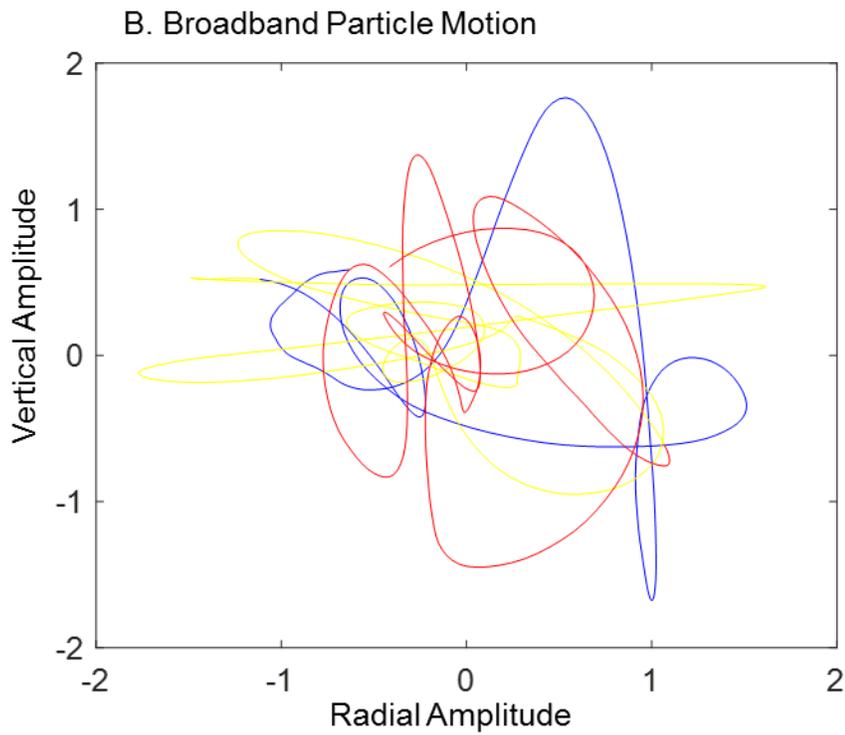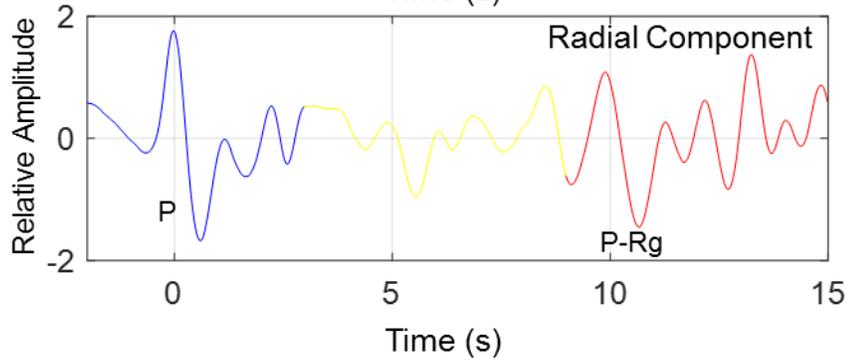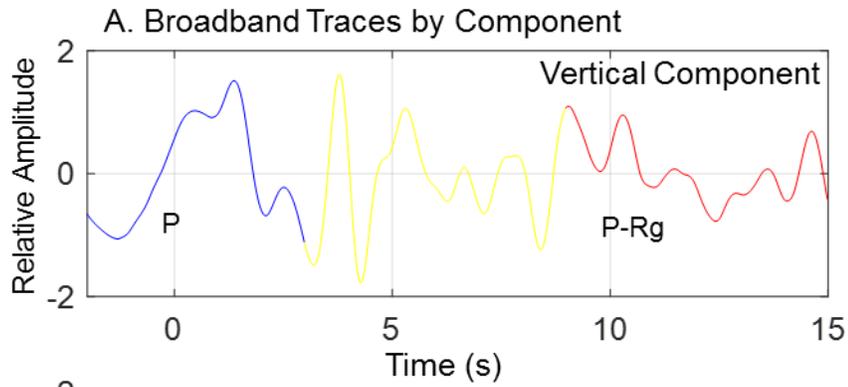
Figure 45: Particle motion from broadband data in the Sevilleta Array. Data pulled from the Popotosa broadband station (IRIS DMC network: XE station: POPO), during the Russia M5.4 (zero time: 2015-02-19 16:43:25.9). A. Fifteen seconds of both the vertical (top) and radial (bottom) component, with the initial P-wave arrival (P, blue) and the P-to-Rayleigh (P-Rg, red) conversion labelled. B. Particle motion plot showing radial vs vertical amplitude. Colors correspond to A (blue P, and red P-Rg).
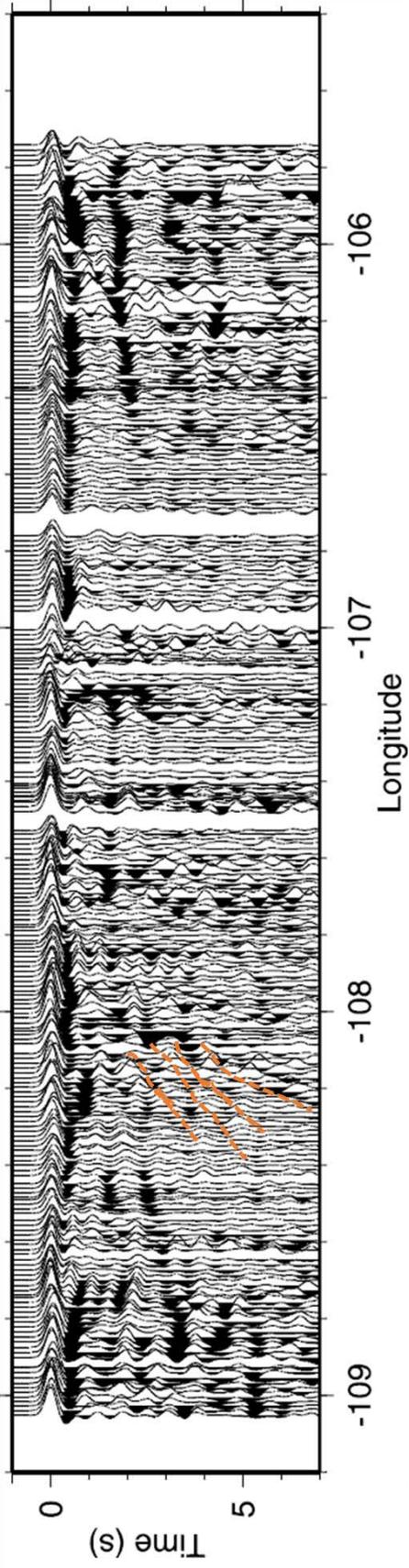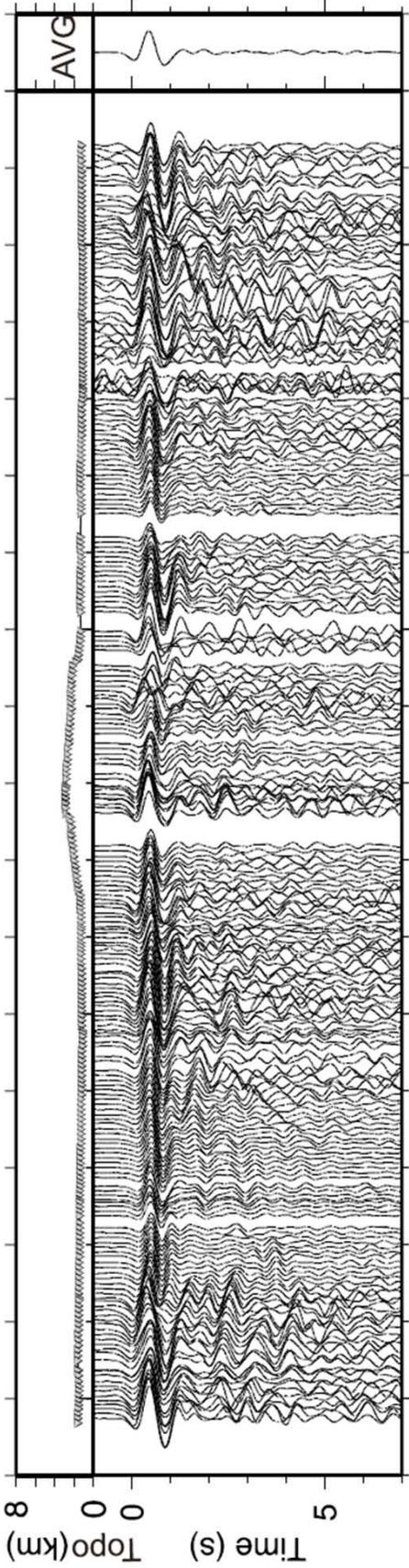
Figure 46: TVR Profiles of the Bighorn basin, Wyo. from Yang et al. (2012). At ~108 longitude, steeply dipping arrivals can be seen in both the top and bottom images. My interpretation is annotated in the bottom image (modified from Yang et al., 2012)

A. Sevilleta Array Palo Duro Line

B. Cocorp Line 2A

165
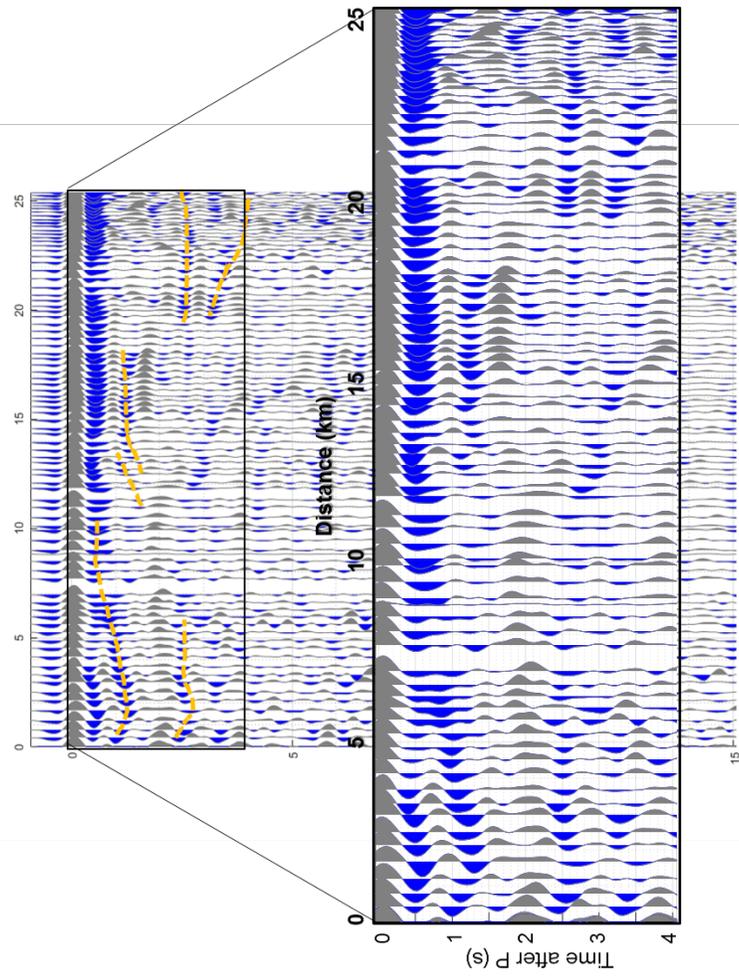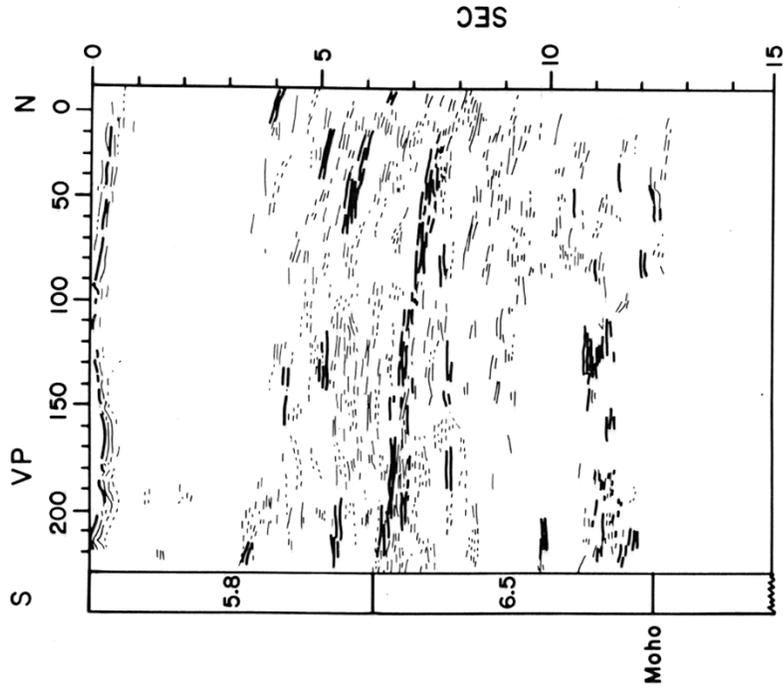
Figure 47: Comparing the results from COCORP and the Sevilleta array. A. The Sevilleta array Palo Duro line, with a zoom in to the first 4 seconds of the data to show shallow crustal arrivals. B. COCORP line 2A, from Brown et al., 1979.

Line 1A

COCORP analysis by
de Voogd et al., 1986

1x1 SCALE at 4 km/sec

SECONDS

Firebreak Line

Sevilleta Array

Time after P (sec)

Distance (km)

Line 1A

SEC
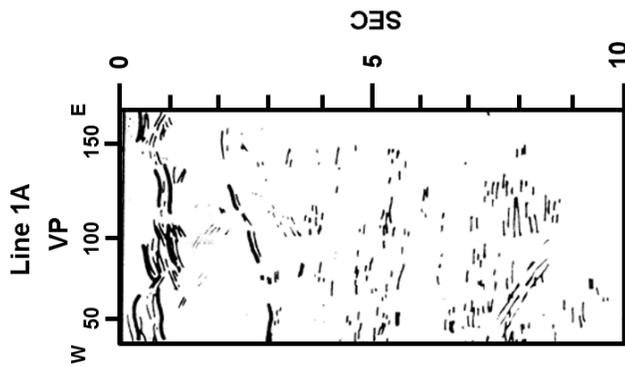
COCORP analysis by
Brown et al., 1979
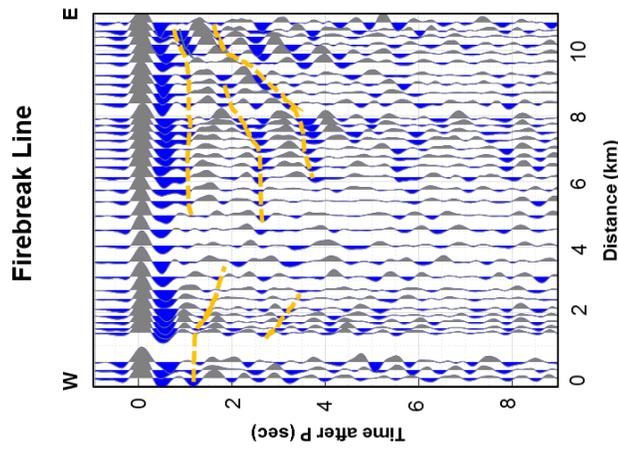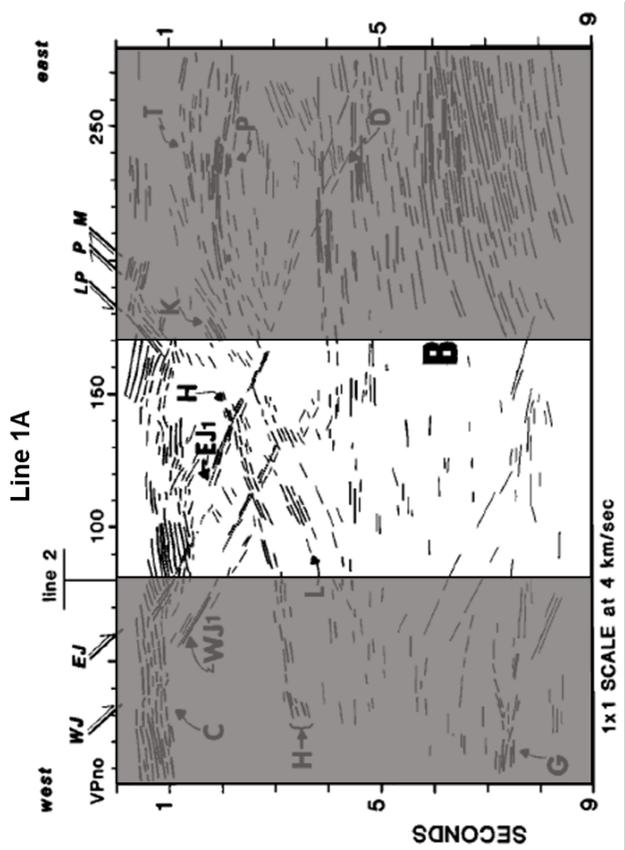
Figure 48: Direct comparison of Brown et al.'s (1979) interpretation of COCORP Line 1A (left), the analysis of the Firebreak line in this study (middle), and de Voogd et al.'s (1986) analysis of COCORP Line 1A.